

# **Engineering micro- and nanoscale cavities for applications in light manipulation**

by

Yi-Kuei Wu

**A dissertation submitted in partial fulfillment  
of the requirements for the degree of  
Doctor of Philosophy  
(Electrical Engineering)  
in the University of Michigan  
2013**

Doctoral committee:

Professor L. Jay Guo , chair

Professor Nickolas A. Kotov

Associate Professor Pei-Cheng Ku

Assistant Research Scientist Xiuli Zhou

Yi-Kuei Wu

© ————— 2013

All Rights Reserved

*I lovingly dedicate this thesis to my parents, my wife, and the whole family, who have  
been supporting me each step of the way.*

# Acknowledgements

It is with immense gratitude that I acknowledge the support and help of my Professor L. Jay Guo, who has been providing guidance, research suggestions, and importantly, a spirit of adventure on the research topics for the real-world applications. His critical thinking inspires me not to be trapped by conventional logic paths. Behaving as my brother, He also shared the philosophy of life with me. Without his mentorship in such a variety of aspects, all the important achievements in my PhD would not have been accomplished.

I would like to thank my committee members, Professor Nickolas A. Kotov, Professor Pei-Cheng Ku, Professor Herbert Winful, and Doctor Xiuli Zhou for their input, valuable discussions, accessibility, dissertation review, and doctoral oral defense. Their valuable suggestions helped me make this dissertation complete.

I am indebted to all colleagues who supported me. Yi-Hao Chen, Jeremy Moore, Min Kim, Wei Guo, Chi-Sen Lee, and Xin Tu have been offering me help on DARPA NACHOS project. In the plasmonic color filter projects, I would also like to thank Dr. Hao-fei Shi, Alex Kaplan, and Tao Ling for the suggestions on the simulations and fabrication. It is also my pleasure to work with Ting Xu, Andrew Eugene Hollowell, Cheng Zhang, Young Jae Shin, and Kyu-Tae Lee. I would also like to acknowledge the contribution to color filter project from Ting Xu, Andrew Hollowell, and Cheng Zhang. They are not only the best people I have worked with but also my friends forever. It is also nice to work with Il Yong Jung, Tae Bae Kim, and Dr. SE Chung since they provide insight on color filtering characteristics from industry perspectives.

I also consider it an honor to work with student colleagues in University of Michigan: Se Hyun Ahn, Hui Joon Park, Sung-Liang Chen have provided me both technical and mental support to go through my PhD. I am also greatly thankful to my friends who share their expertise on fabrication and characterization: Kuen-Ting Shiu, Michael Kuo, Siddharth Gaba, I-Ning Hu, Kuang-Wei Lin, Sung-Liang Chen, and LNF and EMAL staff.

Finally, I would like to thank my parents, my wife, my brother, and volunteer members in Tzu-Chi foundation for being my mental support.

# Table of Contents

Dedication .....	ii
Acknowledgements .....	iii
List of Figures .....	vii
List of Appendices .....	xii
Abstract .....	xiii
Chapter 1     Introduction .....	1
1.1     Background of micro- and nano-cavities .....	1
1.2     Motivation .....	2
1.3     Applications .....	4
1.4     Chapter overview .....	6
Chapter 2     Photonic crystal microdisk (PCM) lasers .....	10
2.1     Introduction and motivation .....	10
2.2     Methods and Results .....	11
2.3     Discussions of high $\beta$ .....	17
2.4     Multi-channel microdisk lasers .....	21
2.5     Summary .....	26
Chapter 3     Plasmonic nanoresonators for high-resolution color filtering and spectral imaging .....	27
3.1     Introduction and motivation .....	27
3.2     Design of plasmonic nanoresonators for color filtering .....	30
3.3     Plasmonic nanoresonators for spectral and polarimetric imaging .....	40
3.4     Discussion and summary .....	42
Chapter 4     Metallic resonant waveguide grating (MRWG) color filters .....	44
4.1     Motivation of color filters for LCD TV .....	44
4.2     Design and results .....	46
4.3     Discussions .....	54
4.4     Summary .....	57
Chapter 5     Study of wavelength tunable and angle-robust plasmonic spectrum filtering .....	58
5.1     Introduction and motivation .....	58
5.2     Methods .....	60
5.3     Design and theory .....	61
5.4     Ultra-high resolution and widely tunable color filtering .....	64
5.5     Design rules for angle insensitivity .....	69
5.6     Summary .....	79
Chapter 6     Wide angled transmission plasmonic color filters .....	80

6.1	Introduction and motivation.....	80
6.2	Design I for the transmission color filters and its results.....	81
6.3	Discussion – Design I .....	83
6.4	Design II – improved design I .....	87
6.5	Discussion – Design II .....	89
6.6	Design III – coupled cavity type transmission color filters .....	91
6.7	Discussion – Design III.....	95
6.8	Summary .....	97
Chapter 7	Summary and vision .....	99
7.1	Research summary .....	99
7.2	Future work and vision .....	102
Appendices	.....	105
Bibliography	.....	113

# List of Figures

Fig. 2.1 (a) Schematics of the photonic crystal microdisk (PCM) laser and the field distribution of the WGM mode TE(9,1) (b) Simulated spontaneous emission coupling factor into lasing mode based on FDTD method (c) Scanning electron micrograph image of PCM laser. .... 14

Fig. 2.2 (a) Threshold spectra below and above threshold of the two-stack device in the logarithmic scale (b) The calculated threshold curve with various  $\beta$  (colored solid lines) and the experimental L-L curve (triangle dots). Inset illustrates the experimental L-L curve in linear scale..... 17

Fig. 2.3 (a) Mode density modification in a 1D PhC with two pairs (b) The schematics of the density of states measurement (c) calculated and measured ratio of DOS for single and double stack of microdisk. .... 21

Figure 2.4 (a) experimental lasing spectrum for a vertically 2-disk microdisk lasers with both the top and bottom disk thickness 258nm. (b) the calculated cavity mode spectrum of the 2-disk microdisk cavities with various thickness of top disk 261, 281, and 301nm, given the bottom disk thickness of 258nm. (c) Hz field distribution of the single mode at top disk thickness of 301nm (cross-section), (d) Hz field distribution of the mode at 957.1nm with top disk thickness of 261nm (cross-section), (e) Hz field distribution of the mode at 951.2nm with top disk thickness of 261nm (cross-section). .... 25

Figure 3.1 Plasmonic nanoresonators formed by MIM stack arrays. (a) Schematic diagram of the proposed plasmonic nanoresonators. The white arrow represents the incident white light and the red, yellow, green and blue arrows represent the transmitted filtered light from the different stack arrays. Grey, pink and blue in the structure indicate the material of aluminum (Al), zinc selenide (ZnSe) and magnesium fluoride (MgF<sub>2</sub>) respectively. Inset is the scanning electron microscopy image of the fabricated device and white scale bar represents 1 $\mu$ m. (b) Plasmonic waveguide dispersions in MIM stack array. Red, green and blue dots correspond to the case of filtering primary RGB colors. Red and blue curves correspond to anti-symmetric and symmetric modes respectively. The shaded region indicates the visible range. (c) Simulated transmission spectra for the RGB color filters. The solid and dash curves correspond to TM and TE illuminations respectively. The stack period for RGB filters is 360, 270 and 230 nm. (d) Cross-section of the time-average magnetic field intensity and electric displacement distribution (red arrow) inside the MIM stack at a peak wavelength of 650 nm with 360 nm stack period. The colors on the right side represent the constitutive materials, defined as in (a)..... 34

Figure 3.2 Plasmonic color filters. (a) Optical microscopic images of seven plasmonic color filters illuminated by white light. Scale bar: 10  $\mu\text{m}$ . (b) Experimentally measured transmission spectra of three fabricated color filters corresponding to the R, G, and B colors. The circle and triangle correspond to TM and TE illuminations respectively. (c) Scanning electron microscopy image of the pattern 'M' formed by two stack periods. The periods of the navy blue background and the yellow character are 220 and 310 nm, respectively. Scale bar: 3  $\mu\text{m}$ . (d) Optical microscopy image of the pattern illuminated with white light. ....38

Figure 3.3 Plasmonic color filters with a few slits. Simulated transmission for the green and red filters with 2, 4, 6 and infinite number of slits. The circle, triangle, diamond and star correspond to the structure with 2, 4, 6 and infinite slits respectively. Inset shows the optical microscopic images for the case of 2, 4 and 6 slits (namely, single, three, and five MIM stacked resonators, and slit number increases from bottom to top).....39

Figure 4.1 Manufacturing process flow for RGB Color filter<sup>88</sup> .....45

Figure 4.2 (a) Schematic of the metal resonant waveguide grating. (b) the simulated spectrum with the bandwidth between 15nm and 50nm by changing buffer layer thickness from 0 to 100nm. (c) SEM top view of the fabricated device with period of 300nm and gap of 54nm. (d) Normal incidence transmission images and (e) measured spectra for three square arrays of metal resonant waveguide gratings for blue, green, and red colors. The grating periods are 300, 350, and 450 nm, respectively, with 0.25 duty-cycles. The thicknesses of the silica buffer layer and silicon nitride waveguide layer are 50 and 100 nm, respectively .....50

Figure 4.3 (a) Proposed designs for commercialized and manufacturable RGB color filters for visual display in Samsung Electronics and (b) the corresponding spectra (blue, green, and red from left to right).....51

Figure 4.4 Process flow for manufacturable MRGW color filters .....52

Figure 4.5 SEM of (a) cross-sectional SU8 resist pattern on top of PMGI/SiNx/glass stack from Samsung Electronics, and (b) cross section of the pattern for the red color filter after O<sub>2</sub> dry etching (inset: zoom-out cross section view) .....53

Figure 4.6 (a) Color and manufacturing demonstration of blue, green, and red MRWG color filters on a single 4 inch glass wafer. (b), (c), and (d) shows non-ideal trench linewidth after lift-off process leads to side resonance peak effect in the visible spectrum for blue, green, and red color filters, respectively.....56

Figure 5.1 Plasmonic-nanocavity-based angle robust color filtering. (a) A schematic of the proposed structure and corresponding SEM image of a fabricated device with width (W)=45nm, depth (D)=160nm, and period (P)=180nm with  $\Theta$  as the incident angle of light. (b) Polarization charge and Poynting vector distribution of light

funneled into these nano-grooves, presented with the red–blue surface plot and purple arrows, respectively. (c) Intensity distribution of the magnetic-field  $H_y$  at resonance,  $P=180$ ,  $W=50$ , and  $D=170\text{nm}$ . (d) Reflection (simulated in solid lines and measured in dash lines) and measured absorption spectra (inset, dashed lines) at  $D=110$ ,  $130$ , and  $170\text{nm}$  in blue, green, and red curves, given fixed  $P=180$  and  $W=50\text{nm}$  at normal incidence. (e) Reflection spectra at fixed  $P=180\text{nm}$  and  $D=170\text{nm}$  demonstrating the three basic colors of the CMY color model, cyan (C), magenta (M), and yellow (Y), with varying  $W=40$ ,  $60$ , and  $90\text{nm}$  at normal incidence ..... 66

Figure 5.2 Color demonstrations with ultra-high resolution and polarization dependent images. (a) The SEM images and (b) optical image under white light illumination of fabricated colored images in the format of the Olympic rings. The full range of CMY colors are achieved by sweeping  $W$  from  $40$  to  $90\text{nm}$ , with  $P$  and  $D$  fixed at  $180\text{nm}$  and  $170\text{nm}$  respectively. (b) Shows that even a single short segmented nano-groove demonstrates color response. (c) Demonstrates utilizing polarization dependence to actively change the displayed image, where grooves with  $W=40$  for cyan and  $W=60\text{nm}$  for magenta under TM illumination. .... 69

Figure 5.3 Simulated angle resolved reflection spectra with various periods. The simulated angle resolved reflection spectra contour plots at periods  $P=140$  (a) ,  $P=180$  (b),  $P=220$  (c), and  $P=260\text{nm}$  (d). The green dash lines in all four figures indicate metal-insulator-metal Fabry-Perot (MIMFP) cavity mode, whereas the red dash lines refer to the grating assisted surface plasmon (GASP) modes whose dispersion is dependent on the grating period. The crossing between MIMFP and GASP when  $P=220$  and  $260\text{nm}$  indicates coupling between the two modes. The green dash line in (a) refers to the dispersion of odd mode defined in Figure 5(c). (e) The simulated angular absorption maxima in terms of various period from  $140$ ,  $180$ ,  $220$ , and  $260\text{nm}$ . .... 71

Figure 5.4 Experimental angle insensitive spectrum filtering. (a) The simulated angular absorption maxima in terms of various periods from  $140$ ,  $180$ ,  $220$ , and  $260\text{nm}$ . The angle resolved reflection spectra of this design with sweeping incident illumination angle from  $45^\circ$  to  $75^\circ$  are presented with the following device dimensions (b)  $P=180$ ,  $W=50$ , and  $D=130\text{nm}$ , (c)  $P=180$ ,  $W=50$ , and  $D=170\text{nm}$ , and (d)  $P=220\text{nm}$ ,  $W=50\text{nm}$ , and  $D=160\text{nm}$ . (b) and (c) show flat band absorption response indicating angle insensitivity, while (d) shows  $25\text{nm}$  resonance wavelength shift per  $30^\circ$  change in incident illumination angle representing coupling between MIMFP and GASP modes ..... 73

Figure 5.5 Optical mode coupling and period dependent field confinement. (a) shows mode dispersion with respect to the groove spacing ( $P-W$ ) and Period, as well as the definition of even and odd modes in the insets. The field distribution of  $H_y$  with

defined even and odd modes is plotted in (b) and (c), respectively. The intensity distribution of magnetic field  $H_y$  at the incident illumination angle of  $45^\circ$  is presented at  $P=180\text{nm}$  (d),  $220\text{nm}$  (e),  $260\text{nm}$  (f). (d) confirms that the field is well confined within the nano-groove corresponding to a MIMFP mode, while (d) and (f) show coupling to the top of the grating corresponding to GASP modes. ....78

Figure 6.1 (a) Schematic of transmission color filter Design I with the geometrical parameters defined same as Figure 5.1(a). (b) Spectra for blue, green, and red color based on the Design I with various height  $70\text{-}120\text{nm}$  (c) Simulated angle resolved spectrum for the blue color filter, and (d)  $H_y$  field intensity distribution at resonance wavelength= $480\text{nm}$ . ....83

Figure 6.2 (a) Transmission spectra for blue, green, and red color with various  $W$  from  $60$  to  $20\text{nm}$  given  $P$  and  $D$  fixed, and (b) Transmission spectra with various  $W$  from  $60$  to  $20\text{nm}$  given resonance wavelength and  $P$  fixed. (c) the equivalent F-P model for MIMFP cavity, (d) dispersion curves of the MIM waveguide (WG) at  $W=20$  (in blue),  $40$  (in red),  $60\text{nm}$  (in black), and the green dash curve indicates the dispersion of the  $n_{\text{out}}$ . The inset shows the imaginary part of propagation constant, which indicates waveguide loss. ....86

Figure 6.3 (a) Schematic of the design II, where DM is added and defined as the thickness of the top and bottom metal layer. (b) The optimized spectra for blue, green, and red colors given  $D=90\text{nm}$  and  $DM=20\text{nm}$  fixed . ....89

Figure 6.4 (a) shows the developed fabrication process, and (b) depicts the real part of refractive indices for plated (red curve) and evaporated silver (black curve), and (c) demonstrates the simulated transmission spectra with plasmonic metals as plated (red curve) and evaporated silver (black curve), where evaporated one has sharp resonance compared to plated one. ....91

Figure 6.5 (a) schematic of the coupled cavity transmission type color filter, where  $WS$ ,  $DT$ ,  $DB$  are added and defined as sidewall metal thickness, top metal thickness, and bottom metal thickness, respectively. (b) The simulated spectra for varying  $W$  from  $50$  to  $90\text{nm}$ , given  $DT=60$ ,  $DB=30$ ,  $WS=15$ ,  $D=100$ , and  $P=140\text{nm}$  fixed. ....92

Figure 6.6 (a)  $H_y$  field distribution in front, back, and coupled cavities, and (b) the absorption spectra of front and back cavities. These two cavity modes are spatially (in (a)) and spectrally (in (b)) overlapped. Therefore, the two cavities form a coupled mode and provide transmission maximum. ....94

Figure 6.7 (a) simulated and (b) experimental angular resolved spectra with angle swept from  $0$  to  $80$  degree. ....95

Figure 6.8 (a) the transmission resonance with fano shape peak located at  $576\text{nm}$  with  $DB=30\text{nm}$  at normal incidence. (b) transmission spectra with various angle swept from  $0$  to  $80$  degree with bottom metal thickness  $DB$  reduces from  $50$  to  $30\text{nm}$ .

(c) the model of fano resonance in the design III. (d) absorption spectra with various angle swept from 0 to 80 degree .....97

Figure A1. The mode profiles of HE(1,0) and HE(1,1) in the microdisk cavities oscillating up and down. ....106

Figure A2. **The reflection spectrum at period=180nm with different angle sweeping orientation.** Measurement schematic and reflection spectra at angle sweeping (a) perpendicular to the grating orientation and (b) parallel to the grating direction. ..109

Figure A3. **The reflection spectrum at period=260nm with different angle sweeping orientation.** Measurement schematic and reflection spectra at angle sweeping (a) perpendicular to the grating orientation and (b) parallel to the grating direction. ..109

Figure A4. **Single slit case.** (a) Schematic, and (b) absorption spectrum. ....110

Figure A5. **Two slits case.** (a) Schematic, (b) simulated reflection spectrum, (c) the  $H_y$  field distribution in contour plots (with scale bar) and Poynting vector in purple arrows. ....111

Figure A6 (a) absorbed optical field strength at angles of 0 and 75 degree, and (b) the schematic of the effective funneling area in different direction. Funneling in horizontal and vertical directions is defined as FH and FP.....112

# List of Appendices

Appendix 1. The importance of competing nonlasing modes – vertical Fabry Perot modes – in microdisk cavities .....	105
Appendix 2. Definition of the sweeping angles .....	108
Appendix 3. Proof of single-cavity color effect .....	110

# Abstract

With highly controllable optical field confinement, subwavelength-scale structures are capable of manipulating light behavior at UV, visible, and IR wavelengths. This light manipulation further enables ones to improve performance of optical devices such as lasers, photovoltaics, and detectors. In this dissertation, two applications of such subwavelength-scale cavities for improved optical performance will be introduced. First, the lasing threshold and optical property of photonic crystal microdisk lasers is improved in the presence of dielectric nanostructures, and the design concept of the nanostructure further paves the way toward higher efficiency microcavity lasers as light sources for photonic integrated circuits. Secondly, several designed plasmonic nanocavities will be presented in this thesis for spectrum filtering. These plasmonic nanostructures enable ones to achieve multifunctional structural color filters with high efficiency ( $>60\%$ ), good color purity (linewidth $<70\text{nm}$ ), and robust angular response ( $\pm 80^\circ$ ). The proposed plasmonic nanostructures have great potential for structural color filtering in LCD TV displays to further allow highly efficient displays with sharper colors and ultra-small pixel sizes. The proposed plasmonic nanocavities also open up the opportunity for a wide variety of applications such as photovoltaics, nanocavity emitters, miniature hyperspectral imaging, and high sensitivity index sensors.

# Chapter 1 Introduction

## 1.1 Background of subwavelength scale cavities

In 19<sup>th</sup> century, two French scientists Alfred Perot and Charles Fabry invented the Fabry-Perot interferometer. Since then, this design has shown great precision of size measurement, wavelength comparison, and a wide range of applications in metrology and spectroscopy. Fabry-Perot cavities were also demonstrated to be good resonators for optical wave. In 1960s, the first open-sided Fabry-Perot optical resonators were demonstrated experimentally <sup>1</sup>. Based on the optical resonator concept, many researchers such as Charles Hard Townes, Arthur Leonard Schawlow, Prokhorov, and Gordon Gould were able to invent the LASER. Moreover, optical resonators have shown to have very strong field enhancement within the cavities. Such strong light intensity enabled many phenomena that had not been observed in free space optics before.

From 2000s until now, in order to further enhance the field intensity within cavities, scaling down the physical dimension of optical cavities <sup>2-6</sup> has become one of the important research directions in photonics and optics society. Subwavelength cavities can be classified into two main categories in terms of the material: dielectric-based

cavities and metal-dielectric-based cavities. Dielectric-based cavities are cavities built using material with low loss and high indices (refractive index  $> 1$ ) and are able to achieve high-quality-factor modes. The most popular cavities in this category are photonic crystals (PhC) nanocavities<sup>7-10</sup>, nanowire cavities<sup>11,12</sup>, and disk cavities<sup>7,13,14</sup>.

On the other hand, metal-dielectric-based cavities including metal-enclosure cavities<sup>15,16</sup> and plasmonic cavities<sup>5,17-21</sup> have also gained lots of interest. The former type of cavities uses metal as broadband reflectors in order to reduce radiation loss of the optical cavities. Metal-encapsulated nanocavities have led to development of next generation optoelectronic devices, such as miniature lasers and single photon sources. The latter type of the cavities relies on the plasmonic modes, which confines light at the interface of metal-dielectric. This good light confinement at the interface of metal and dielectric materials has Plasmonic nanocavities attracting much attention.

## 1.2 Motivation

The aforementioned optical micro- and nano-structured cavities have been an integral part of the mainstream research topics recently – nanophotonics. Nanophotonics is a research field that discusses light behavior at the nano-scale, and it states that optical

waves behave very different from light propagating in free space. The reasons for such large amount of attention on nanophotonics are shown in the following:

### **1. Free spectral range modification**

By changing the physical dimensions of cavities from the meter and millimeter scale down to the micrometer and nanometer dimension, free spectral range (FSR) of optical resonators will increase, and therefore indicating that FSR is inversely proportional to the cavities' dimensions. This light manipulation helps increase Finesse and FSR, as well as helps manage the number of modes within a certain spectral window of interest.

### **2. Highly confined optical field distribution**

Instead of in relative large scale cavities, light can be tightly confined in micrometer and nanometer scale cavities with reasonably high quality factors (Q). This tight optical confinement leads to localized optical field with high light intensity. Such high light intensity concentration in the subwavelength cavities allows ones to excite the nano and microscale objects very efficiently with intense light.

### **3. Enhanced light-matter interaction**

Based on intense light concentrating on nano- and micro-scale cavities, enhanced

light-matter interaction in both the strong and weak coupling regime can be observed in the nanostructured cavities<sup>19, 22-31</sup>. For the strong-coupling regime, according to Box 1 in the reference<sup>2</sup>,

$$n_0 \propto V, N_0 \propto \frac{V}{Q} \quad (1)$$

, where  $n_0$  indicates the saturation photon number,  $N_0$  represents the critical atom number,  $V$  the mode volume, and  $Q$  the quality factor of the cavities. To achieve strong light-matter interaction, both  $n_0$  and  $N_0$  are expected to be less than unity. Therefore, cavities with small mode volume  $V$  and high quality factor  $Q$  would be desirable to observe strong coupling. On the other hand, in the weak coupling regime, keeping light confined in nanometer and micrometer scale cavities enhances spontaneous emission. The Purcell spontaneous emission enhancement factor describes the degree of spontaneous emission enhancement compared to emitters in free space. The Purcell factor is proportional to  $Q/V$ <sup>32, 33</sup>, and therefore, the smaller cavity size, the stronger the light-matter interaction and more pronounced light manipulation.

## 1.3 Applications

Light manipulation in micro- and nano-structured cavities can be applied to a variety of

applications. First, since the miniature size of the cavities leads to a large FSR and high Finesse, it provides a large operation bandwidth for devices such as interferometers, spectrometers, color filters, and optical add-drop modulators (OADM). Large FSR and high Finesse are also good for laser applications because of less mode competition, less mode hopping effect, and better beam quality.

Second, a tightly confined optical field results in an optical image and light spot size close to or even beyond the resolution limit. It opens up the possibility of super-resolution imaging that could be particularly useful for photolithography<sup>34-37</sup>. Current achievable resolution is sub-20nm. Moreover, since some specially designed nanostructured cavities can trap light very efficiently, they can act as good photon absorbers and light harvesting nanostructures<sup>38-40</sup> and even nanoscale solar concentrators<sup>41, 42</sup>.

Third, increased light-matter interaction in nanostructured cavities alters light behavior and further leads to coupling between light and materials, particles, and even atoms. Nanostructured cavities can be used to study cavity QED and quantum information. Furthermore, the Purcell effect determines the spontaneous emission rate and control over the photonic density of states (PDOS). The manipulation of spontaneous

emission is a very important and necessary effect in real applications<sup>11,43</sup>. Enhanced spontaneous emission intensity can be used for light emitters to create ultra-bright light-emitting diodes and brightness-enhanced fluorophores<sup>23,44,45</sup>. On the other hand, suppressed spontaneous emission can be used to achieve ultra-efficient light sources by removing the unwanted modes and emission at unwanted wavelengths<sup>8,46</sup>. Therefore, nanostructured cavities have a wide variety of applications.

## 1.4 Chapter overview

As described in the previous sections, micro- and nano-structured optical cavities have the ability to manipulate the spectrum, confinement, and the light-matter interaction at optical frequencies. These light manipulation effects allow for many applications and possibilities. The objective of this thesis is to investigate these light manipulating effects in nanostructured cavities. Furthermore, the second goal is to apply these effects to improve the efficiency of microcavity lasers for photonic integrated circuits and achieve better color filters at visible wavelengths for LCD TVs.

In the chapter 2, nanostructured microdisk cavities are introduced. These cavities are shown to be capable of multichannel lasers for reducing the cost of light sources in a

DWDM system. Based on simulation and experiment, these cavities also demonstrate that the spontaneous emission coupling factor into lasing modes ( $\beta$ ) will be enhanced more than 3 times. The discussion is followed by explaining the enhanced  $\beta$  based on spontaneous emission control.

In the chapter 3, plasmonic metal-insulator-metal (MIM) nanoresonators are introduced. By carefully choosing the period of the nanoresonators from 240nm to 360nm, one can achieve color filtering over the entire visible spectrum. Also, the designed color filters can achieve ultra-high resolution and behave as good polarizers. These indicators clearly show that the proposed plasmonic devices are capable of acting as commercial color filters in LCD TVs.

In the chapter 4, for further achieving better color purity control and higher transmission, another plasmonic color filter design is demonstrated in simulation and experiment. We are able to achieve transmission efficiency up to 80% with a full-width at half-maxima (FWHM) of 20nm. The mechanism of FWHM tunability of the transmission peak is demonstrated. Moreover, these color filters are further fabricated as 2-inch devices to demonstrate the possibility of commercialization and manufacturability. In this study, we also identify a potential problem on this design –

angle sensitive color response in the discussion, which will be solved in the design in the chapter 5.

In order to find a solution for long lasting problem in structural colors — angle sensitive color response (namely iridescence), a type of plasmonic nanostructure is proposed and studied in detail in Chapter 5. This nanostructure is also proposed as reflection type angle-independent color filters (AICF). This design of reflection type AICFs has wide color tunability and high resolution color pixels, and the most importantly, angle tolerance up to  $\pm 80^\circ$ . Experimental results of reflection type AICF further proves the angle tolerance and the color tunability. Moreover, the angular response analysis is studied in detail in this chapter.

Chapter 6, followed by the analysis and the study of the angle insensitive plasmonic nanostructure in the chapter 5, several designs for transmission color filters are proposed. All designed plasmonic nanostructures can achieve at least  $\pm 70^\circ$  angle insensitivity. Also, color tunability and color purity on two of the designs (Design I and II) are discussed in detail in the first part of this chapter. At the second part of the chapter, a nanostructure design (Design III) is experimentally demonstrated to show the possibility of angle insensitive color filters.

In the chapter 7, a summary of the research will be included in section 7.1, and the future work of the research work based on the finding in this dissertation will be listed partially at section 7.2.

# Chapter 2 Photonic crystal microdisk (PCM) lasers

## 2.1 Introduction and motivation

Microdisk cavities are essential components in the optical communication, information storage<sup>47 48</sup>, and optical interconnect<sup>49</sup>. In order to achieve densely integrated photonic circuits, researchers have been pursuing semiconductor lasers in miniature dimension<sup>5051</sup>. In the dense wavelength division multiplexing (DWDM) system, laser light sources play important roles, and therefore the efficiency of lasers is important. To make high-efficiency light sources, high spontaneous emission coupling factor ( $\beta$ ) is one of the keys. One approach for large  $\beta$  is to reduce the number of modes by scaling down the device scale. However, smaller diameters of the microdisk cavities lead to large radiation loss, which therefore increases the lasing threshold. Current microdisks have unexceptional spontaneous emission coupling rates less than 15%<sup>4 752 53 54</sup>. Therefore, microdisk light emitting devices that have large  $\beta$  are important to pursue for better-performing light sources for photonic integrated circuits (PIC).

Moreover, cost of light sources for WDM and DWDM systems on the future photonic integrated circuits is important. One of the common approaches to multi-channel light

sources in WDM and DWDM is multiple devices with single wavelength channel operation. This scheme complicates the real photonic device integration and further increase cost. Therefore, cost effective multi-channel light sources are on demand.

Here we propose a concept of microcavity laser design based on microdisk cavities that are capable not only of large  $\beta$  but also of multi-channel light sources on single device with controllable light source channel spacing. In this work, we first introduce the proposed structure and simulated  $\beta$  control based on Finite difference time domain (FDTD) method. This structure is able to achieve small device diameter of  $1.22D/\lambda$  with mode volume  $0.06\lambda^3$ . Secondly, we experimentally demonstrate this design at room temperature, and characterize that the demonstrated device has spontaneous emission coupling rate ( $\beta$ ) of 50% for two disks. Forth, we discuss controllable channel spacing from 1nm to 5nm regarding to the geometrical change. Finally, we conclude this work with the performance and the vision of the design.

## 2.2 Methods and Results

The laser cavity design is illustrated in Figure 2.1(a). First we performed the mode distribution of a two-stack photonic crystal microdisk cavity with diameter of  $1.2\mu\text{m}$

and an undercut of 300nm using finite difference time domain (FDTD) method. By tweaking the top and bottom disks with thickness being different, we are able to control number of modes within the gain spectrum. In this case, we first design single optical mode within TE-dominant quantum-well gain spectrum. Within the full width at half maximum (FWHM) of the InGaAs quantum well gain spectrum from 960nm to 980nm, it supports a single WGM mode TE(9,1) at wavelength of 970nm. Fig. 2.1 also shows the top view of the mode profiles of WGM TE(9,1). Another mode is located at 995nm, which is far away from the FWHM of the gain spectrum. We further investigate the enhanced coupling rate of the emitter emission into the lasing mode in the proposed device design based on FDTD simulation<sup>52 53</sup>. Dipole emitters are placed at various radial positions in the microdisk to probe the position dependence of the coupling rate. The coupling rate of spontaneous emission into WGM mode ( $\beta$ ) as a function of position with respect to radius (R) is shown in the Figure 2.1(b). First, it indicates that, when an emitter is close to the microdisk center, the coupling rate declines. The emitter at the radial position of 0.15R has half the coupling rate compared to that at 0.75R. Second, emitters couple to the two stack photonic crystal microdisk cavity much more effectively than coupling to a single disk. At any position away from the center of the disk more than 0.35R, a two-stack device has coupling rate of 0.45, which is almost three times higher than the reported  $\beta$ <sup>52 53 4 7</sup>.

We design and fabricate the multiple stack microdisk lasers shown in Figure 2.1(a) on a substrate with GaAs/AlGaAs stack structures, which have two InGaAs quantum wells located at the middle of the top GaAs layer. The epitaxial structure GaAs/InGaAs QWs/GaAs /Al<sub>0.75</sub>Ga<sub>0.25</sub>As /GaAs/ Al<sub>0.75</sub>Ga<sub>0.25</sub>As was grown with metal-organic vapour-phase epitaxy (MOVPE) technique on an n<sup>+</sup> GaAs substrate by Landamark Technology Company. Two quantum wells (QWs) are located at the center of the top GaAs stack. AlGaAs is selectively etched to make air gap as the low index layer of the PCM. A scanning electron micrograph image of the fabricated laser device shows in Fig. 2.1(c). To fabricate the device, first a 300nm oxide film is deposited with plasma-enhanced chemical vapor deposition (PECVD). Then the electron beam lithography (EBL) is performed, followed by Ni deposition and a lift-off process. The resulting Nickel disk pattern is used as a hardmask in the following dry etching of the whole stack with inductively coupled plasma reactive ion etching (ICP-RIE). The PCM structure is realized with the final step of selective etching of Al<sub>0.75</sub>Ga<sub>0.25</sub>As in dilute buffered hydrofluoric acid (BHF).

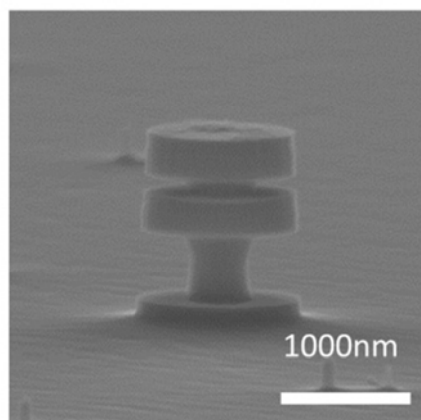
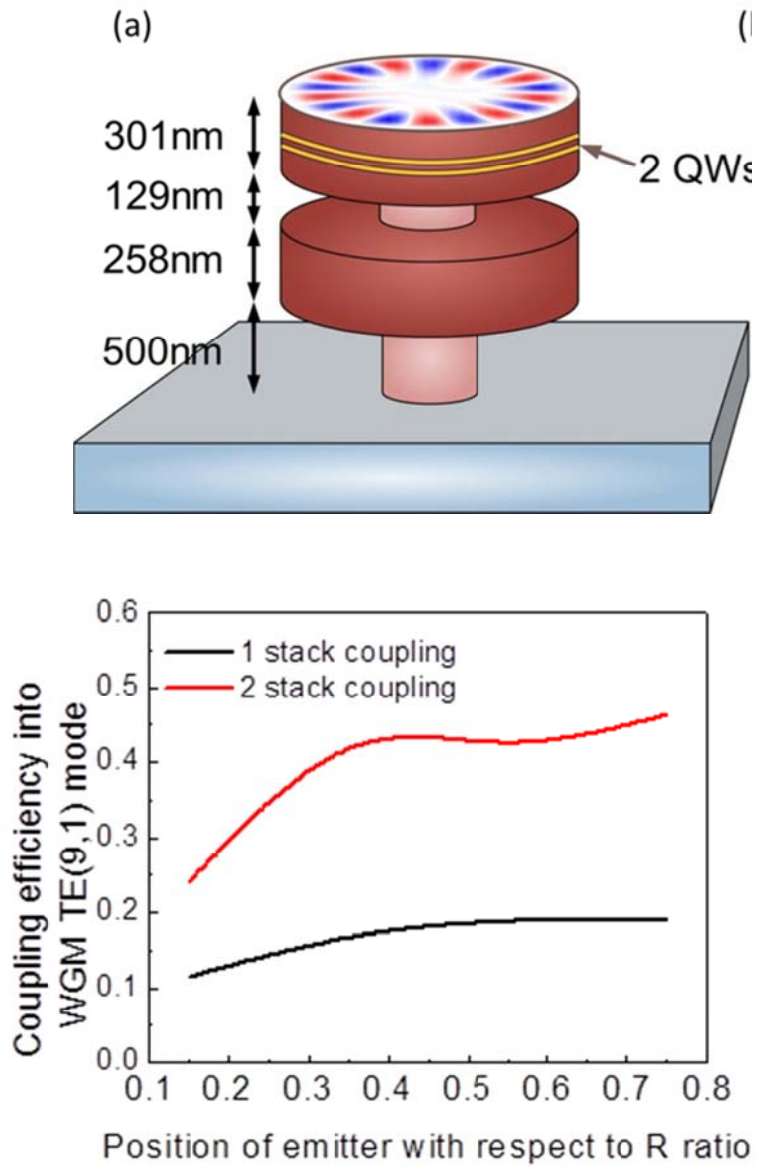


Fig. 2.1 (a) Schematics of the photonic crystal microdisk (PCM) laser and the field distribution of the WGM mode TE(9,1) (b) Simulated spontaneous emission coupling

factor into lasing mode based on FDTD method (c) Scanning electron micrograph image of PCM laser.

The measurement setup is a micro-luminescence ( $\mu$ -PL) system. A Ti:Sapphire pulsed laser excites the active region of the laser device through an objective lens (NA=0.9). The diameter of the pumping beam is focused down to 5 $\mu$ m. The signal is then collected by the same objective lens and is delivered to a monochromator equipped with a cooled InGaAs detector.

We demonstrated a single mode PCM laser with a disk diameter of 1.2 $\mu$ m at room temperature. The photo-luminescence (PL) spectra below and above threshold are presented in the logarithmic scale in the Fig. 3(a). Single mode lasing is observed at wavelength of 969nm, in good agreement with the simulation. The 3dB bandwidth is 1.2nm, corresponding to active Q of 890. Moreover, the clear cavity peak with suppressed broad spontaneous spectrum below threshold verifies that the spontaneous emission is dominated by the lasing WGM mode in the PCM structure. Also, the broadband background signal from 960 to 1000nm on the same curve indicates that in two-stack PCM the spontaneous emission into vertical direction is not perfectly suppressed. By integrating the intensity spectrum within the lasing peak, the threshold curve is presented in Fig. 3(b). The threshold of the two-stack PCM laser is 16mW.

The purcell factor  $F$  and spontaneous emission coupling efficiency  $\beta$  can be fit simultaneously<sup>55</sup> based on the rate equations<sup>56</sup>, shown in Fig. 3(b). In the fitting,  $\tau_{sp}=2\text{ns}$ ,  $v_s=2\times 10^4\text{ cm/s}$ , and  $G=2100\times v_g\times \ln(N/1.8\times 10^{18})$ , where  $v_g$  is group velocity of light. The colored solid curves in this graph are calculated in log-log scale for purcell factor of 5.3, whereas the threshold curve in the logarithmic scale is depicted with triangular marks in this figure.  $\beta$  of the two-stack PML is fitted to be 0.5. This  $\beta$  value is enhanced 3 times than the typical value 0.15 for a single microdisk cavity<sup>4</sup>. This increasing  $\beta$  can be explained in the following. The suppression of photonic density of state (PDOS) in vertical direction helps improve the spontaneous emission coupling rate into WGM lasing mode. This experimental result matches with the calculated spontaneous emission coupling efficiency 0.45.

The  $\beta$  value enhancement is attributed to suppression of the photonic mode density. It is modified effectively by truncated 1D PhC structure<sup>57</sup>. The detail will be elaborated in the following section.

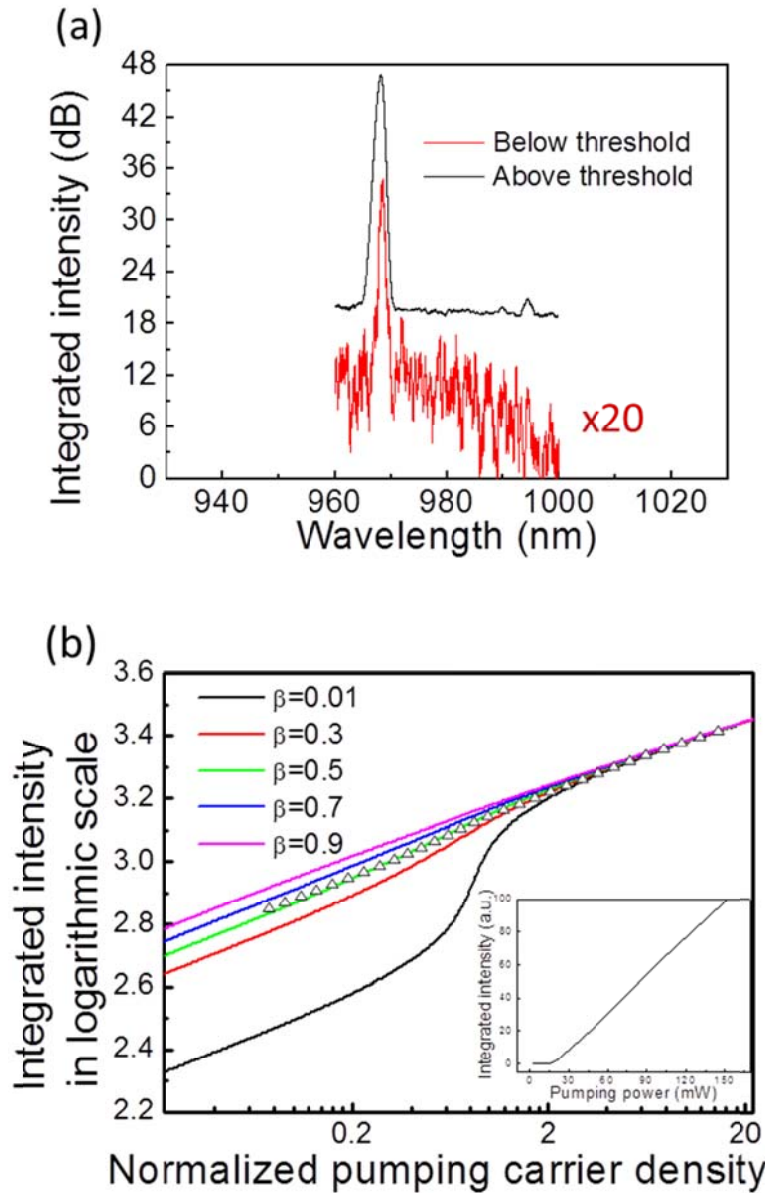


Fig. 2.2 (a) Threshold spectra below and above threshold of the two-stack device in the logarithmic scale (b) The calculated threshold curve with various  $\beta$  (colored solid lines) and the experimental L-L curve (triangle dots). Inset illustrates the experimental L-L curve in linear scale.

## 2.3 Discussions of high $\beta$

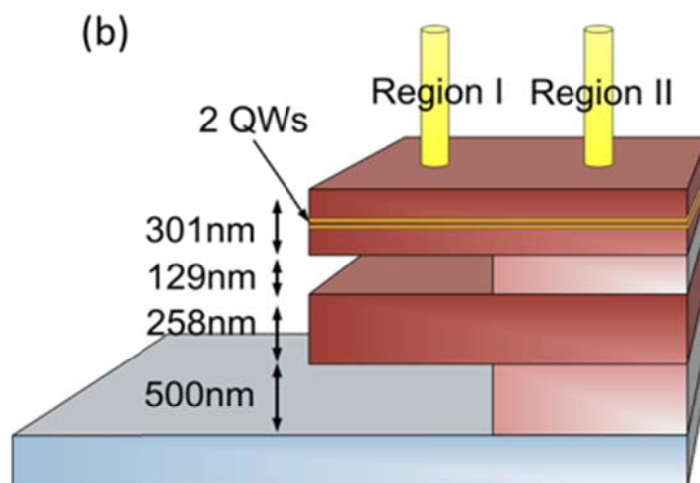
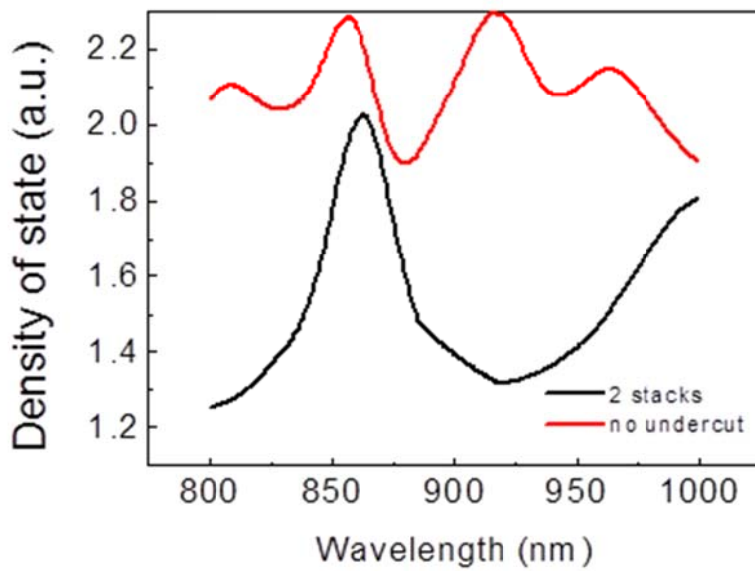
To explain the large  $\beta$  in PCM, we dive into what causes low  $\beta$  in the conventional microdisk cavities. The primary reason for small  $\beta$  of WGM in microdisks is strong competition between lasing and nonlasing Fabry-Perot modes (see Appendix I). Clearly, to significantly improve  $\beta$  of the lasing WGM mode, suppressing radiation into all the undesirable modes becomes crucial. This can be done by reducing spontaneous emission rate  $\gamma_{nontasing}$ . According to Fermi's golden rule<sup>58</sup>, manipulation of the photonic density of states controls spontaneous emission. Therefore, large  $\beta$  to the lasing mode can be achieved by minimizing the mode density of the other competing and non-lasing modes, e.g., the Fabry-Perot (FP) modes in microdisk cavities.

Theoretically, the mode density can be modified effectively even by truncated 1D PhC<sup>57</sup>, where the PhC structure is terminated by a bulk material with only finite pairs. Herein we first quantitatively investigate the mode density modification in a 1D PhC with different high-index and low-index pairs. Based on COMSOL simulation and calculation in<sup>59</sup>, the mode densities with various numbers of the 1D PhC pair show in Fig. 2.3(a). As expected, the DOS in a single disk is flat within the spectrum of interest, and therefore does not have effect on mode density suppression. This result indicates that, instead of coupling into lateral propagation modes, photons in a single stack microdisk prefer to emit through the channel of Fabry-Perot modes along vertical

direction. Therefore, it leads to reducing the spontaneous emission in the WGM modes. In contrast, 1D PhC with more than two pairs of high-low index stacks can strongly suppresses the density of states (DOS) along the vertical direction between the wavelength of 870nm and 1000nm, where it is located in the quasi-photonic bandgap.

To experimentally prove this idea, we conducted a micro -photoluminescence ( $\mu$ PL) measurement on a device shown in Fig. 2.3(b). The device is fabricated with selective wet etching of the AlGaAs layer to form undercut structures. The region with undercut forms truncated PhC due to large refractive index difference between the GaAs layers and the air gaps. The sample is measured with an excitation laser (Ti:Sapphire pulse laser) at region I and region II. By using the signal from region II as reference (detail in Part 3 of supplementary material), the density of states (DOS) in region I is characterized by the ratio of the signal from region I to that from region 2. Fig. 2.3(c) shows the calculated and measured ratio of DOS between region I (two pairs of GaAs/air stacks) and II. Both simulation and experiment show a spectrum valley between 900nm and 990nm. This is a clear evidence of DOS suppression in the 1D PhC structure. The mismatch between simulation and the measurement results at wavelength of 975 nm might be due to refractive index change of quantum wells due to proximity of interband transition band not considered in the simulation. On the other

hand, the DOS for a device with single GaAs layer is shown in Fig. 2.3(c), which depicts a flat spectrum DOS ratio. Clearly, the DOS can be effectively modified in the photonic crystals with more than one pairs of dielectric stacks. The suppression of DOS in the vertical direction will help spontaneous emission coupling to the WGM modes more effectively.



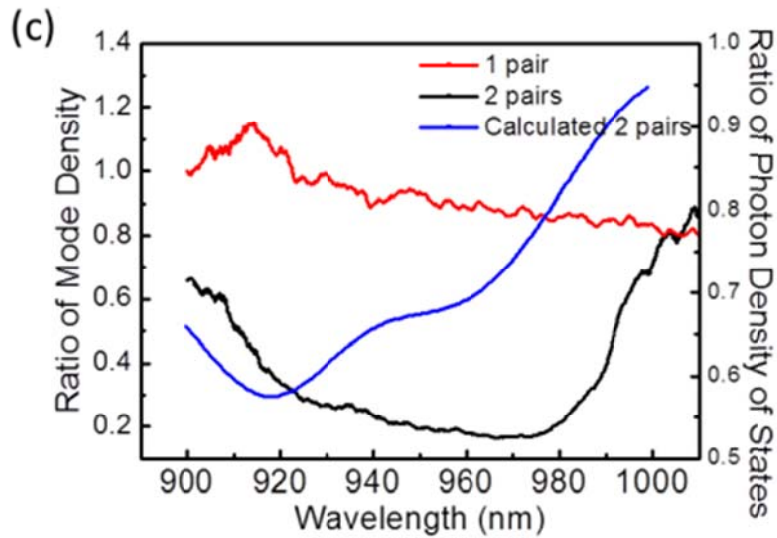


Fig. 2.3 (a) Mode density modification in a 1D PhC with two pairs (b) The schematics of the density of states measurement (c) calculated and measured ratio of DOS for single and double stack of microdisk.

## 2.4 Multi-channel microdisk lasers

Multiple stack microdisk lasers have been demonstrated as single mode lasers in the previous section. On the other hand, some applications such as the light sources in the WDM and DWDM system prefer a single device that works for multiple wavelength channels with channel spacing from 0.2nm to 5nm. The usual approach is to fabricate multiple single-wavelength operating devices<sup>60</sup>. For instance, an 8-channel device requires eight single wavelength operating devices. The channel spacing is determined by the size of each ring. This approach is capable of large tuning range of the channel

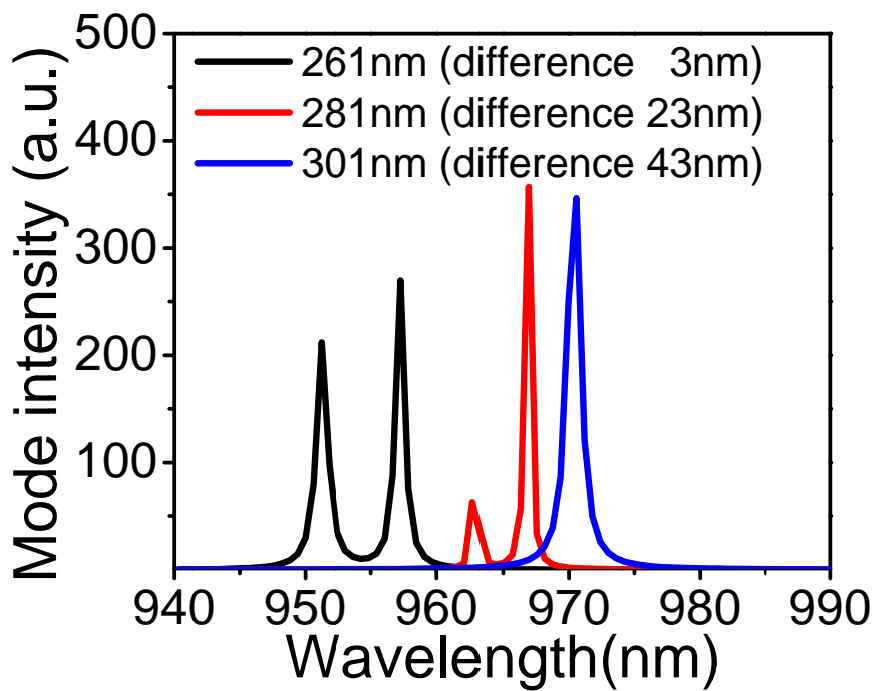
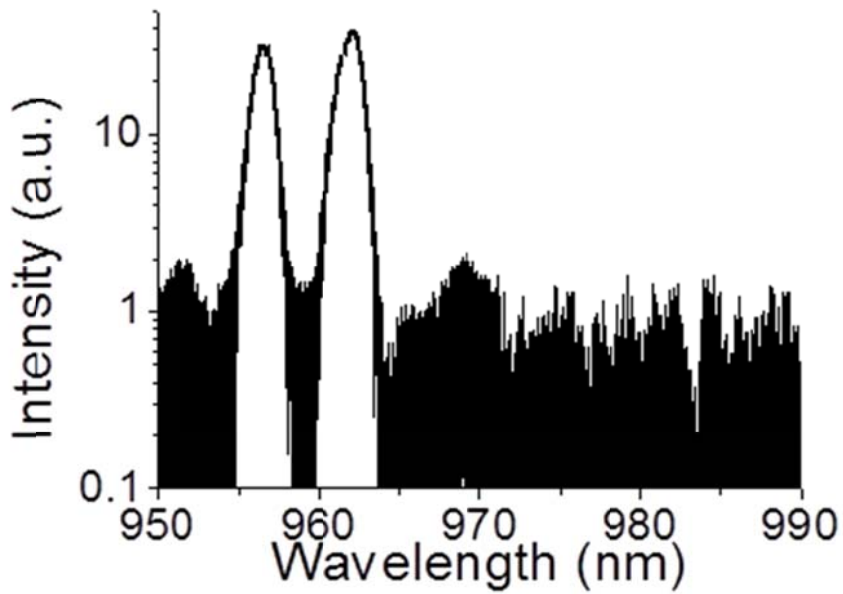
spacing. However, this approach leads to narrow manufacturability tolerance for ring/disk size. This precise control of the diameter of each device leads to enormous cost.

In order to reduce the fabrication difficulty and cost, we propose that the multi-stack microdisk lasers that are able to adjust the lasing channel spacing by controlling the spacing between neighboring disks. This channel spacing control strategy is feasible since the epitaxial growth can achieve very accurate control. Moreover, this strategy reduces required space for multi-channel devices by using vertically integrated microdisks. Herein, we fabricated and characterized a vertically 2-stack microdisk laser with same top and bottom thickness (258nm) but with no undercut into AlGaAs layers. We observe splitting modes in the lasing spectrum in Figure 2.4(a). The splitting modes are located at 956.5 and 961.9nm with mode spacing of 5.4nm.

Figure 2.4 (b) shows calculated mode splitting evolution in regards to the thickness of top microdisk from 301 nm, 281nm to 261 nm, given the bottom disk thickness of 258nm. We observe clearly that an emerging cavity mode at shorter wavelength when the top disk thickness approaches the thickness of the bottom microdisk. The resulting lasing mode evolution agrees well with peak shift and mode spacing in above

experiments. Simulations show that lasing mode is located around 970.5nm when the top disk is 301nm and bottom is 258nm. On the other hand, when the top disk thickness reduces to 261nm, lasing modes are located at 951.2 and 957.1nm. The mode splitting is 5.9nm, close to the experimental spacing 5.4nm. Additionally, mode splitting is determined by the thickness mismatching between top and bottom disks. The mode splitting from null, to 4.1nm, further to 5.9nm when top disk thickness decreases from 301nm, 281nm, to 261nm. The field distribution (Hz component) is furthermore used to investigate the coupling between top and bottom disks. The Hz field intensity for modes in Figure 2.4(c), (d), (e) indicates the cross-section view of field distribution of the only mode in top disk 301nm, and two coupled modes (at wavelength of 957.1nm and 951.2nm) in top disk 261nm, respectively. The mode coupling indicated in Figure 2.4(d) and (e) can be explained by coupled mode theory. According to coupled mode theory, mode splitting effect is not only determined by the degree of momentum mismatch but also by the physical separation between two waveguides or resonators. The simulation also shows that the mode spacing can be adjusted from 5.4nm to 1nm by changing the separation thickness from 129nm to 320nm. Apart from the tunability of channel spacing, another important factor of being multi-channel devices is the equal lasing power level. Here we also foresee the possibility of equal power level for application of Photonic integrated circuits in Figure

2.4(a). In this Figure, intensity of the modes 951.2nm and 957.1nm is 31.1 and 37.9, respectively. To further improve the equal power and slope efficiency for coupled modes, we have to address the bandwidth of the gain spectrum, which is not discussed here.



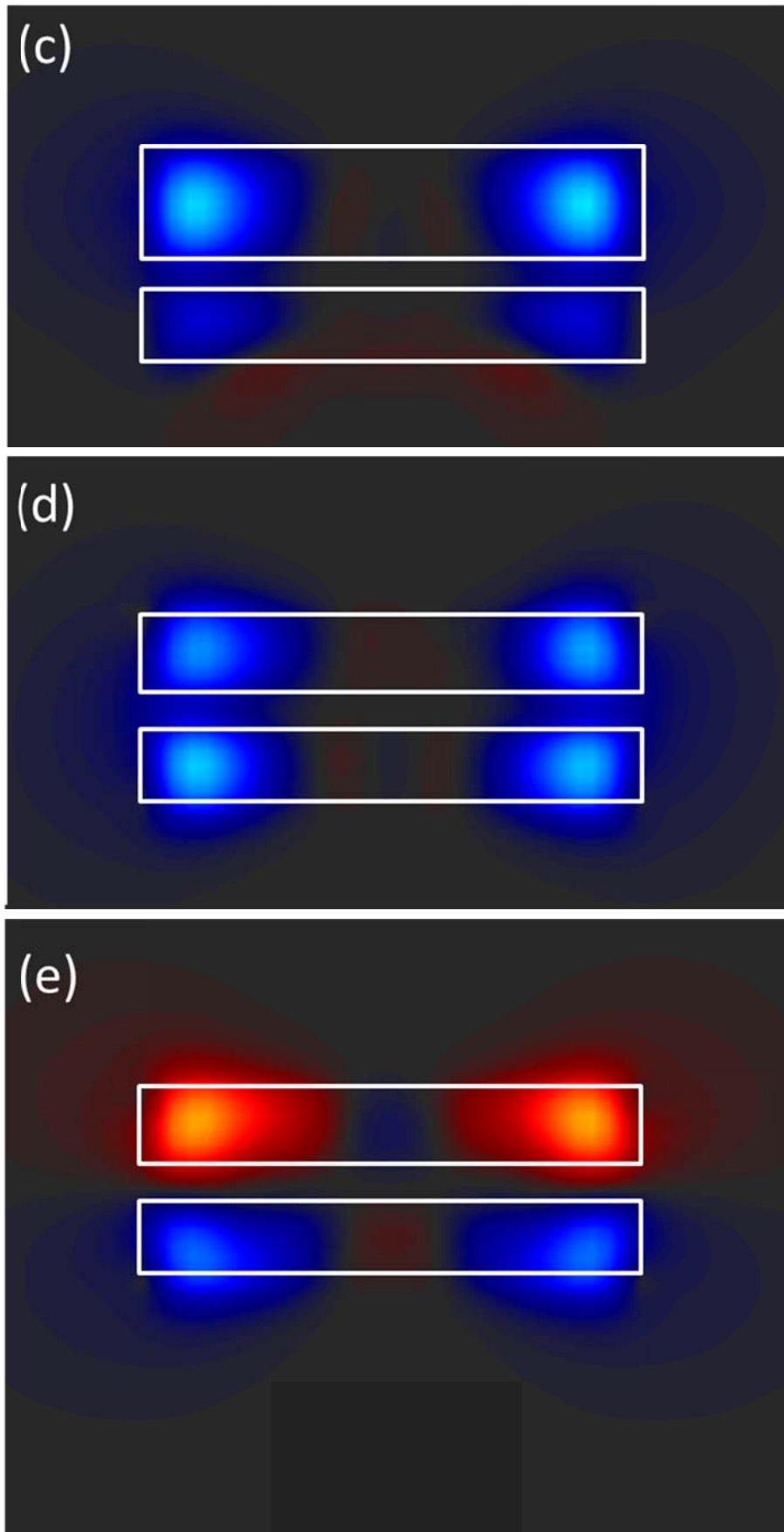


Figure 2.4 (a) experimental lasing spectrum for a vertically 2-disk microdisk lasers with

both the top and bottom disk thickness 258nm. (b) the calculated cavity mode spectrum of the 2-disk microdisk cavities with various thickness of top disk 261, 281, and 301nm, given the bottom disk thickness of 258nm. (c) Hz field distribution of the single mode at top disk thickness of 301nm (cross-section), (d) Hz field distribution of the mode at 957.1nm with top disk thickness of 261nm (cross-section), (e) Hz field distribution of the mode at 951.2nm with top disk thickness of 261nm (cross-section).

## 2.5 Summary

We discussed the photonic crystal microdisk laser cavities in several aspects. First, this vertical 1D photonic crystals design is capable of enhancing spontaneous emission coupling factor into lasing modes ( $\beta$ ) for microdisk cavities. By using 1D photonic crystals in microdisk structure, the spontaneous emission into unwanted modes is suppressed. This  $\beta$  enhancement can increase the efficiency of microdisk based light sources and further reduce lasing threshold. Another important demonstration is that the mode splitting in this structure is easily achievable. By adjusting the spacing between top and bottom disks, as well as the thickness difference between these two disks, we are able to achieve multi-channel lasing and further reduce the cost of photonic integrated circuits.

# Chapter 3 Plasmonic nanoresonators for high-resolution color filtering and spectral imaging

## 3.1 Introduction and motivation

Apart from the resonance in dielectric cavities and their applications in chapter 2, the focus in this chapter is on plasmonic nanocavities. Even though metallic nanocavities have high loss, plasmonic cavities have ability to confine light very tightly, which is as small as 20nm. Due to this good confinement, one can achieve much smaller cavities than dielectric based cavities. In this chapter, a type of plasmonic nanostructured cavity will be introduced and applied to be potential replacement of commercial pigment color filters.

Surface plasmons (SPs) and related plasmonic nanostructures have gained considerable interest with the development of nanofabrication and characterization techniques<sup>61-67</sup>. SPs are essentially charge wave existing in the coupling of light to the collective oscillation of electrons at the metal and insulator interface. By exploiting plasmonic nanostructures, such as nanohole or nanoslit arrays, efficient conversion between photons and plasmons can be controlled at subwavelength scale, which may provide

novel solutions to traditional optical processes such as color filtering and spectral imaging<sup>68</sup>. Recently, these effects have been reported in a metallic nanohole array for filtering color by tuning the resonant transmission peaks at the visible spectrum<sup>69</sup>. However, the transmission band of such filters are relatively broad and do not satisfy the requirement for the multiband spectral imaging. Other approaches such as nanoslits combined with period grooves<sup>70</sup> or in a metal – insulator – metal (MIM) waveguide<sup>71</sup> also demonstrate color filtering. However, in these structures, two neighboring output slits have to be separated by additional structures or by specific coupling distances (both about several micrometers, causing attenuation due to metal absorption loss); therefore, the device dimension and efficiency are restricted. Furthermore, because of the thick metal film used in these structures, the absorption loss from light input and output of the MIM waveguide further decreases the device efficiencies to < 10 %. Such a value does not satisfy the requirement for practical display applications. Among the above efforts, filters generated by MIM waveguide resonators are of particular interest. MIM waveguide geometries have the ability to support SP modes at visible wavelengths and have been widely investigated for various applications, such as guiding waves at subwavelength scale<sup>72-75</sup>, concentrating light to enhance the absorption for photovoltaic applications<sup>76,77</sup>, achieving a near-field plate for super-resolution at optical frequency<sup>78-81</sup> or composing metamaterials for magnetic

resonance and negative refraction<sup>78-81</sup>. In addition to enabling efficient subwavelength optical confinement, compared with other nanostructures, the top and bottom metal layers of MIM waveguides can be potentially integrated as electrodes in a straightforward manner in the electro-optic system, both of which can compact the device size.

In this chapter, the design of plasmonic MIM nanoresonators capable of spectrum filtering for various colors across the entire visible band is demonstrated. The design principle can also be applied to other wavelength range. The key concept is to use nanoresonators to realize the photon – plasmon – photon conversion efficiently at specific resonance wavelengths. Compared with the aforementioned spectrum filtering methods, our new design significantly improves transmission, narrower pass bandwidth and compactness. Moreover, the filtered light is naturally polarized, making it very attractive for direct integration in liquid crystal displays (LCDs) without a separate polarizer layer. In a nutshell, this plasmonic nanoresonator based spectrum filtering device can reduce the number of optical components in LCDs by integrating polarizers, color filters, and electrode into single device.

## 3.2 Design of plasmonic nanoresonators for color filtering

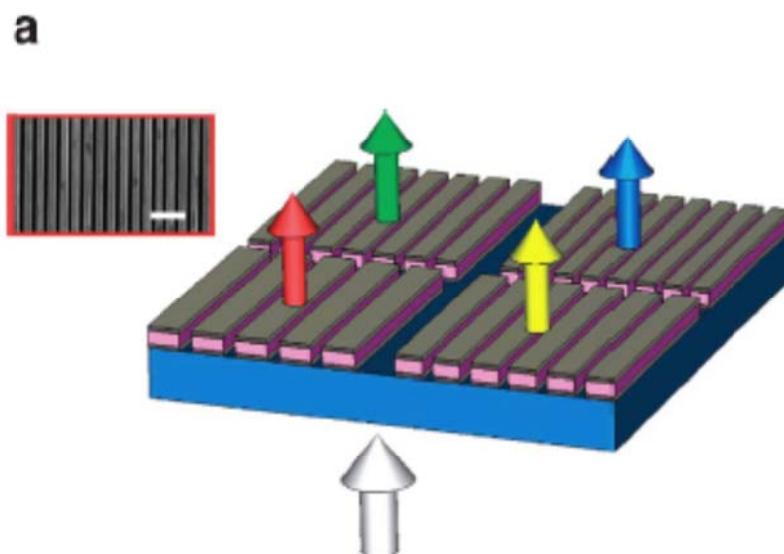
Figure 3.1(a) presents the schematic diagrams of the proposed nanoresonators. For simplifying fabrication process, the device is designed as a subwavelength periodic MIM stack array on a magnesium fluoride ( $\text{MgF}_2$ ) transparent film with period  $P$ . For each MIM stack, a 100 nm-thick zinc selenide ( $\text{ZnSe}$ ) layer is sandwiched by two 40 nm-thick aluminum ( $\text{Al}$ ) layers, wherein the thickness of the dielectric core is determined on the basis of the spatial extension of SP waves inside the  $\text{ZnSe}$  layer at the visible spectrum. The 100 nm-thick  $\text{ZnSe}$  layer ensures the efficient coupling of SP modes at the top and bottom edges of the stack, whereas the 40 nm-thick  $\text{Al}$  layer prohibits the direct transmission of the incident light. The duty cycle of the stack array is about 0.7.

The bottom  $\text{Al}$  grating is used to couple selectively the incident optical wave into surface plasmon waveguide modes by diffraction, whereas the top  $\text{Al}$  grating efficiently reconverts the confined plasmons to propagating waves by scattering and transmits the light to the far field in the forward direction.

For TM-polarized waves (the  $E$ -field is perpendicular to the  $\text{Al}$  grating direction), the

transverse magnetic plasmon dispersion of the Al / ZnSe / Al stack array is plotted in Figure 1b . Here we only consider the normal incidence and therefore the stack period is related to the plasmon transverse wavevector as  $P = 2\pi / k_x$  by the  $\pm 1$ st order diffraction based on the momentum conservation law. From this figure, it can be clearly seen that the SP antisymmetric mode has a near-linear dispersion across the entire visible range. Therefore, the SP antisymmetric modes can be used as intermediates to couple the incident plane wave selectively in and scatter the confined SP modes out to the far field. The close-to-linear dispersion made it very easy to design filters for any colors across the entire visible spectrum range. As an example, the red, green and blue spots in Figure 3.1(b) represent the three primary RGB colors. They have different transverse wavevectors that correspond to specific stack periods by the  $\pm 1^{\text{st}}$  order diffraction. The calculated transmission spectra for RGB colors show in Figure 3.1(c). The corresponding period of the stack is 360, 270 and 230 nm, which is well within the current micro and nanofabrication technologies feasibility. On the other hand, the TE-polarized light (the  $E$ -field is parallel to the Al wire direction) does not support the excitation of SP modes and thus there is no obvious light conversion process. As a result, the TE-polarized light is strongly suppressed at resonance wavelengths and the transmissions are extremely low. This indicates that the proposed transmission color filters can simultaneously function as polarizing optical components,

a highly desirable feature for display applications. Figure 1d shows the simulated time-average magnetic field intensity ( $H$ -field and electric displacement ( $D$ -field, arrow) profiles in one MIM stack corresponding to the red spot in Figure 3.1(b). The TM-polarized incident light has a resonance peak wavelength of 650 nm and the stack period is 360 nm. The magnetic field intensity shows that most of the incident light is coupled into anti-symmetric waveguide modes with maximal intensity near the edges of both top and bottom Al gratings, which supports our design principle. From the electric displacement distribution, we can see that the efficient coupling of incident light to the SP anti-symmetric modes is realized by the strong magnetic resonance response in each sandwiched MIM stack, as in the case of a previous report<sup>79</sup> in which the electric displacement field forms a loop and results in strong magnetic fields opposing that of the incident light inside the dielectric layer.



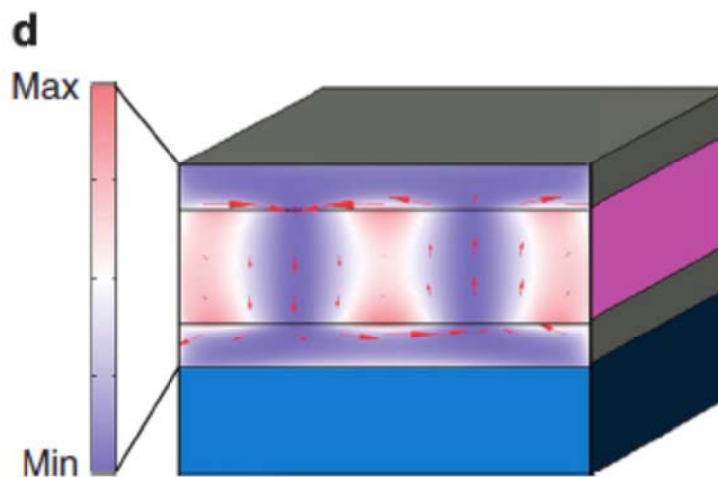
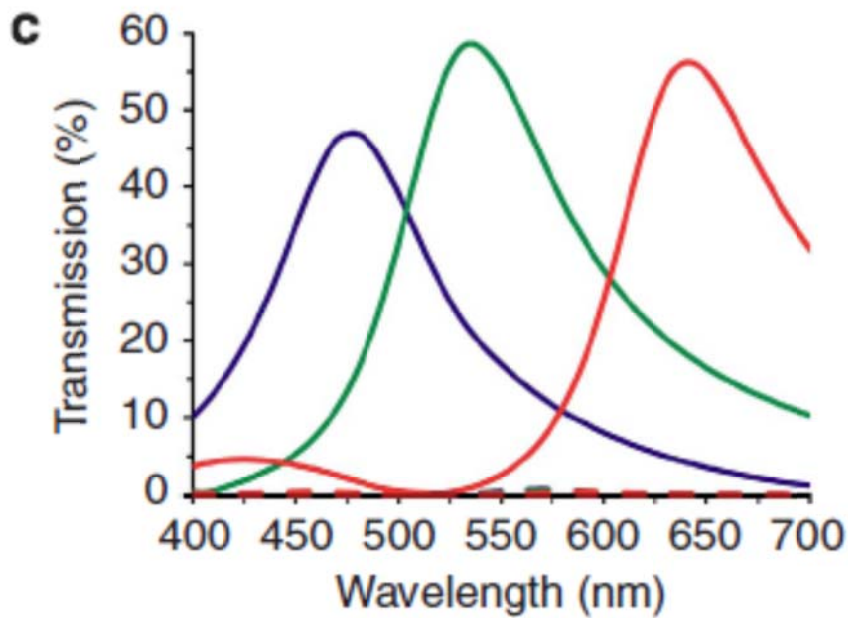
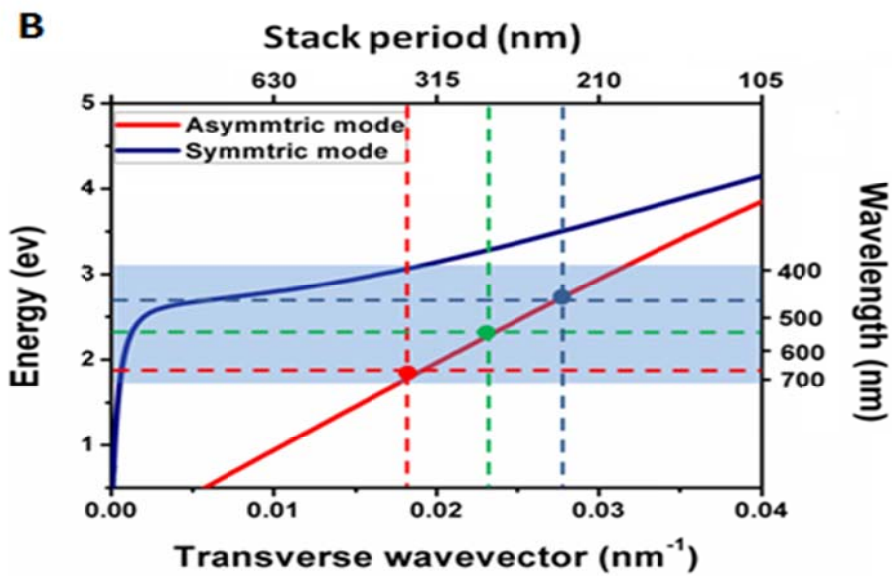


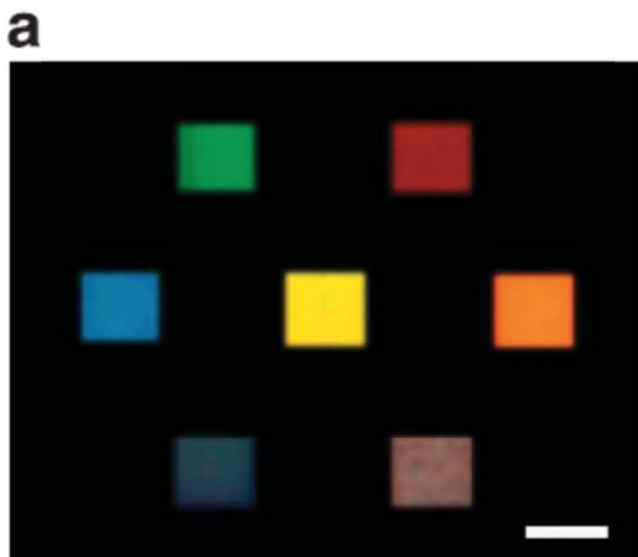
Figure 3.1 Plasmonic nanoresonators formed by MIM stack arrays. (a) Schematic diagram of the proposed plasmonic nanoresonators. The white arrow represents the incident white light and the red, yellow, green and blue arrows represent the transmitted filtered light from the different stack arrays. Grey, pink and blue in the structure indicate the material of aluminum (Al), zinc selenide (ZnSe) and magnesium fluoride ( $\text{MgF}_2$ ) respectively. Inset is the scanning electron microscopy image of the fabricated device and white scale bar represents  $1\mu\text{m}$ . (b) Plasmonic waveguide dispersios in MIM stack array. Red, green and blue dots correspond to the case of filtering primary RGB colors. Red and blue curves correspond to anti-symmetric and symmetric modes respectively. The shaded region indicates the visible range. (c) Simulated transmission spectra for the RGB color filters. The solid and dash curves correspond to TM and TE illuminations respectively. The stack period for RGB filters is 360, 270 and 230 nm. (d) Cross-section of the time-average magnetic field intensity and electric displacement distribution (red arrow) inside the MIM stack at a peak wavelength of 650 nm with 360 nm stack period. The colors on the right side represent the constitutive materials, defined as in (a).

Figure 3.2(a) shows the optical microscopy images of the seven  $10\mu\text{m}$  by  $10\mu\text{m}$  square-shaped plasmonic color filters illuminated by the white light. The filters are fabricated using focus ion beam (FIB) milling of a deposited Al / ZnSe / Al stack on an  $\text{MgF}_2$  substrate. The color filters have the stack period changing from 200 to 360 nm, corresponding to the color from violet to red. The measured transmission spectra of RGB filters are given in Figure 3.2(b), which agrees well with the simulation results

shown in Figure 3.1(c). For TM illumination, stack arrays show the expected filtering behavior with absolute transmission over 50 % around the resonant wavelengths, which is several orders of magnitude higher than those of previously reported MIM resonators<sup>82</sup>. This transmission is comparable with the prevailing pigment color filter used in an LCD panel, but the thickness of the plasmonic device is 1 or 2 orders of magnitude thinner than that of the pigment one. The relative reduced transmission for blue color results from larger material loss of ZnSe in the shorter wavelength range. The full-width at half maximum (FWHM) of the passbands is about 100 nm for all three colors. On the other hand, these devices strongly reflect TE-polarized light, as in wire-grid polarizers<sup>83</sup>. Therefore, the transmission of TE-polarized light is suppressed as shown in Figure 3.2(b). This feature indicates that the structure can act as the roles of color filter and polarizer simultaneously, whose multi-functionality could greatly benefit the LCD by eliminating the need of a separate polarizer layer. In addition, the conductive nature of the Al grating also implies that a separate transparent conductive oxide layer used in LCD module may not be necessary, as was demonstrated in our previous work on metal-wire-based transparent electrodes<sup>84, 85</sup>.

Besides the standard square color filters, one can use different nanoresonator arrays to form arbitrary colored patterns on a micrometer scale. As a demonstration, a

University of Michigan logo with yellow character ‘M’ in a navy blue background is shown in Figure 3.2(c). The pattern size of the ‘M’ logo measures only  $20\ \mu\text{m} \times 12\ \mu\text{m}$  and uses two periods: 310 nm for the yellow letter M and 220 nm for the navy blue background. The optical microscopic image of the pattern illuminated with the broad band light source is shown in Figure 3.2(d). A clear-cut yellow ‘M’ sharply contrasts the navy blue background. It is important to note that the two distinct colors are well preserved even at the sharp corners and boundaries of the two different patterns, which indicates that our color filter scheme can be extended to ultra-high-resolution color displays.



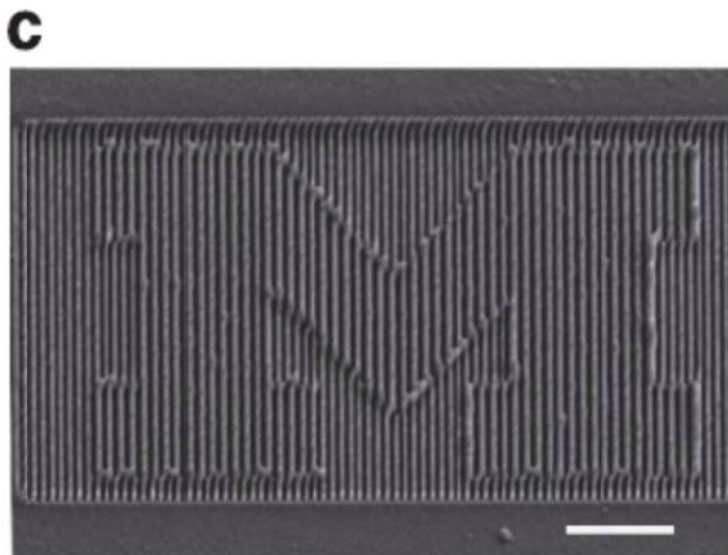
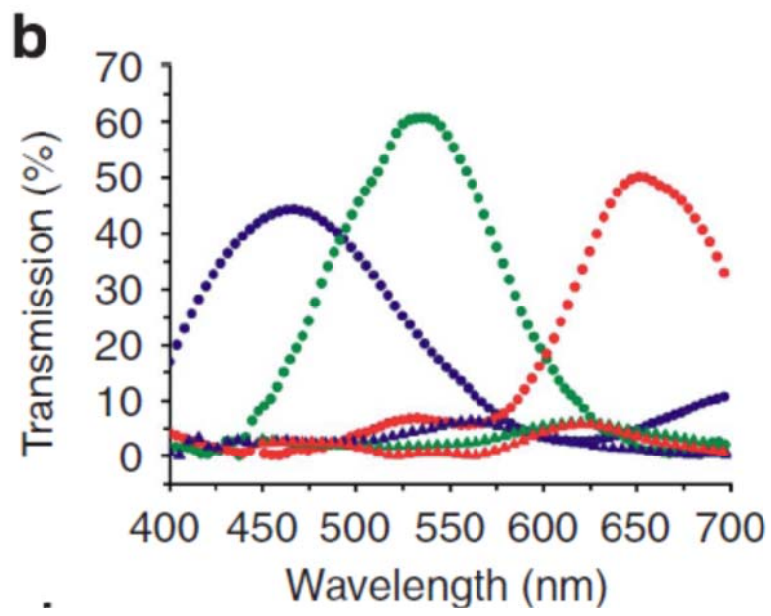


Figure 3.2 Plasmonic color filters. (a) Optical microscopic images of seven plasmonic color filters illuminated by white light. Scale bar: 10  $\mu\text{m}$ . (b) Experimentally measured transmission spectra of three fabricated color filters corresponding to the R, G, and B colors. The circle and triangle correspond to TM and TE illuminations respectively. (c) Scanning electron microscopy image of the pattern 'M' formed by two stack periods. The periods of the navy blue background and the yellow character are 220 and 310 nm, respectively. Scale bar: 3  $\mu\text{m}$ . (d) Optical microscopy image of the pattern illuminated with white light.

Inspired by the clear-cut color at the sharp corner of University of Michigan logo, we further address the following question: how many slits are necessary to render the color filtering effect? We performed simulation and experiments to investigate the relationship between the slit number and the filtering effect. The inset of Figure 3.3 shows the microscope images of the samples with 2, 4 and 6 slits (which means 1, 3, and 5 stacked nanoresonators from the bottom to the top) for green and red color filters. The center-to-center distance between the neighboring slits for green and red filters is 270 and 360 nm, respectively, with slit width about 80 and 100 nm. Amazingly, even the structures with only two slits (or single nanoresonator) exhibit distinct colors. With more slits, the green and red colors become better defined and much brighter. This conclusion agrees well with the simulation results shown in Figure 3.3. This

interesting behavior can be explained by the resonance of the SP waveguide modes. When the incident light is coupled into MIM surface plasmon waveguide modes through the bottom slits, the counter propagating SP waves inside the insulator layer from different slits would interfere along the waveguide direction, in a manner similar to an earlier work<sup>86</sup>. Transmission will be enhanced for constructive interference at the top slits and suppressed for destructive interference. Fundamentally, the filtering effect of the stack array with infinite slits can also be ascribed to the multiple interferences of SP waves from each slit. The main difference between structures having a few slits and infinite slits is that the latter can efficiently couple the incident light into SP antisymmetric modes through momentum matching by diffraction, and therefore the efficiency would be much higher. The above analysis and experimental results indicate that very compact structures with just a few slits can still perform the color filtering function.

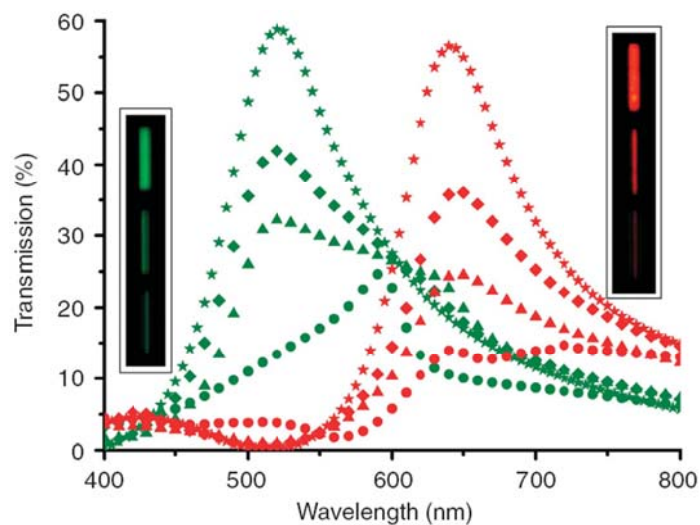


Figure 3.3 Plasmonic color filters with a few slits. Simulated transmission for the

green and red filters with 2, 4, 6 and infinite number of slits. The circle, triangle, diamond and star correspond to the structure with 2, 4, 6 and infinite slits respectively. Inset shows the optical microscopic images for the case of 2, 4 and 6 slits (namely, single, three, and five MIM stacked resonators, and slit number increases from bottom to top).

### 3.3 Plasmonic nanoresonators for spectral and polarimetric imaging

By gradually changing the periods of the plasmonic nanoresonator array, we also design and demonstrate a plasmonic spectroscope for spectral imaging. Figure 3.4(a) shows the fabricated device consisting of gradually changing period from 200 to 400 nm that covers all colors across the visible spectrum. When illuminated with white light, the structure becomes a rainbow stripe, with light emitting from the stack array, as shown in Figure 3.4(b). Plasmonic spectroscopes can disperse the whole visible spectrum in just a few micrometer distances, which are orders of magnitude smaller than the dispersion of the conventional prism-based device. This feature indicates that the color pixels formed by these structures could provide ultra-high spatial resolution for application in multiband spectral imaging systems. Our thin film stack structures can be directly integrated on top of focal plane arrays to implement high-resolution

spectral imaging, or to create chip-based ultra-compact spectrometers.

All structures discussed so far only consist of 1D linear slits (that is, a slit in the same direction). Here, we design a 2D micro-scale spoke structure that has slits in different orientations and a gradual change of slit spacing to further investigate spectral and polarimetric imaging responses. The spoke structure, as depicted in Figure 3.4(c), consists of 96 slits that form a circular ring. Each slit is 3  $\mu\text{m}$  in length and 50 nm in width, and the inner and outer radius of the ring is about 3 and 6  $\mu\text{m}$ . The spacing between neighboring slits changes from 200 nm from the center to 400 nm towards the outer edge of the ring, covering all colors across the visible range as the above linear spectroscopy. Figure 3.4(d) shows the polarimetric response of the spoke with different illuminations. When the spoke is illuminated with unpolarized white light, the transmitted light forms a complete rainbow ring. However, if the illumination is the polarized light and the polarization is rotated, a clear dark region appears along the polarization direction. This is because of the absence of excited SPs in the polarization direction, and thus the transmission is extremely low, which is consistent with the TM coupling discussed earlier. Therefore, this 2D spoke structure, when used with an imaging device, could provide real-time polarimetric information in spectral imaging, or it can be used as a microscale polarization analyzer.

### 3.4 Discussion and summary

Human eyes typically have a resolution limit of about  $80 \mu\text{m}$  at  $350 \text{ mm}$ . Therefore, we can use these plasmonic nanoresonators to build colored ‘ super-pixels ’ that are only several micrometers in a lateral dimension and are much smaller than the resolution limit of the human eyes. At present, this lateral dimension is also 1 – 2 orders of magnitude smaller than the best high-definition color filters currently available. Furthermore, these plasmonic devices have a longitudinal thickness that is 1 – 2 orders of magnitude thinner than that of colorant ones, which is very attractive for the design of ultrathin panel display devices.

Besides the slim dimensions, the nature of the polarization dependence of plasmonic resonators is also attractive. This feature not only benefits the applications in LCD by eliminating the need of a separate polarizer layer, but can also be used for extracting polarimetric information in spectral imaging.

In summary, we proposed and demonstrated plasmonic nanoresonators to disperse light with high efficiency spectrally. By arranging different resonators, arbitrary colored patterns on a micrometer scale are achievable. These artificial structures provide an opportunity for display and imaging devices with a higher spatial resolution, as well as

much smaller device dimensions than those currently available. The design principle can be easily expanded to other wavelength ranges for multispectral imaging.

# Chapter 4 Metallic resonant waveguide grating (MRWG) color filters

## 4.1 Motivation of color filters for LCD TV

The aforementioned works <sup>5, 87</sup> demonstrate that plasmonic color filtering is a promising technology to improve visual display devices. There is room to improve current color filters. Pigment color filters in LCD industry are costly. Out of tens of components, manufacturing cost of pigment color filters accounts for 20-30% of the total LCD TV cost. The large amount of cost on color filters is due to complicated manufacturing process. Figure 4.1 shows the process flow for color filters <sup>88</sup>, and the manufacturing process requires more than 20 process steps. Another issue of current pigment color filters is absorption loss. Currently only 6% light from back light unit (BLU) reach out of the visual display device, and part of the loss is due to color filters. Colorants pass the wavelength of interest but absorb energy out of this wavelength window. The absorption process reduces the amount of light that can be recycled.

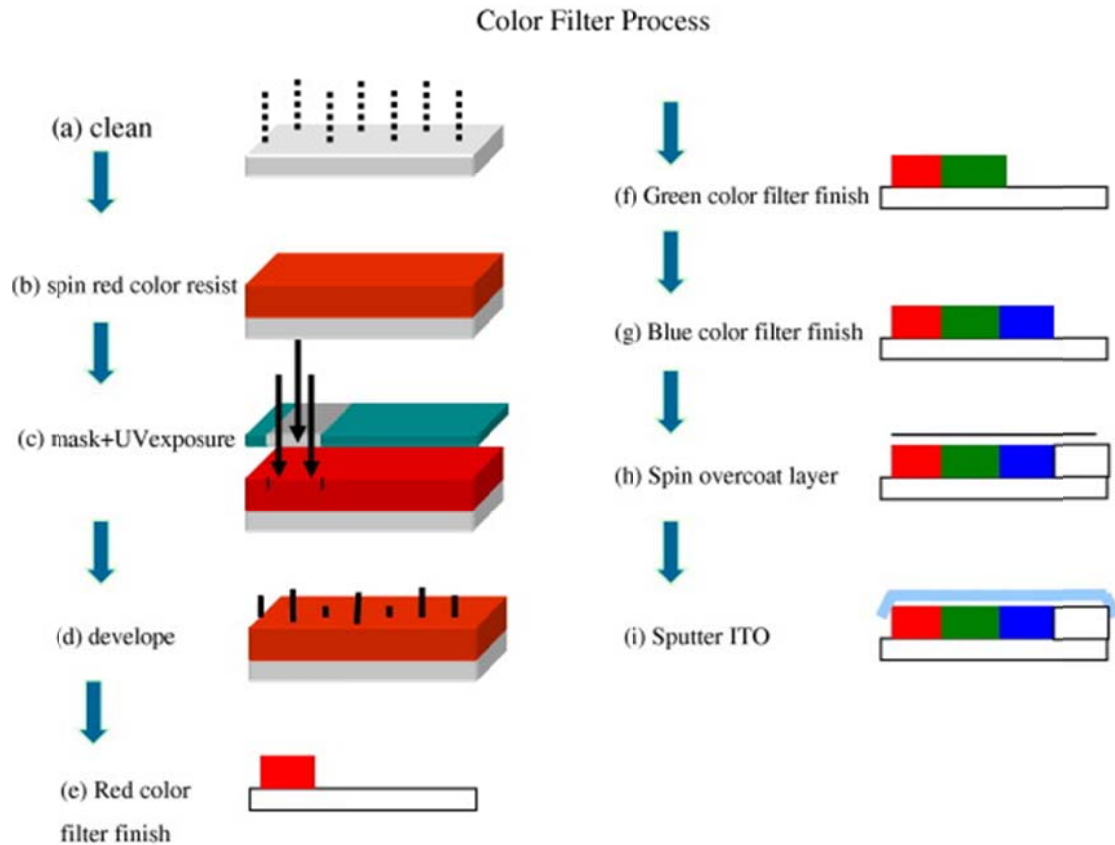


Figure 4.1 Manufacturing process flow for RGB Color filter<sup>88</sup>

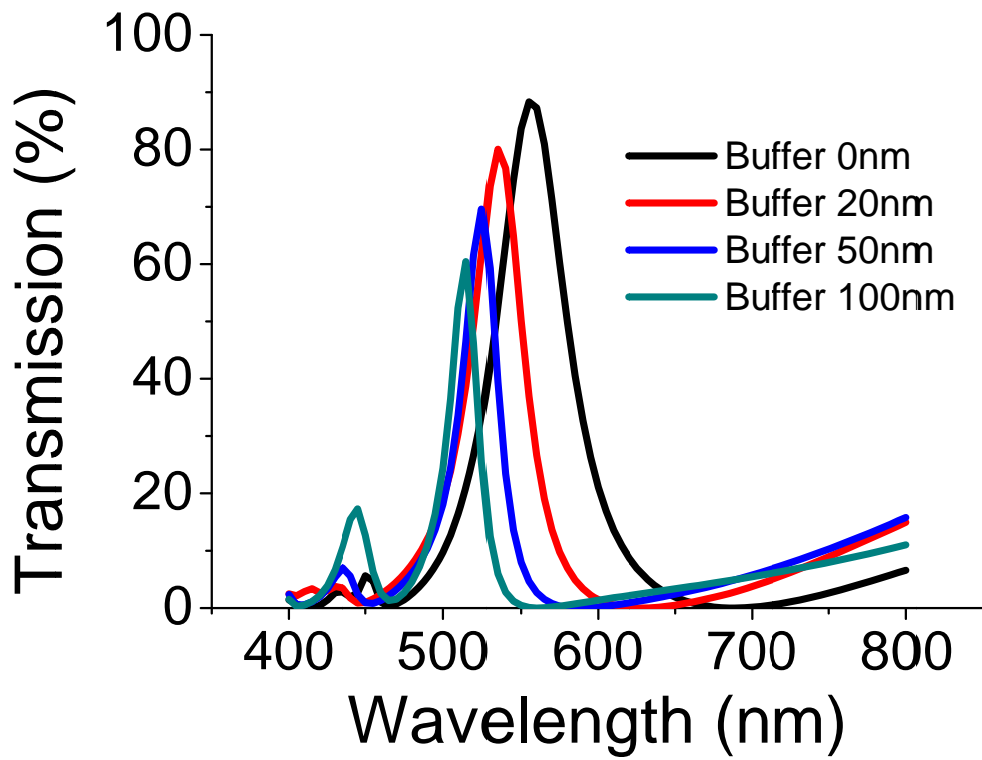
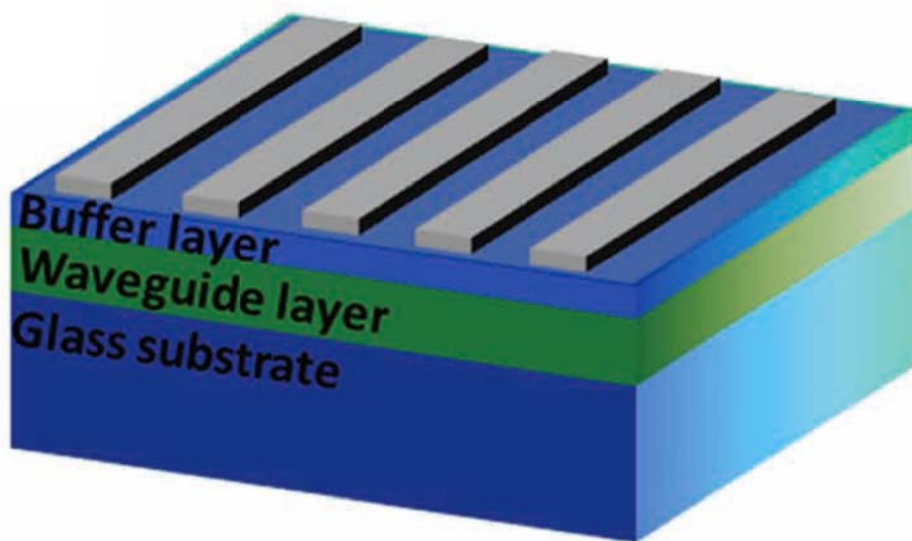
Plasmonic color filters are a promising approach to reduce the cost and loss in the LCD color filters. The work we have done<sup>5</sup> achieved narrower bandwidth than previous works, as well as much less absorbed light. More importantly, this design can be achieved by using simple fabrication process. To further improve plasmonic color filters toward higher transmission and color purity for commercial color filters, we propose and demonstrate another idea called metal resonance waveguide grating (MRWG). It will be described in detail in the following sections.

## 4.2 Design and results

The design shows in Figure 4.2(a). The metallic grating is placed on a stack of dielectric layers on glass substrate. The stack of thin film contains buffer layer and waveguide layer, the refractive index of which are 1.5 (silicon dioxide) and 2.0 (silicon nitride), respectively. The filtered color across the entire visible spectrum can be achieved by controlling the period of grating. Moreover, the linewidth of the transmission resonance can be adjusted from 10nm to 50nm by changing the thickness of buffer layer. This structure is originated from dielectric resonant waveguide grating (DRWG). DRWG is an optical element which consists of a dielectric grating and waveguide structure that allows light diffracted by the grating to couple into the waveguide modes<sup>89, 90</sup>. Because the dielectric medium is lossless and transparent, transmission spectrum of the DRWG is notch-type with extremely narrow resonance band, typically smaller than 1 nm. This characterization makes it very useful in the signal processing and biosensing applications. On the other hand, MRWG structure has the subwavelength grating made of metal rather than dielectric medium. Therefore, it can excite the surface plasmons and couple with the waveguide modes to realize color filtering. Not like DRWGs, the MRWG structure has a wider resonance bandwidth due to the metal loss, about several tens of nanometers. This MRWG still has narrower

resonance linewidth than other types of plasmonic color filters. Such bandwidth is suitable for the purity of the filtered color required for optical applications. Theoretically, the resonance linewidth can be tunable from 50 to 15nm, shown in Figure 4.2(b).

To realize this design, we fabricated these RGB color filters using the following process. The glass substrate is cleaned and then 40nm aluminum is deposited on the top. The PMMA A2 resist is spun and patterned using Raith 150 Ebeam lithography system to have grating patterns with period of 300, 350, 400nm and the gap size from 50nm. Afterwards, the aluminum is etched with patterned PMMA as a mask and appropriate mixed ratio of  $\text{BCl}_3$  and  $\text{Cl}_2$  etching gas. The final grating shows in Figure 4.2(c). We set up a measurement system based on the scheme of inverted microscope equipped with a Nikon D3000 DSLR camera and a spectrometer. The measured spectra and color response results for RGB design show in Figure 4.2(d) and (e). Moreover, the resonance bandwidth in MRWG filter can be tuned by changing the thickness of the buffer layer, which would further increase its practicality<sup>91</sup>.



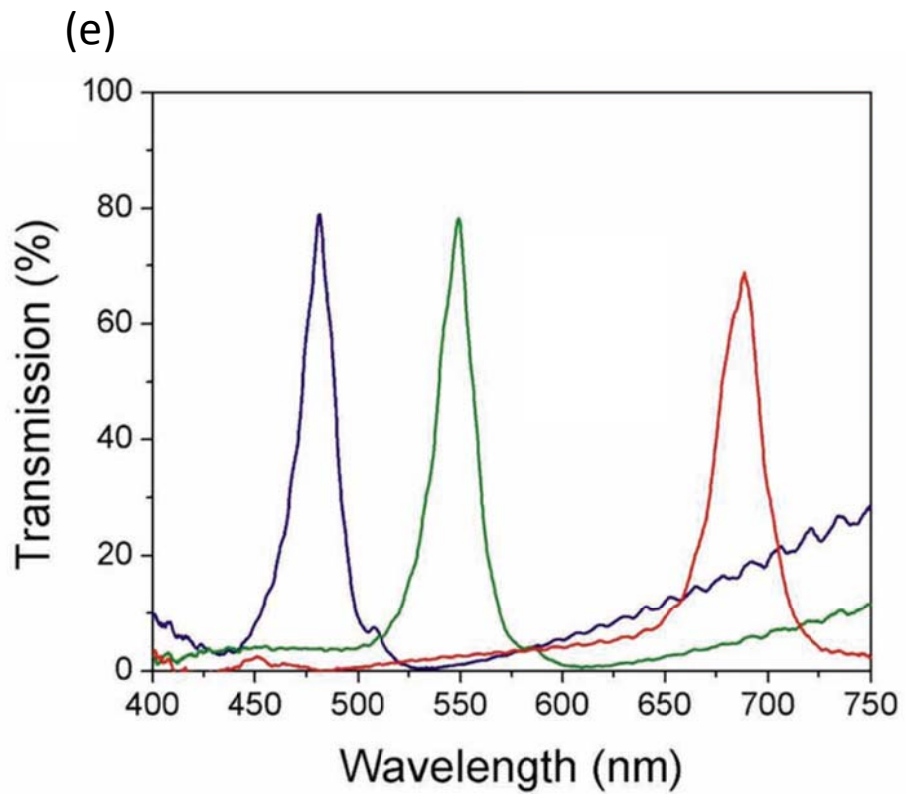
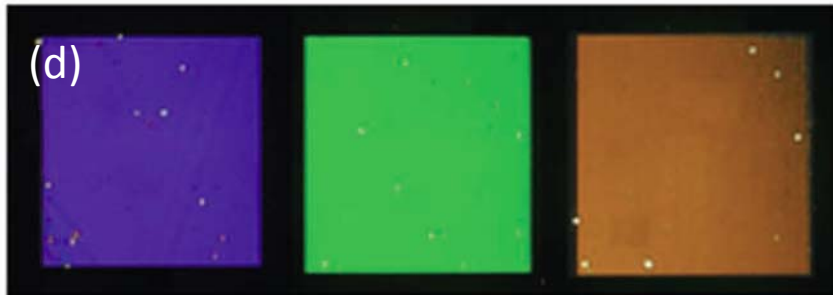
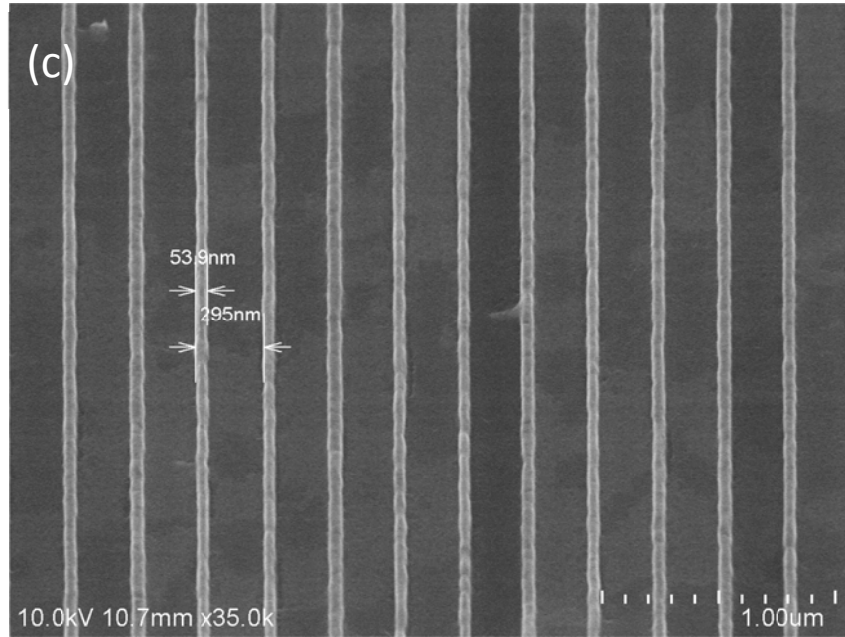


Figure 4.2 (a) Schematic of the metal resonant waveguide grating. (b) the simulated spectrum with the bandwidth between 15nm and 50nm by changing buffer layer thickness from 0 to 100nm. (c) SEM top view of the fabricated device with period of 300nm and gap of 54nm. (d) Normal incidence transmission images and (e) measured spectra for three square arrays of metal resonant waveguide gratings for blue, green, and red colors. The grating periods are 300, 350, and 450 nm, respectively, with 0.25 duty-cycles. The thicknesses of the silica buffer layer and silicon nitride waveguide layer are 50 and 100 nm, respectively

We showed in Figure 4.2(d) that the bandwidth of the resonance can be as small as 30nm. This design guarantees outstanding color purity. However, a potential problem is that we will have low total transmission and low color gamma by using this structure. This is an issue to prevent plasmonic color filters being commercialized. The reason is the trade-off between color purity and total transmission. In order to reduce the impact of total transmission, we have to design a set of RGB color filter that has good color purity, as well as reasonable total transmission. Collaborating with Samsung electronics, we designed this structure for potentially replacing the current pigment type color filters. The design is in the following Figure 4.3 (a). First, silver is chosen as plasmonic metal. The periods for blue, green, and red are 240, 320, and 420nm, where the gaps are 50, 80, and 110nm, respectively. The corresponding spectra for blue, green, and red are shown in Figure 4.3(b).

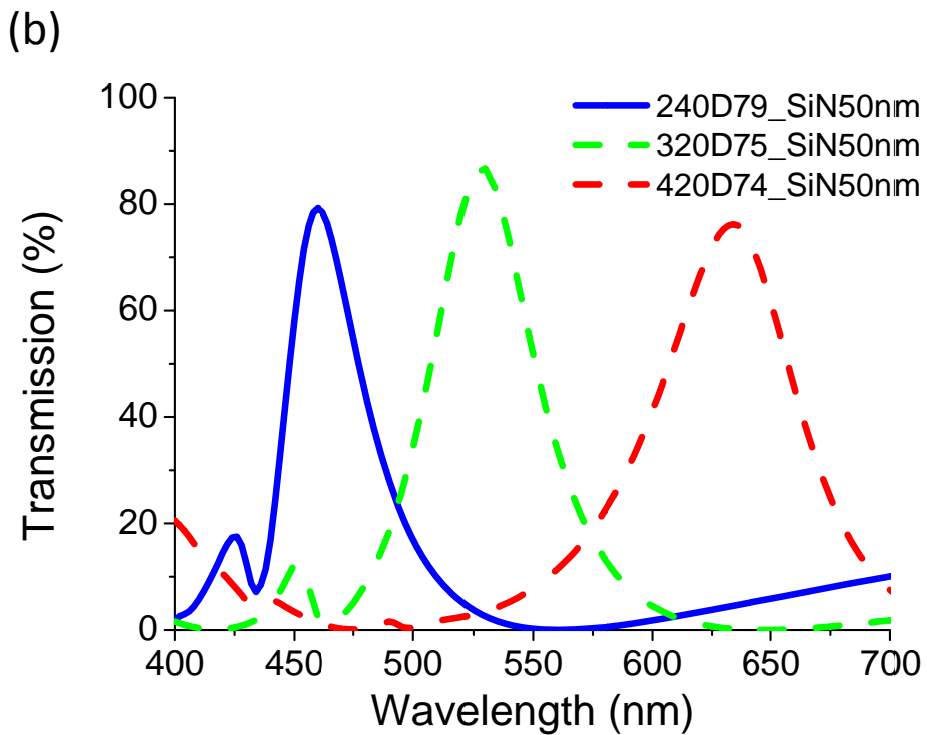
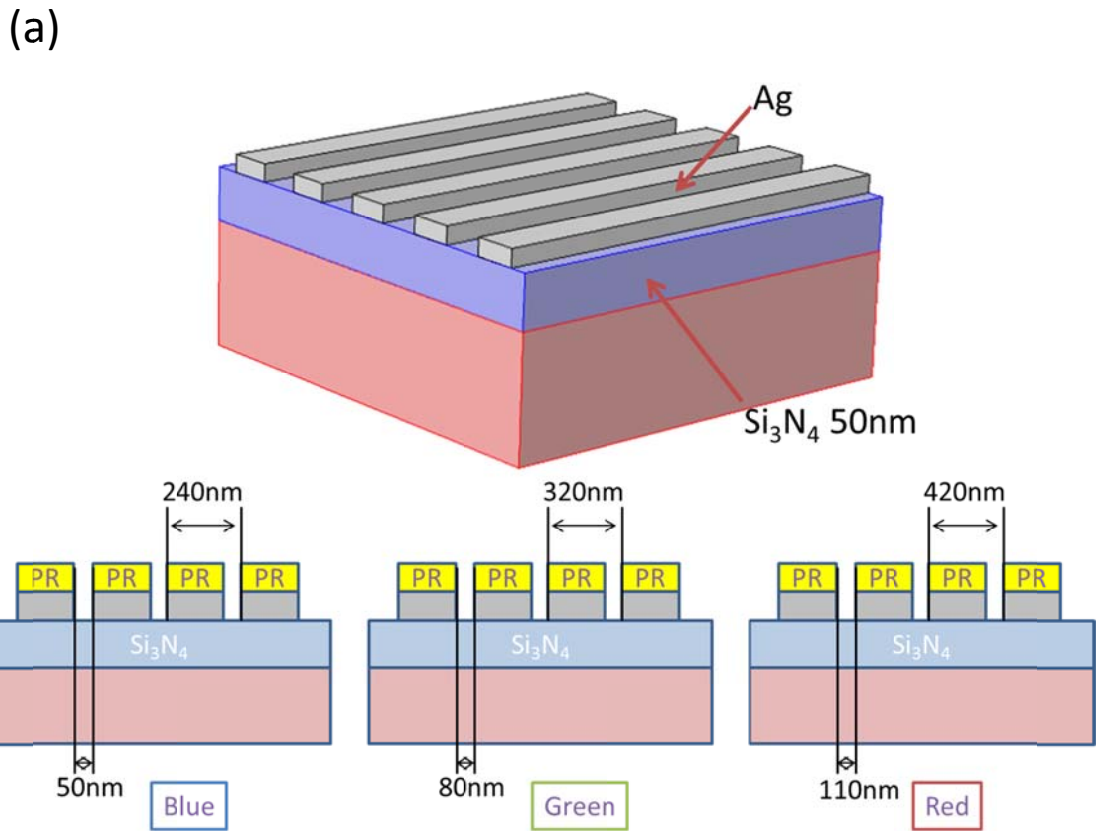


Figure 4.3 (a) Proposed designs for commercialized and manufacturable RGB color filters for visual display in Samsung Electronics and (b) the corresponding spectra (blue,

green, and red from left to right)

In order to achieve manufacturable optical color filters based on this design, we collaborated with visual display division, Samsung Electronics. The full process flow is described in Figure 4.4. First, the SU8 grating patterns are made on PMGI/SiNx/glass stack by Samsung, shown in Figure 4.5(a). Titanium is then shadow evaporated at either side of SU8 grating for SU8 mask protection. Afterwards, the unprotected PMGI resist is dry etched using O<sub>2</sub>, and the pattern before lift-off is shown in Figure 4.5(b). Finally, silver is deposited and lift off. Figure 4.6(a) shows the color response of the RGB color filters on a 4-inch glass wafer, and the detail will be discussed in the next section.

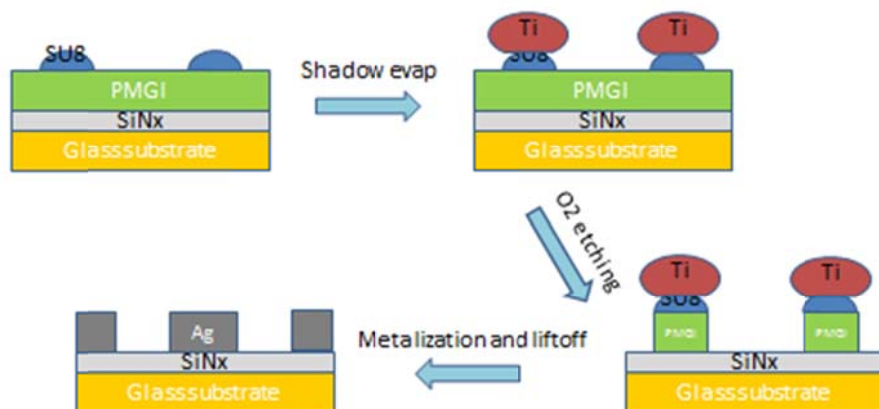


Figure 4.4 Process flow for manufacturable MRGW color filters

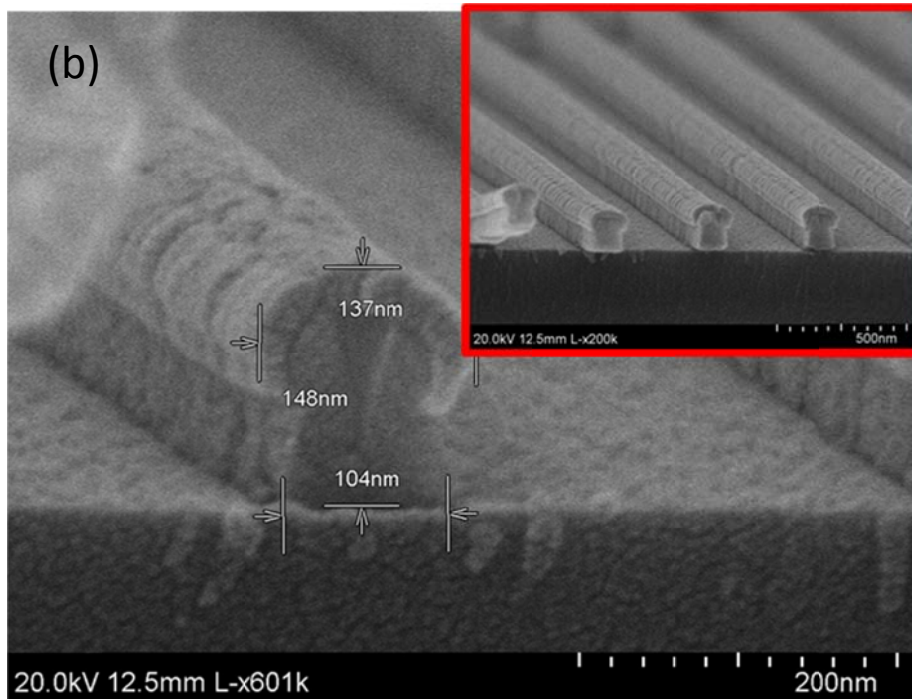
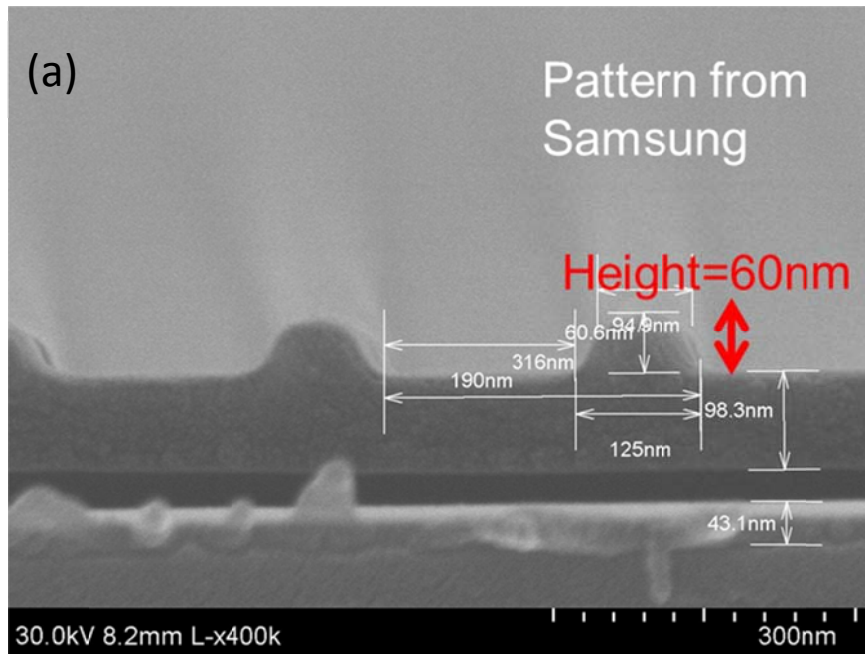


Figure 4.5 SEM of (a) cross-sectional SU8 resist pattern on top of PMGI/SiN<sub>x</sub>/glass stack from Samsung Electronics, and (b) cross section of the pattern for the red color filter after O<sub>2</sub> dry etching (inset: zoom-out cross section view)

## 4.3 Discussions

We demonstrated RGB colors on a 4-inch glass wafer in Figure 4.6(a). It shows possibility of simplifying manufacturing process and further reducing its cost.

However, this demonstration still has room to improve. Blue and green color filters shows good color purity, but the red color filter shows red color with blue color being mixed. The mixed color is proved to result from non-ideal trench linewidth control.

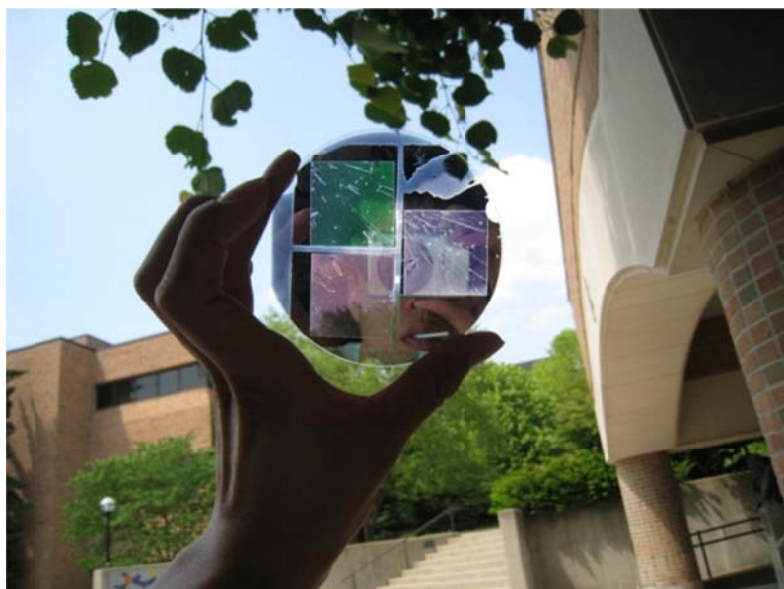
In Figure 4.5(b), SEM picture shows the trench width is defined as 137nm, around 30nm wider than my original design in Figure 4.3(a) (namely, 110nm). Furthermore,

simulated spectrum of the red color filter in Figure 4.6(d) contains a big blue peak when the trench is 30nm wider than design, whereas simulated spectra for blue and green

indicates relatively similar spectra in Figure 4.6(b) and (c). Therefore, this result explains the reason of not being pure red and indicates that trench linewidth is very

important for the real application.

(a)



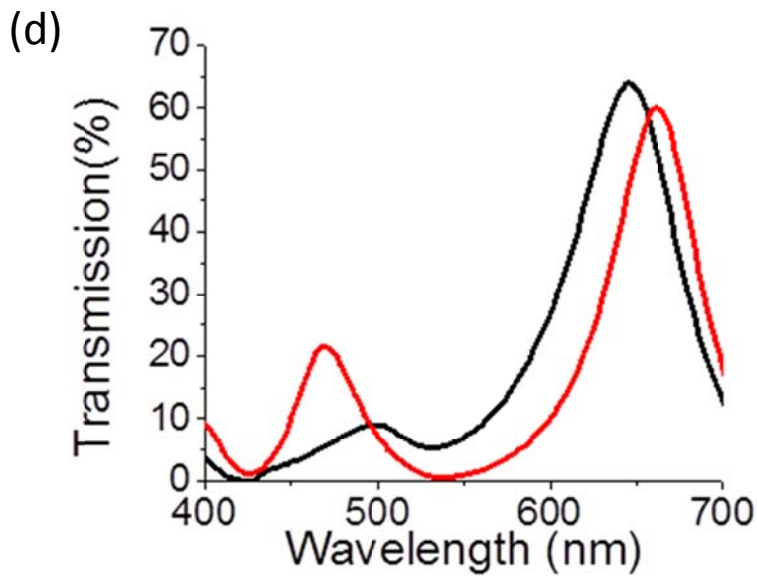
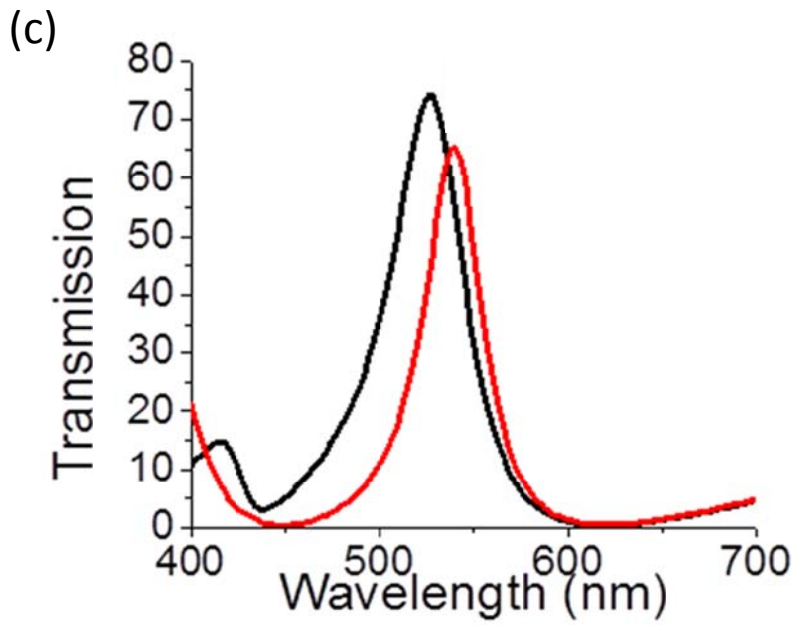
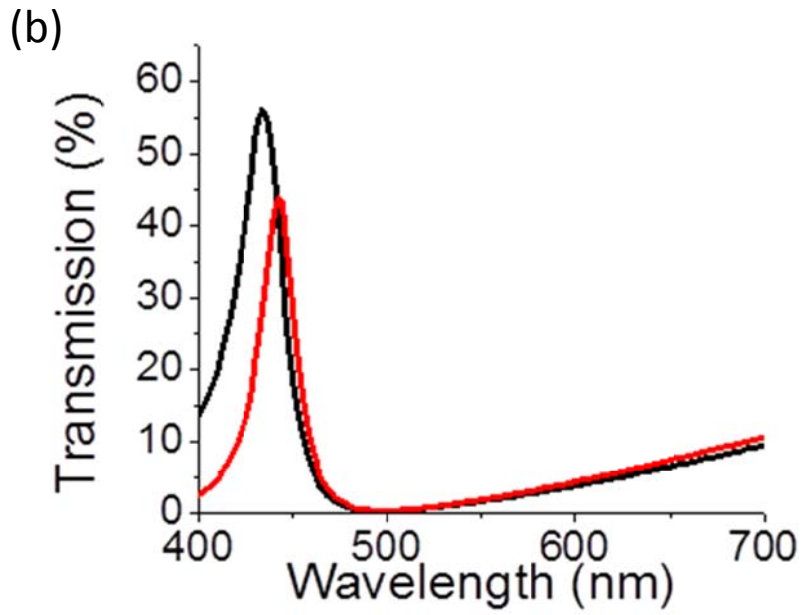


Figure 4.6 (a) Color and manufacturing demonstration of blue, green, and red MRWG color filters on a single 4 inch glass wafer. (b), (c), and (d) shows non-ideal trench linewidth after lift-off process leads to side resonance peak effect in the visible spectrum for blue, green, and red color filters, respectively.

However, this structure has a drawback of the angle sensitive color response. The main reason is the grating coupling mechanism. Grating coupling method is the bridge between free space light and bounded modes. To achieve this coupling, momentum along the propagating surface plane has to be conserved, which leads to the equation:

$k_{SP} = k_{grating} + k_{light}$ , where  $k_{sp}$ ,  $k_{light}$ , and  $k_{grating}$  are the momentum of plasmonic guided modes, momentum from Bloch theory, and incident light momentum along plasmonic mode propagation direction, respectively. To further make this equation

explicit, the previous equation becomes the following equation:  $k_{sp} = k_{inc} \sin \theta + \frac{2\pi}{\Lambda}$ ,

where  $k_{inc}$ ,  $\theta$ , and  $\Lambda$  indicates momentum of incident light, incident angle, and period of grating. It is clear that the momentum matching condition changes with incident angle, and therefore iridescence comes along with most plasmonic structures. This issue will be discussed in detail and addressed in the next chapter.

## 4.4 Summary

High resolution, slim dimension, and better power management are final goals for the development of visual display technologies. Typically, human eyes have a resolution limit of about  $80\ \mu\text{m}$  at  $350\ \text{mm}$ . By using plasmonic resonance, color filters can achieve subwavelength resolution for future high resolution applications. Moving toward commercialization, we need to focus on two aspects: first, the further improvement of their optical performances, i.e. transmission efficiency, color purity, and the incident angle-independency. Second is to develop a more efficient, high-throughput nanofabrication method to realize mass production with low costs. In this chapter, plasmonic based MRGW color filters are demonstrated to be manufacturable in large scale (2 inches), and this work paves the way for the commercial application of plasmonic color filters.

# Chapter 5 Study of wavelength tunable and angle-robust plasmonic spectrum filtering

## 5.1 Introduction and motivation

In the chapter 3 and 4, we have focused on color filtering effect based on plasmonic nanostructures. The structural colors are important for the liquid crystal display (LCD) industry. Structural color filtering is regarded as an attractive replacement for colorant pigmentation filtering. Such chemical pigments are vulnerable to a variety of processing chemicals, cannot withstand constant illumination with strong light intensities, and require extensive multilayer processing to pattern individual pixels<sup>5, 87, 92</sup>. Inspired by natural color filtering, as found in the wings of Morpho butterflies and the feathers of peacocks<sup>87, 93-96</sup>, many designs have been developed based on photonic crystals<sup>97, 98</sup> and plasmonic nano-structures<sup>5, 69, 70, 87, 99, 100</sup>. However, the iridescence of these devices leads to drastic changes in color with different incident angles of light, which is an important issue to be solved. For plasmonic nanostructures, this angle dependence is directly related to surface plasmon polariton (SPP) excitation via grating coupling<sup>5, 82, 87, 99, 101</sup>. This has led to high coupling efficiencies<sup>102</sup>, but is inherently angle-dependent due to momentum matching

conditions. Overcoming this angle-dependent spectrum response will allow these structural filters to be integrated into practical applications such as high resolution visual displays, miniature hyperspectral imaging, and high sensitivity sensors<sup>103-105</sup>.

To obtain angle-insensitivity, one has to avoid relying on grating coupling for plasmonic mode excitation. In contrast to grating coupling, plasmonic based resonators and antennas have been demonstrated as candidates for structure colors<sup>106-110</sup>. Additionally, horizontally deployed plasmonic antennas and resonators have gained attention on angle insensitive spectrum filtering response in Near-IR, Mid-IR, and THz band<sup>18, 39, 111</sup>. However, as pointed out by Kumar et. al.<sup>96</sup>, increasing the density of these plasmonic resonators is necessary to effectively scatter light to viewers' eyes (or detector) at visible wavelengths. In order to increase the scattering efficiency and generate more vivid colors, a vertical plasmonic resonator array has been realized with specially designed periodicity.

In this design, light funneling into periodic nanoslits is exploited to generate strong absorption for transverse magnetic (TM) polarized incident fields<sup>112-114</sup>. Utilizing light funneling, extremely small physical dimensions have large scattering cross sections, and therefore possess plasmonic mode coupling with efficiency comparable

to that of grating coupling. In this letter, we theoretically and experimentally study angle robust optical devices with near-perfect absorption, as large as 96%, in the visible spectrum. Moreover, wide color tunability throughout the entire visible spectrum and pixel size beyond the diffraction limit are demonstrated. We also suggest a design principle for angle-robust reflection by investigating the angular response of the reflection spectra with respect to the periodicity of arrayed one-dimensional structures. We further discuss the influence of periodicity on field confinement within the nano-cavities, and conclude through discussion of a variety of applications for angle robust field confinement and spectrum filtering.

## 5.2 Methods

Simulations and experiments in this letter, broad band and collimated light illumination in the wavelength range  $\lambda=400\text{-}800\text{nm}$  is supplied as the input signal, and the reflected signal is collected at an angle corresponding to the 0<sup>th</sup> order reflection. The simulation is performed using finite difference time domain (FDTD) method for the field distribution details and rigorous coupled wave analysis (RCWA) is used to calculate the angle resolved reflection and absorption spectra. It is also noticed that the angle we are investigating is defined in Appendix 2.

The device is fabricated through use of nanoimprint lithography (NIL), reactive ion etching (RIE), and metal deposition. To fabricate these devices a template is first created in a fused silica substrate through reactive ion etching (RIE) and then Ag is sputter deposited at onto the silica grating conformally covering the etched silica walls. The fused silica substrate was chosen due to its desirable refractive index in the visible spectrum and Ag was chosen because of its desirable plasmonic characteristics in the visible regime.

The optical measurement is conducted using two systems to obtain the reflection/absorption spectra at normal and angled incidences. Reflection spectra at normal incidence are measured using Nikon TE300 inverted microscope with a halogen lamp for the light source. Reflection spectra with angled incidence are measured from  $45^\circ$  to  $75^\circ$  ( $2^\circ$  increment) with a J. A. Woollam M-2000 ellipsometer. The numerical apertures of the collection optics in both systems are as low as 0.04 to ensure high angular resolution.

## 5.3 Design and theory

A schematic diagram of our plasmonic nanostructure is illustrated in Figure 5.1(a) as well as a corresponding SEM image of a fabricated device. Silver (Ag) is conformally deposited on a fused silica grating defined with the pitch, depth, and width of the grating as  $P$ ,  $D$ , and  $W$  respectively. As opposed to trapping the incident light into surface plasmon modes through grating coupling, the dimensions and periodicity of the structure have been designed to concentrate the light into the silica nano-grooves based on a phenomena recognized as light funneling. As light is incident on the nano-groove array, an induced polarization charge pair accumulates at the top corners of the grooves. This charge pair acts as a dipole and further alters the E-field of incident light, redirecting the light into the groove. Figure 5.1(b) shows this effect with a red-blue surface plot and arrow plot which represent the normalized polarization charge distribution induced by the scattered field<sup>21</sup> and propagation direction of the field's Poynting vector, respectively. It is noticed that the purple arrows near the Ag and silica interface point toward the groove verifying this funneling effect. The intensity distribution of the magnetic field  $|H_y|^2$ , under the funneling condition, is depicted in Figure 5.1(c) showing that the light is well confined in the groove at the resonant wavelength.

The above angle insensitive color filtering results from the fact that light is funneled

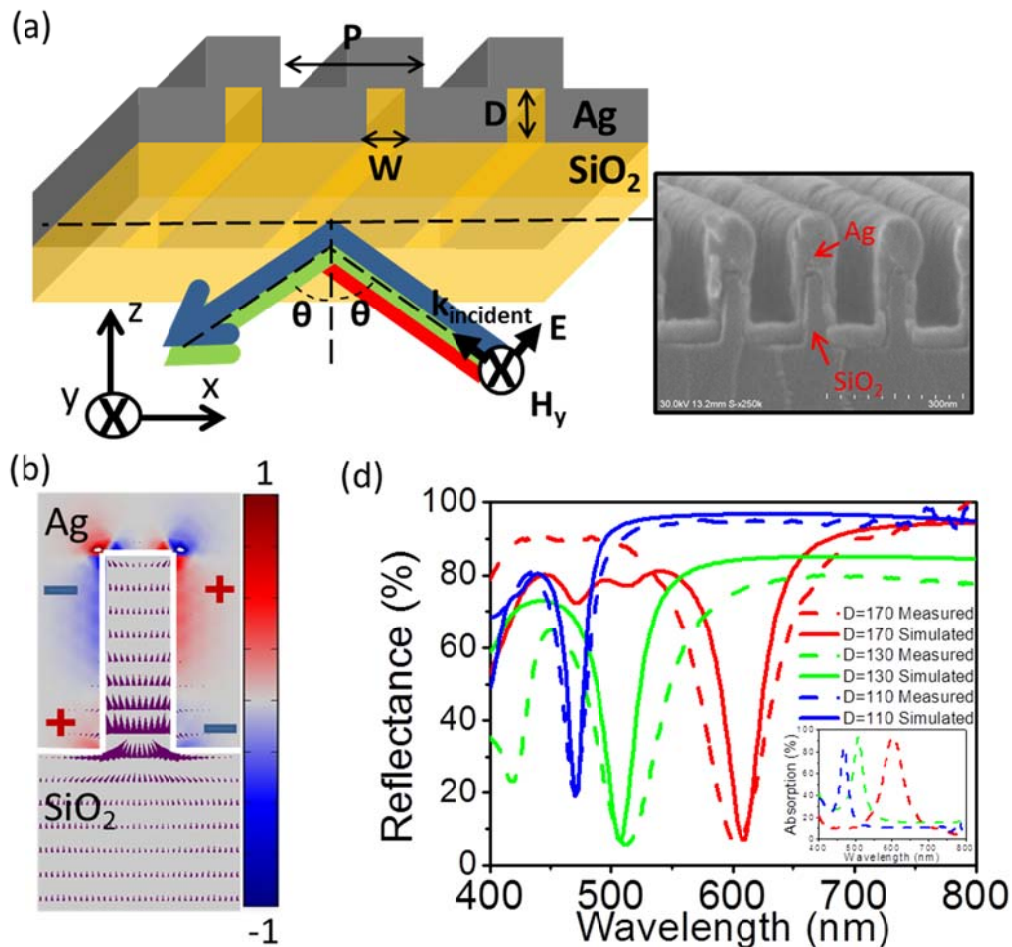
into metal-insulator-metal Fabry-Perot (MIMFP) cavity modes. By varying the optical path length in the MIMFP cavity through changing the width and depth of the nano-grooves, the resonance of the structure is able to be tuned across the entire visible spectrum. The MIMFP resonant wavelength,  $\lambda$ , is determined by the effective refractive index,  $n_{eff}$ , and the depth,  $D$ , in the Fabry Perot resonance equation,  $(\frac{1}{4} + \frac{1}{2}m)\lambda = n_{eff}D$ , where  $m$  is a positive integer and  $n_{eff}$  is the effective refractive index of MIM waveguide modes. The effective index is insignificantly dependent on the nano-groove thickness,  $D$ <sup>24</sup>, but is highly dependent on acute changes in the width,  $W$ . The effective indices,  $n_{eff}$ , are calculated for changing values in width,  $W$ <sup>112, 115</sup>. For example, when  $W=50\text{nm}$ , the effective index dispersion relation of even modes in a MIM waveguide at insulator  $\text{SiO}_2$  thickness is found to be  $n_{eff}=1.85$ , 1.90, and 2.02 for wavelengths of  $\lambda=620$ , 532, and 460nm, respectively. When  $W=60\text{nm}$ ,  $n_{eff}=1.91$ , 1.99, and 2.11, respectively. This design can be integrated into various applications as well as accommodate different manufacturing processes, since there is a wide degree of freedom in modifying the filtered color by changing either  $D$  or  $W$ . This dependence on optical path length, as opposed to grating coupling into waveguide or plasmonic modes, allows angle insensitive performance.

## 5.4 Ultra-high resolution and widely tunable color filtering

The next topic is ultra-high resolution, widely tunable color filtering. First, a description is given on how resonant wavelength, namely the wavelength of the absorption peaks (reflections dips), can be tuned throughout the entire visible spectrum through adjusting the groove depth  $D$ . In this set of simulation and experiment, the groove width,  $W$ , and period,  $P$ , are held constant at 50nm and 180nm respectively. The groove depths  $D$  corresponding to yellow, cyan, and magenta reflective colors are found to be 110, 130, and 170nm, respectively. Figure 5.1(d) presents the simulated and measured reflection spectra (and measured absorption spectra in the inset) of the above three devices with different  $D$  at normal incidence and TM polarized light. These devices are able to trap light as much as 96% at the resonance wavelength and reflect all other wavelengths. The optical propagation loss in silver at shorter wavelengths is non-negligible, resulting in an 80% absorption peak at the shorter wavelength. This strong absorption at the selected wavelength range can be exploited for high purity reflective color filtering.

In addition to the color tuning based on changing  $D$ , Figure 5.1(e) shows that the three basic colors of the cyan, magenta, and yellow (CMY) color scheme can also be

achieved by adjusting the width of the nano-groove  $W$  from 40nm to 90nm, given fixed  $P=180$ nm and  $D=170$ nm. It is noticed that the broad resonance dip on the yellow device is due to larger propagation loss of the MIM waveguides at higher frequencies. A better reflection dip for yellow can be achieved by changing  $D$  to 110nm with  $W=50$ nm as shown in the blue solid and dotted lines in Figure 5.1(d). This method of holding the period and depth constant while varying the widths of the groove presents a more viable method for manufacturing where the depth of reactive ion etching (RIE) is held constant and the width of each colored pixel is altered, allowing multiple color pixels to be produced on a single wafer.



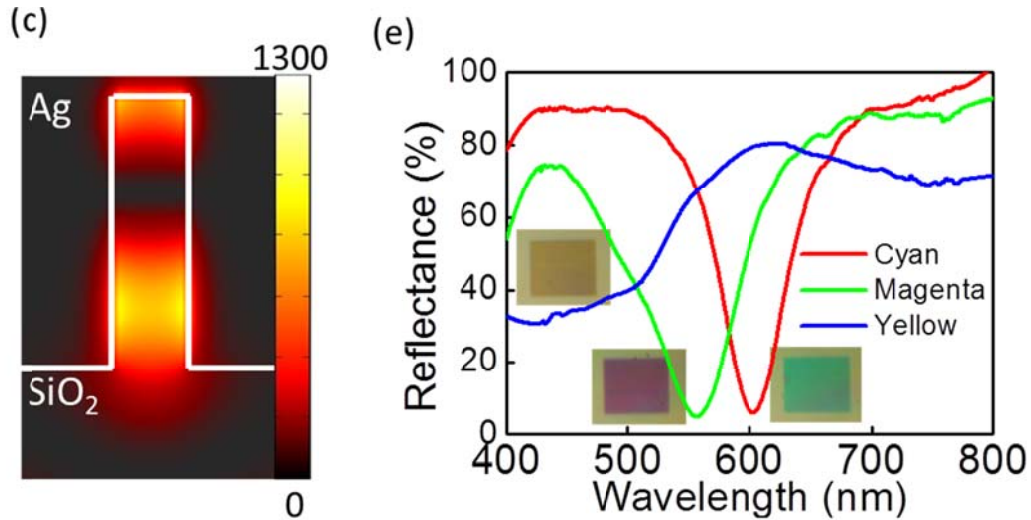


Figure 5.1 Plasmonic-nanocavity-based angle robust color filtering. (a) A schematic of the proposed structure and corresponding SEM image of a fabricated device with width ( $W$ )=45nm, depth ( $D$ )=160nm, and period ( $P$ )=180nm with  $\Theta$  as the incident angle of light. (b) Polarization charge and Poynting vector distribution of light funneled into these nano-grooves, presented with the red–blue surface plot and purple arrows, respectively. (c) Intensity distribution of the magnetic-field  $H_y$  at resonance,  $P=180$ ,  $W=50$ , and  $D=170$ nm. (d) Reflection (simulated in solid lines and measured in dash lines) and measured absorption spectra (inset, dashed lines) at  $D=110$ , 130, and 170nm in blue, green, and red curves, given fixed  $P=180$  and  $W=50$ nm at normal incidence. (e) Reflection spectra at fixed  $P=180$ nm and  $D=170$ nm demonstrating the three basic colors of the CMY color model, cyan (C), magenta (M), and yellow (Y), with varying  $W=40$ , 60, and 90nm at normal incidence

In order to demonstrate the visual performance of these color filters, we have designed and fabricated colored images in the format of the Olympic Rings. Figure 5.2(a) and its insets show SEM images of the devices. The corresponding optical

image of these reflective color filters is in Figure 5.2(b). The period,  $P$ , and depth,  $D$ , of each ring are held constant while the widths,  $W$ , vary from 40nm to 90nm to generate the different colors. The angular dependence of these images was unable to be measured because of the small size of the images. The next section presents large scale devices fabricated through nanoimprint lithography in which we were able to measure the angled reflection spectrum and confirm angle insensitivity. With this technique, cyan, magenta, and yellow, as well as intermediate colors can be achieved. Note that the purple color from the rope held by the gymnast in the top middle ring is produced by two nano-grooves. Moreover, the magenta color from the bow area is produced by several isolated and segmented short lines, as small as 100nm in length and 60nm in width, demonstrating ultra-high color resolution. In the supporting information, we include simulation results to prove that even single and double slits have color filtering effect (Appendix 3). This color demonstration proves that the proposed plasmonic structural color is capable of creating pixels with sizes beyond the diffraction limit of light. This opens up the possibility of realizing super-pixels imaging<sup>5</sup>, in which colors are mixed between multiple super-pixels before their combined size is comparable to the diffraction limit. In addition, a ring with two colors has been fabricated in order to present an application of the polarization dependence of these filters. Figure 5.2(c) shows an image with two sets of gratings.

As the polarization of incident light is changed, the displayed image is altered. Particularly, the central pattern in Figure 5.2(c) is concealed when the incident light polarization changes from TM polarized light to TE. This polarization dependence can be utilized in applications of cryptography and anti-counterfeiting. One specific example would be to put such images on a personal identification card. Counterfeiters may be able to reproduce the color of the symbol but it would be increasingly difficult for them to make the image additionally dependent on polarization of light, adding another element to the validity of the identification card. This polarization dependence is also advantageous for implementation in visual display technologies by creating a multifunctional component that can serve as a conductive electrode, polarizer, and color filter simultaneously.

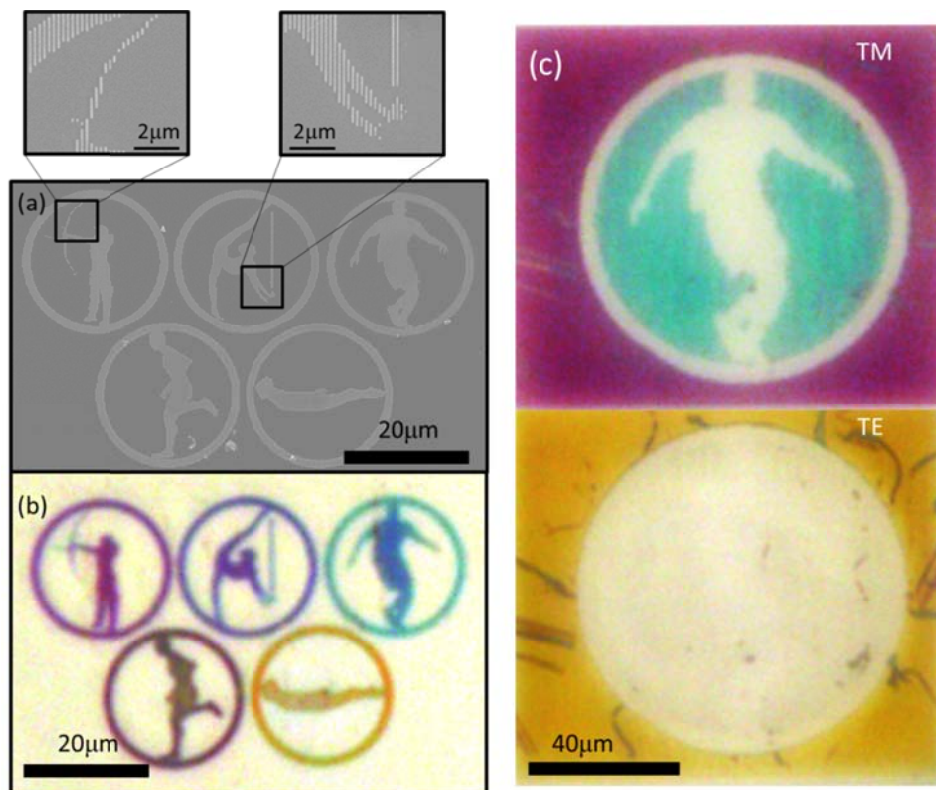


Figure 5.2 Color demonstrations with ultra-high resolution and polarization dependent images. (a) The SEM images and (b) optical image under white light illumination of fabricated colored images in the format of the Olympic rings. The full range of CMY colors are achieved by sweeping  $W$  from 40 to 90nm, with  $P$  and  $D$  fixed at 180nm and 170nm respectively. (b) Shows that even a single short segmented nano-groove demonstrates color response. (c) Demonstrates utilizing polarization dependence to actively change the displayed image, where grooves with  $W=40$  for cyan and  $W=60$ nm for magenta under TM illumination.

## 5.5 Design rules for angle insensitivity

The effect of periodicity on the angle robustness of these metallic nano-grooves is investigated here. Given  $W=50$ nm and  $D=180$ nm, the simulated angle resolved reflection spectra contour plots at periods of  $P=140$ , 180, 220, and 260nm are shown in Figure 5.3(a), (b), (c), and (d). Incremental changes of 40nm in the period are chosen to illustrate three different regimes: grating coupling, localized resonance, as well as cavity coupling between neighboring waveguides which is explained further in the next section of this letter. Figure 5.3(a) and (d) indicate higher angle dependence than Figures 5.3(b) and (c). When the period  $P=140$ nm and 260nm, the MIMFP resonance position shifts with increasing incident angle of light, whereas the spectra at the other two periods, 180 and 220nm, remain at a relatively constant wavelengths

over all incident angles. Furthermore, the angular behavior of absorption at the resonance wavelength 630nm with  $P= 140, 180, 220$  and  $260\text{nm}$  are presented in Figure 5.3(e) showing that the absorption reaches over 90% for  $\pm 90^\circ$  angle range with  $P=180\text{nm}$ . This shows that angle independence is achieved at a periodicity of  $180\text{nm}$  for visible wavelengths of light. Above or below  $P=180\text{nm}$ , the resonance wavelength corresponding to the absorption peak is angle dependent and therefore less efficient. The angle resolved reflection spectra from angles of  $45^\circ$  to  $75^\circ$  were measured on various large scale fabricated devices based on nanoimprint lithography. Two of them are shown in Figures 5.4(a) and (b) with a period of  $180\text{nm}$  and depths  $D$ , of  $130$  and  $170\text{nm}$ , respectively. A device fabricated with a period of  $220\text{nm}$  exhibited angle dependence further validating this design. The angle resolved reflection spectra of this device, with  $P=220\text{nm}$ ,  $W=45\text{nm}$ , and  $D=160\text{nm}$ , is displayed in Figure 5.4(c).  $25\text{nm } \Delta\lambda$  is observed per  $30^\circ$  change in incident illumination angle. This change in reflection dip is not observed at  $P=180\text{nm}$  (Figures 5.4(a) and (b)) showing strong agreement between measured and simulated spectra. Through this analysis we conclude that a range of periods from  $160\text{nm}$  to  $200\text{nm}$  has been found to possess angle robust spectrum response.

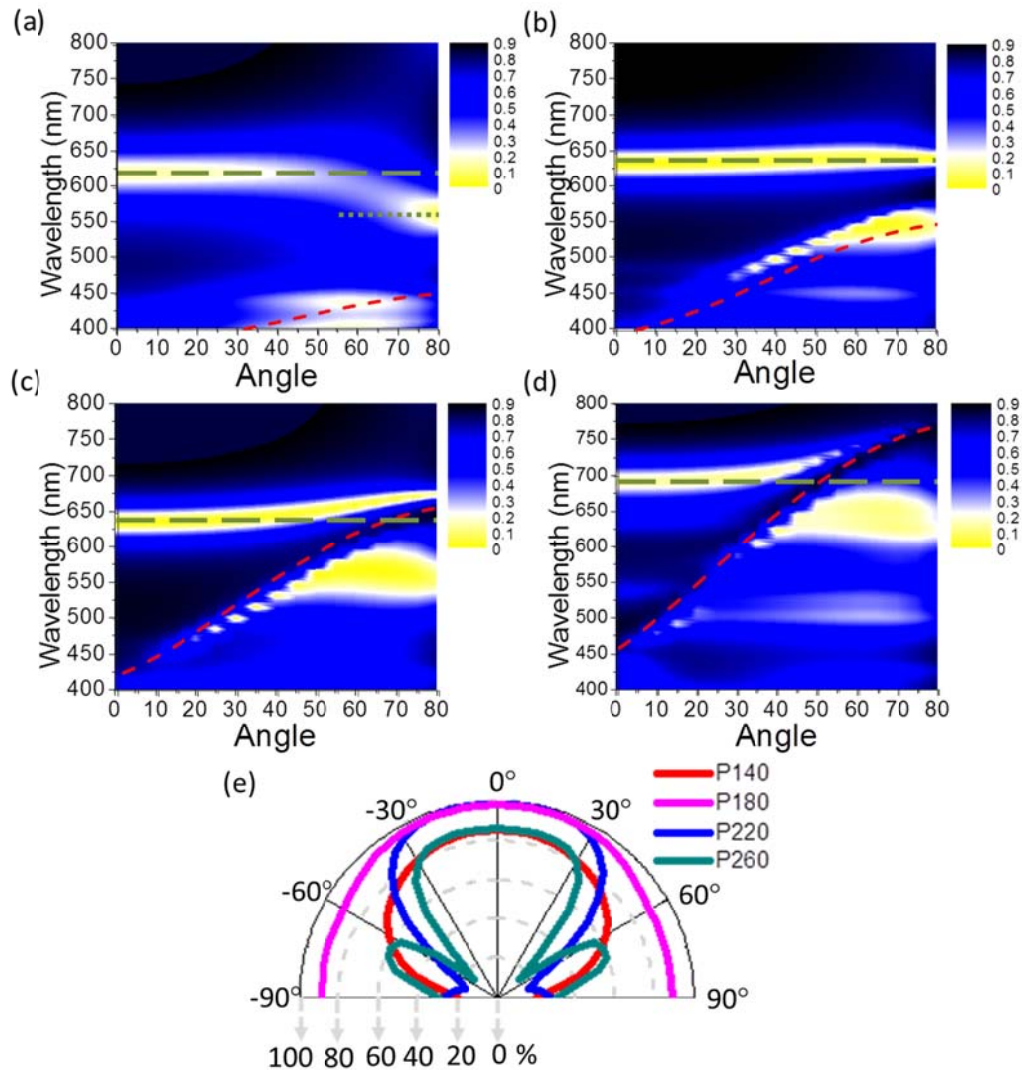
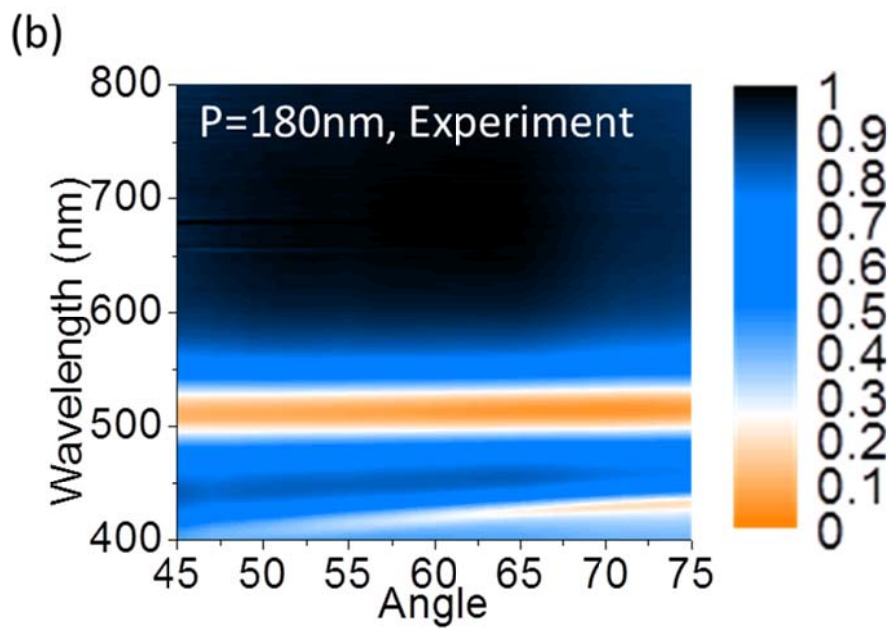
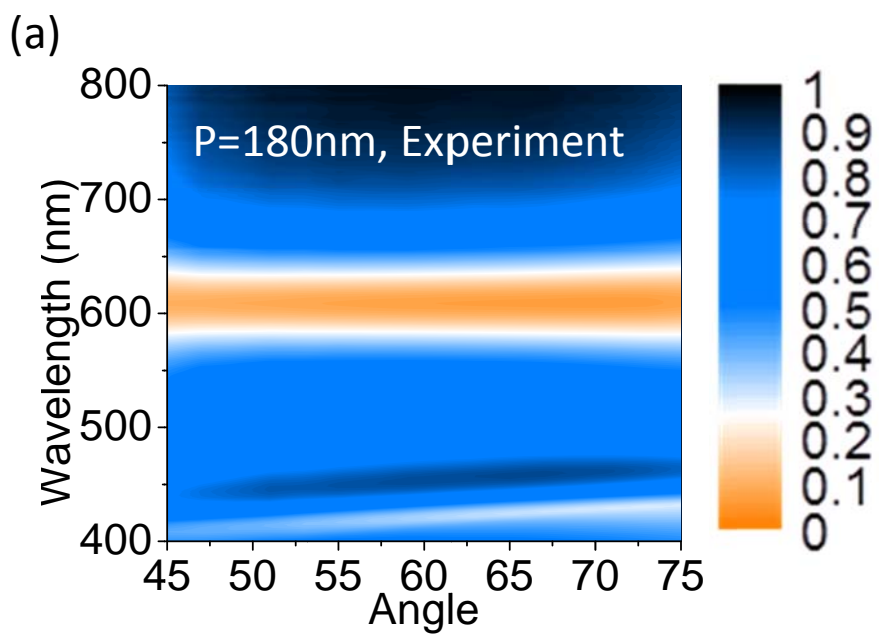


Figure 5.3 Simulated angle resolved reflection spectra with various periods. The simulated angle resolved reflection spectra contour plots at periods  $P=140$  (a) ,  $P=180$  (b),  $P=220$  (c), and  $P=260\text{nm}$  (d). The green dash lines in all four figures indicate metal-insulator-metal Fabry-Perot (MIMFP) cavity mode, whereas the red dash lines refer to the grating assisted surface plasmon (GASP) modes whose dispersion is dependent on the grating period. The crossing between MIMFP and GASP when  $P=220$  and  $260\text{nm}$  indicates coupling between the two modes. The green dash line in (a) refers to the dispersion of odd mode defined in Figure 5(c). (e) The simulated angular absorption maxima in terms of various period from 140, 180, 220, and 260nm.



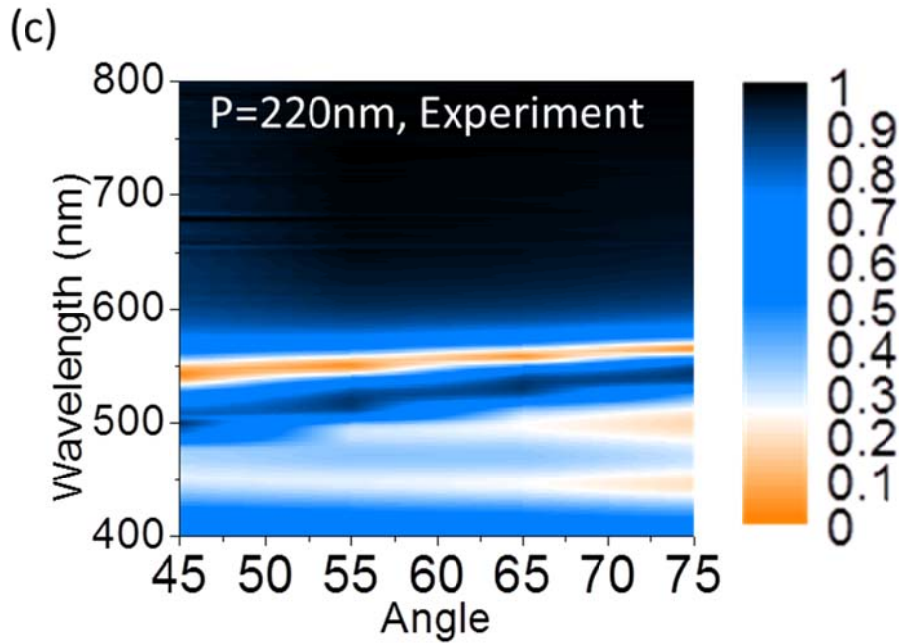


Figure 5.4 Experimental angle insensitive spectrum filtering. (a) The simulated angular absorption maxima in terms of various periods from 140, 180, 220, and 260nm. The angle resolved reflection spectra of this design with sweeping incident illumination angle from  $45^\circ$  to  $75^\circ$  are presented with the following device dimensions (b)  $P=180$ ,  $W=50$ , and  $D=130$ nm, (c)  $P=180$ ,  $W=50$ , and  $D=170$ nm, and (d)  $P=220$ nm,  $W=50$ nm, and  $D=160$ nm. (b) and (c) show flat band absorption response indicating angle insensitivity, while (d) shows 25nm resonance wavelength shift per  $30^\circ$  change in incident illumination angle representing coupling between MIMFP and GASP modes

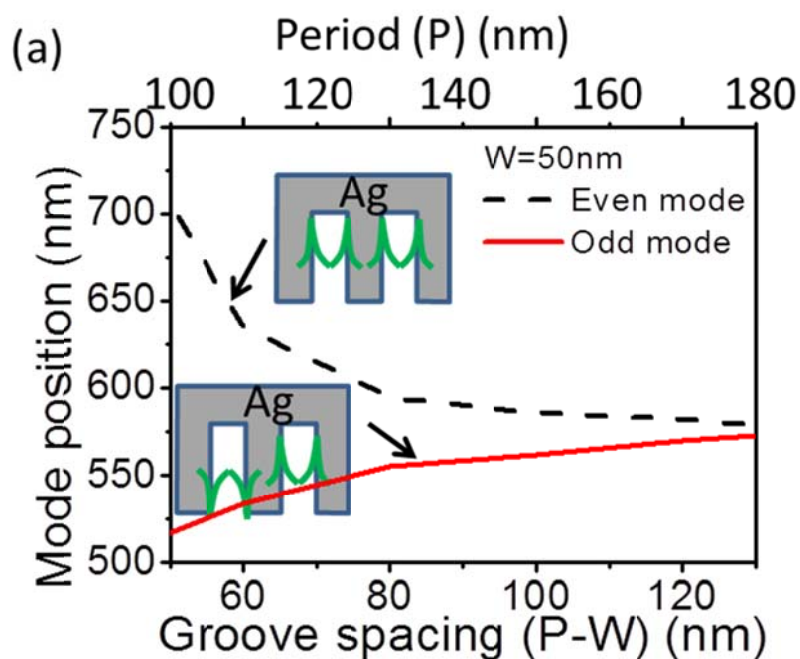
We would now like to further elaborate on the mechanism for angle dependence when the period is away from the optimal range,  $P > 200$ nm and  $P < 160$ nm. Clearly shown in Figures 5.3(e), the side lobes of the absorption maxima develop at large angles of incidence. Therefore we further analyzed the resonant modes at these larger degrees

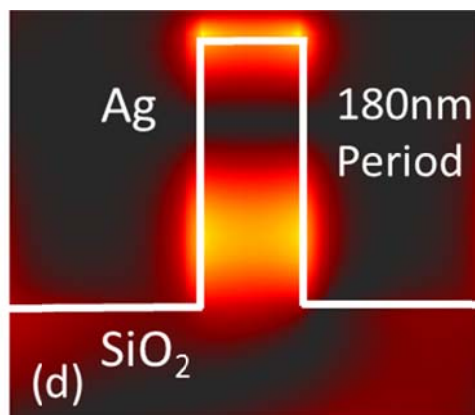
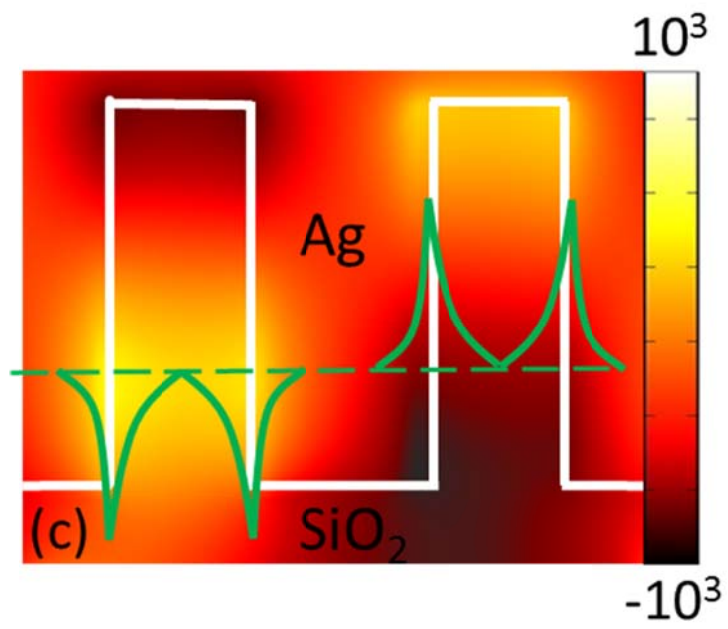
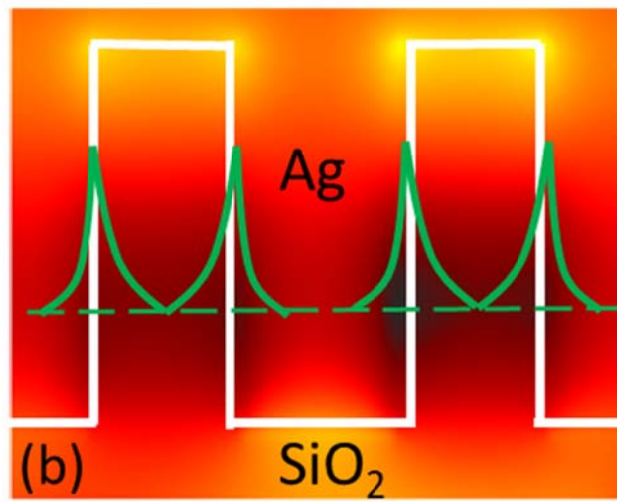
of incidence. For  $P > 200$ , two modes are involved in this phenomenon. MIMFP resonances are angle independent modes, illustrated as green straight dash lines, and grating assisted surface plasmon modes (GASP) generated under the Bragg coupling condition<sup>101</sup> are highly angle dependent, illustrated by the red dashed lines in Figures 5.3(a), (b), (c) and (d). The increasing angle leads to the interaction between the MIMFP modes and the grating assisted surface plasmon modes (GASP) due to momentum matching. For TM-polarized waves, the momentum matching equation for grating assisted surface plasmon resonance excitation of dielectric—metal interfaces is governed by the following relationship,  $\frac{m}{\Lambda} + \frac{1}{\lambda} \sin \theta = \frac{1}{\lambda} \sqrt{\frac{\epsilon_1}{\epsilon_1 + \epsilon_2}}$ . In this equation,  $m$  represents the diffraction order,  $\Lambda$  the period (denoted in the figures as  $P$ ),  $\lambda$  the wavelength,  $\theta$  the incident angle, and  $\epsilon_1$  and  $\epsilon_2$  are the permittivity of the metal and dielectric materials respectively. The red curves in Figures 5.3(a), (b), (c), and (d) extend from the ultraviolet to the visible region with increasing periodicity, and finally result in a strong coupling between the GASP and the MIMFP cavity modes. The field distribution of this coupling will be discussed in the end of this letter. Moreover,  $\Lambda$  is found to be proportional to  $\lambda$  in the above equation, which provides a guideline of selecting the appropriate period for angle independent plasmonic resonance at desired wavelength bands.

When  $P < 160\text{nm}$ , the MIMFP resonance band blue shifts at incident angles greater than  $60^\circ$ . This is due to the breakdown of the assumption that nano-groove structures are well separated (nano-groove size  $W \ll \text{Period } P$ ). When the thickness of the groove spacing ( $P-W = \text{groove spacing}$ ) is too small, the dispersion has to be reconsidered due to coupling between neighboring metal-insulator-metal (MIM) waveguides<sup>116, 117</sup>. Figure 5.5(a) shows the mode dispersion with respect to the groove spacing ( $P-W$ ) and Period. In this scheme, even and odd modes are defined in Figure 5.5(a), which indicate whether the field is in-phase or out-of-phase in the neighboring grooves, respectively. The fields of both even and odd modes at an incident angle of  $75^\circ$  are plotted in Figures 5.5(b) and (c), respectively. Moreover, the dispersion in Figure 5.5(a) clearly indicates that the splitting between even and odd modes increases as the groove spacing ( $P-W$ ) reduces. This trend follows the observation found in Figures 5.3(a) and (b) denoted by the green dashed lines and green dotted lines for the even and odd modes. Only when the incident angle of light is large enough can the odd mode be excited instead of even mode, which causes the resonance shift to shorter wavelengths at incident angles greater than  $60^\circ$ .

The field distributions at the resonance wavelength for periods of 180, 220 and 260nm further illustrates this coupling between GASP and MIMFP modes, as shown in

Figures 5.5(d), (e), and (f) for  $45^\circ$  angle of incidence. The resonance mode for a period of 180nm indicates that the field is mostly concentrated within the groove. Alternatively, when the period is greater than 220nm the field is both in the groove and on top of the grating. This indicates strong coupling between MIMFP and GASP modes, leading to the angular dependence of the reflection dips. The information in this set of the figures also confirms that the angle independent reflection spectra occur at periods  $< 180\text{nm}$  for visible wavelengths of light. Moreover, the light confinement is manipulated with respect to periodicity  $P$  in the Figures 5.5(d), (e), and (f) with stronger coupling into GASP modes for larger periods. The period controllable optical field confinement in this nanostructure can be a design principle for applications that require strong field confinement such as photovoltaics, high sensitivity nanofluidic index sensors, and plasmonic enhanced nanoscale emitters.





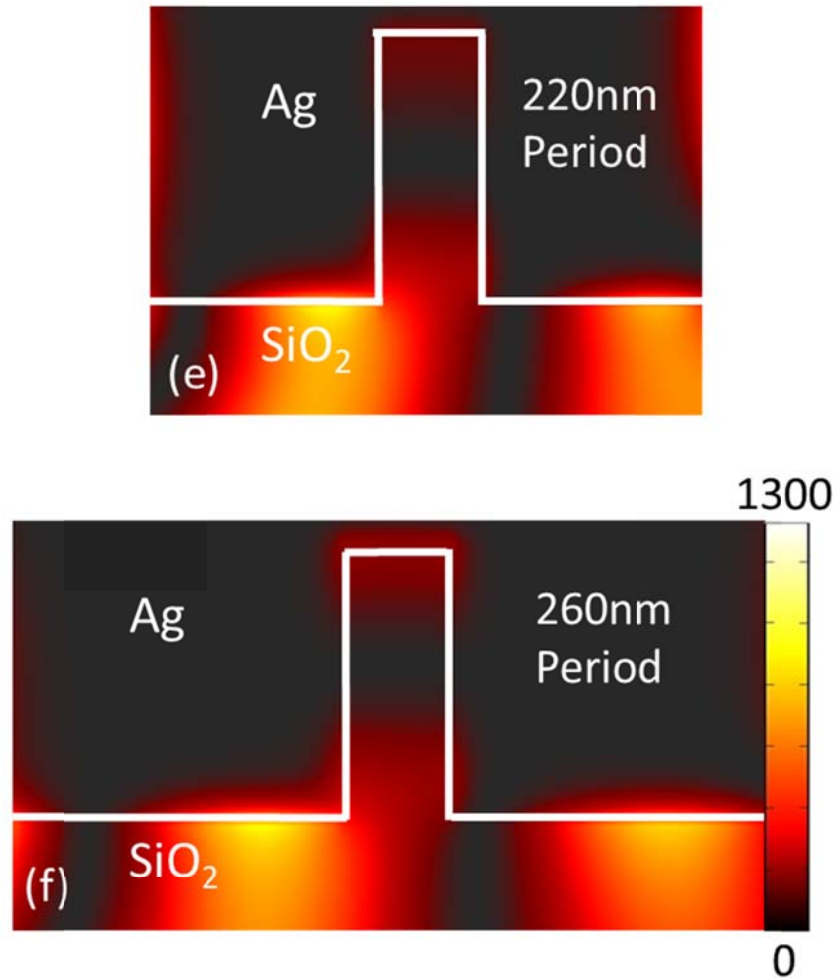


Figure 5.5 Optical mode coupling and period dependent field confinement. (a) shows mode dispersion with respect to the groove spacing (P-W) and Period, as well as the definition of even and odd modes in the insets. The field distribution of  $H_y$  with defined even and odd modes is plotted in (b) and (c), respectively. The intensity distribution of magnetic field  $H_y$  at the incident illumination angle of  $45^\circ$  is presented at  $P=180\text{nm}$  (d),  $220\text{nm}$  (e),  $260\text{nm}$  (f). (d) confirms that the field is well confined within the nano-groove corresponding to a MIMFP mode, while (d) and (f) show coupling to the top of the grating corresponding to GASP modes.

## 5.6 Summary

We have designed, fabricated and analyzed one dimensional nanostructure with angle-robust color response. Light funneling is employed as a method for angle independent coupling into localized resonances in metallic nanoslits. Color tunability across the visible spectrum and pixel size beyond the diffraction limit have also been demonstrated. Through simulation and experimental confirmation, design principles have been developed for angle tolerant spectrum response. Angle dependence has been avoided with a designed periodic structure for visible wavelength resonances employing MIMFP modes. Finally, field confinement and manipulation within these nano-grooves induced through sub-wavelength periodic effects are discussed. This device is capable of wide color tunability in the visible wavelength regime and can be used as a guideline for designing devices that require consistent performance independent of incident angles of light. This thorough analysis is important for the design of the angle-robust transmission type color filters in the incoming chapter. In the next chapter, the structure in the chapter 5 will be used as a design rule for transmission type color filters to move toward the final goal for replacement of pigment color filters in LCD industry.

# Chapter 6 Wide angled transmission plasmonic color filters

## 6.1 Introduction and motivation

In the chapters 3.1, 4.1, and 5.1, the literature survey shows clearly that the transmission type structural colors based on plasmonic nanostructure and photonic crystals have become an emerging research field recently. However, the angle sensitive color response in all of the aforementioned related works impedes the transmission type plasmonic based color filters from replacing the current pigment color filters in liquid crystal display industry.

In chapter 5, we propose and study a plasmonic nanostructure that has angle independent spectrum filtering effect for reflection type color filtering. The proposed structure successfully demonstrates angle tolerance as large as  $\pm 80^\circ$ . In order to further apply the angle robust design principles in the chapter 5 to plasmonic transmission type spectrum filtering for color filters in liquid crystal display panels, the plasmonic structure has to be redesigned. Based on the chapter 5, three designs for angle insensitive transmission type plasmonic color filtering are proposed in this chapter.

## 6.2 Design I for the transmission color filters and its results

The schematic of the Design I shows in Figure 6.1(a). The design has very similar schematic with the reflection type color filter in Figure 5.1(a) except the SiO<sub>2</sub> periodic structure (yellow region) without the top being blocked. In this figure, the nanostructure is defined by the width of the nano-slits  $W$ , the height of the slits  $D$ , and period  $P$ . Based on the calculation with real silver (Ag) refractive index model, the transmission spectra for blue, green, and red can be achieved by varying  $D$  from 70nm to 120nm, shown in Figure 6.1(b). Moreover, the angle resolved spectrum simulation in Figure 6.1(c) shows that the resonance holds at 470nm from launching angle of 0° to 80°. Therefore, this nanostructure design not only provides a widely tunable resonance through the visible region but also holds the resonance wavelength with viewing angle up to  $\pm 80^\circ$ .

In order to understand this transmission type plasmonic nanostructure, the field intensity distribution ( $|H_y|^2$ ) at resonance wavelength is plotted in Figure 6.1(d). This mode distribution is found to share the same principle with the reflection type color filter – MIMFP mode. This MIMFP resonance condition can be described as

$\frac{1}{2}m\lambda = n_{eff}D$ . It is noticed that the missing  $\frac{1}{4}\lambda$  is due to boundary condition of the proposed MIMFP structure with both sides being open ended.

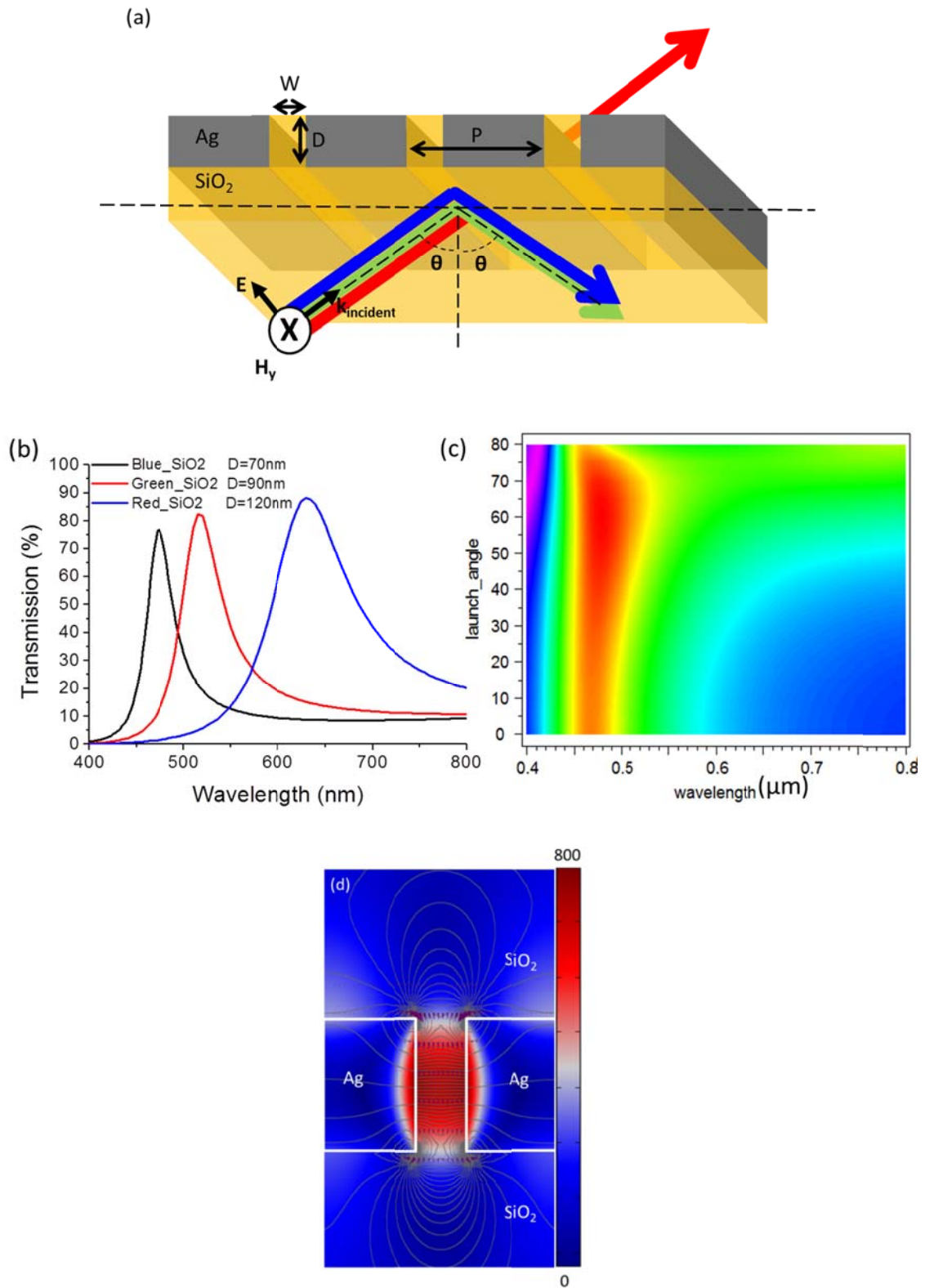


Figure 6.1 (a) Schematic of transmission color filter Design I with the geometrical parameters defined same as Figure 5.1(a). (b) Spectra for blue, green, and red color based on the Design I with various height 70-120nm (c) Simulated angle resolved spectrum for the blue color filter, and (d) Hy field intensity distribution at resonance wavelength=480nm.

### 6.3 Discussion – Design I

Color tunability and color purity are two important factors of the transmission color filters in real application. In this section, we would like to introduce another color tuning mechanism, and further discuss the color tunability and color purity issues for the MIMFP modes in transmission type structure based on the resonance condition equation in the previous section. This resonance condition indicates that the resonance can be manipulated with varying  $n_{eff}$ , which can be achieved by changing  $W$ , the width of the nanoslits. The simulation in Figure 6.2(a) demonstrates the transmission resonance from blue to red across the entire visible regime by changing  $W$  from 60 to 20nm, given fixed period of 180nm. Compared to the color tuning method by changing  $D$ , this method is favorable due to simple and low-cost fabrication process. Also, the average transmission percentage is above 70%. It is also found that the background at longer wavelength for each spectrum increases with  $W$ . This

phenomenon causes color impurity problem on color filter application, and it will be elaborated in the following paragraphs.

In order to investigate the relationship between large flat background and slit width  $W$ , a simulation is performed and demonstrated in Figure 6.2(b). Given the fixed period  $P$  and the resonance wavelength  $\lambda$ , this simulation shows the transmission spectra in various  $W$  swept from 60nm to 20nm. As  $W$  decreases, the flat background at longer wavelength is suppressed further. When  $W=20\text{nm}$ , this background is totally suppressed. To further understand this background change with  $W$ , we apply a MIMFP cavity like the left-handed figure in Figure 6.2(c) to be equivalent to a typical dielectric Fabry-Perot (FP) model in right hand side of the same figure. It is known that Fabry-Perot has transmission  $T_{FP}$  determined by reflection coefficient for normal incidence  $R = \left(\frac{n_{in}-n_{out}}{n_{in}+n_{out}}\right)^2$  in the following equation:  $T_{FP} = \frac{(1-R)^2}{(1-R)^2 + 4R(\sin(n_{in}D/\lambda))^2}$ .

According to this equation, off-resonance  $T_{FP}$  magnitude (which indicates background) is determined by the denominator. In other words, the off-resonance  $T_{FP}$  will be suppressed when  $R$  approaches to 1, which indicates  $n_{in}$  has to be much larger than  $n_{out}$ . However, the  $n_{in}$  in the case of MIMFP does not always have large at longer wavelength due to the waveguide (WG) dispersion. The propagation constant dispersion of the MIM WG ( $2\pi n_{in}/\lambda$ ) is calculated in Figure 6.2(d), where the green dash line represents

the optical wave propagation constant ( $2\pi n_{\text{SiO}_2}/\lambda$ ) in silica ( $n_{\text{SiO}_2}=1.46$ ). This figure shows that the dispersion curve of the MIM WG has propagation constant value 18.53 very close to that in silica material 15.46 at  $\lambda=700\text{nm}$  when  $W=60$ . On the other hand, this value becomes 26.87 at  $\lambda=700\text{nm}$  when  $W=20\text{nm}$ . This conclusion indicates that narrower slit width  $W$  helps suppress the background transmission at longer wavelength, and it agrees well with the simulation results in Figure 6.2(a) and (b).

The last paragraph is summarized with better background suppression performance at small  $W$ . However, a trade-off between background suppression and color tunability is revealed in Figure 6.2 (d). According to the dispersion calculation in this figure,  $W$  cannot be too small since color tunability is affected by small slit width  $W$ . In the inset of Figure 6.2(d), we observe that the propagation constant dispersion has visible wavelength region where MIM WG has dramatically increasing waveguide propagation loss (imaginary part of propagation constant) at shorter wavelength, and the cavity resonance cannot form due to large loss in these regions. Those regions in the case of  $W=60, 40, 20\text{nm}$  are 400-420nm, 400-440nm, and 400-510nm, respectively. It is clear that these regions will increase when  $W$  decreases. The conclusion also agrees with the simulation results. In summary, the relationship between  $W$  and lossy waveguide region indicates that the color tunability will be restricted if  $W$  is chosen too

small. Therefore, the trade-off between background suppression and color tunability degrades the performance of this version of the transmission plasmonic color filter.

Furthermore, small  $W$  affects transmission magnitude, one of the important parameters for transmission color filters. In Figure 6.2(b), it is also noticed that the transmission maximum drops to 40% at  $W=20\text{nm}$ . The low transmission can be understood based on the effective funneling region that Shi et al. proposed<sup>118</sup>.

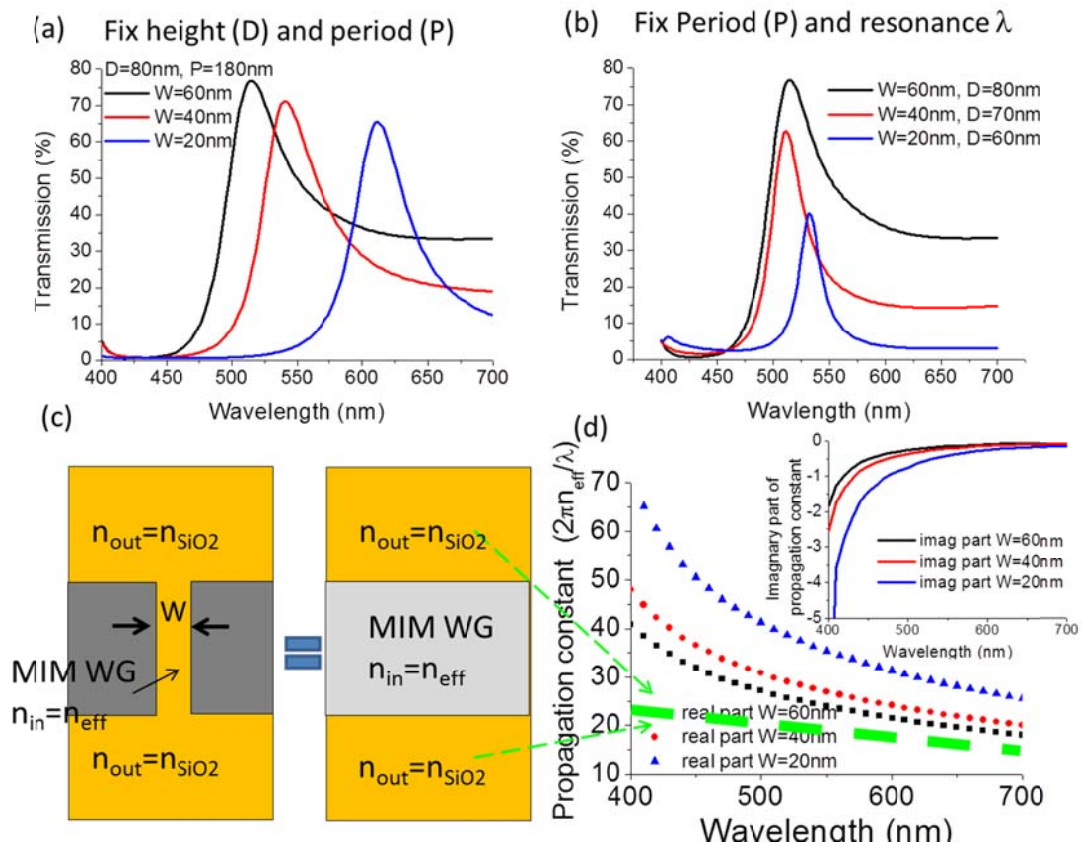


Figure 6.2 (a) Transmission spectra for blue, green, and red color with various  $W$  from 60 to 20nm given  $P$  and  $D$  fixed, and (b) Transmission spectra with various  $W$  from 60 to 20nm given resonance wavelength and  $P$  fixed. (c) the equivalent F-P model for

MIMFP cavity, (d) dispersion curves of the MIM waveguide (WG) at  $W=20$  (in blue), 40 (in red), 60nm (in black), and the green dash curve indicates the dispersion of the  $n_{out}$ . The inset shows the imaginary part of propagation constant, which indicates waveguide loss.

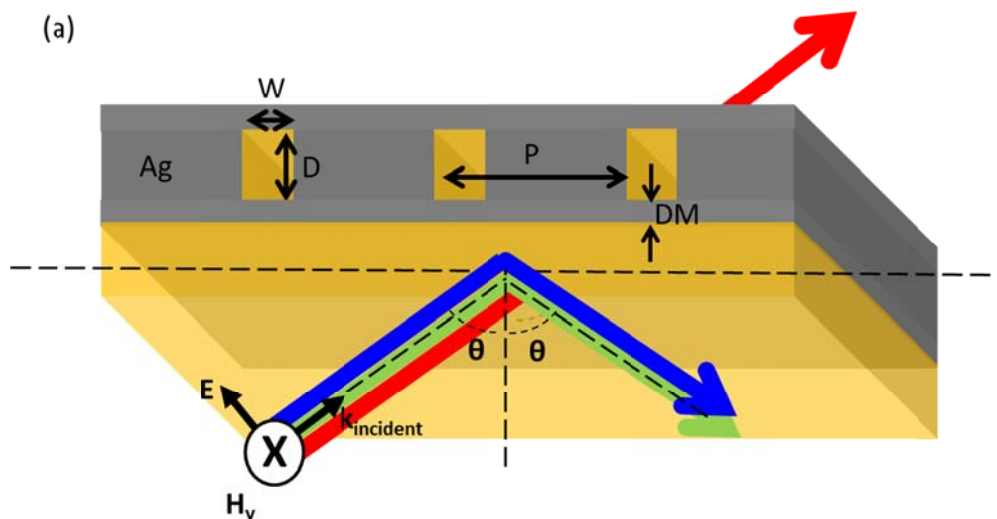
By combing the studies of background suppression, color tunability, and transmission magnitude, we finalize a conclusion for Design I in the following: this device design gives an very simple and clear idea about the implementation of the angle robust transmission type color filters, but however, the trade-off between color purity (due to the flat background at longer wavelength), color tunability, and transmission magnitude will be challenging to meet the criteria of the LCD transmission color filters. In order to improve this design, Design II is proposed in the next section.

## 6.4 Design II – improved design I

The Design I requires trade-off between the three important factors for LCD color filters: color purity, color tunability, and transmission magnitude. In this trade-off, color purity requires small  $W$ , whereas color tunability and large transmission magnitude prefer large  $W$ . Hence, this trade-off impedes this Design I from achieving all LCD filter requirements. In order to achieve a plasmonic design meeting all the

criteria of LCD color filters, one has to decouple this trade-off relationship.

The schematic of the Design II based on the improvement of the Design I is proposed in Figure 6.3(a). Herein additional parameter thickness of Ag mirror DM is defined. Instead of having open ends at the either side of the MIMFP cavity, this nanostructure includes two Ag metal mirrors to provide high reflectivity. Since this strategy does not rely on the large index contrast ( $n_{in} - n_{out}$ ) to reduce flat background issue in the last section, it helps decouple the trade-off between flat background suppression, color tunability, and transmission magnitude. Based on the design in Figure 6.3(a), we are able to optimize the parameters of period  $P$ , depth  $D$ , and slit width  $W$  to achieve a set of blue, green, and red (RGB) color filters which have good color purity and color tunability with fixed  $D=90\text{nm}$  and  $DM=20\text{nm}$  shown in Figure 6.3(b). Therefore, the Design II resolves the trade-off issue in the design I.



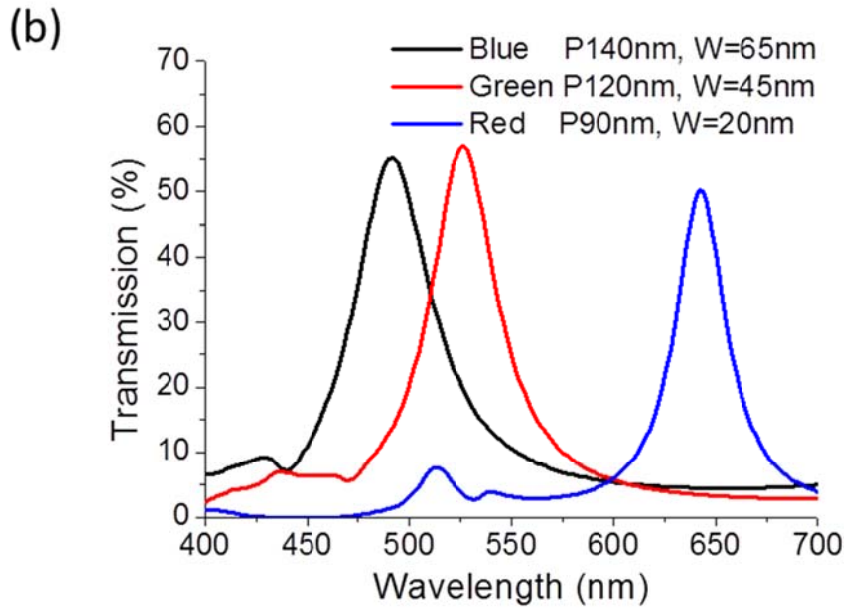


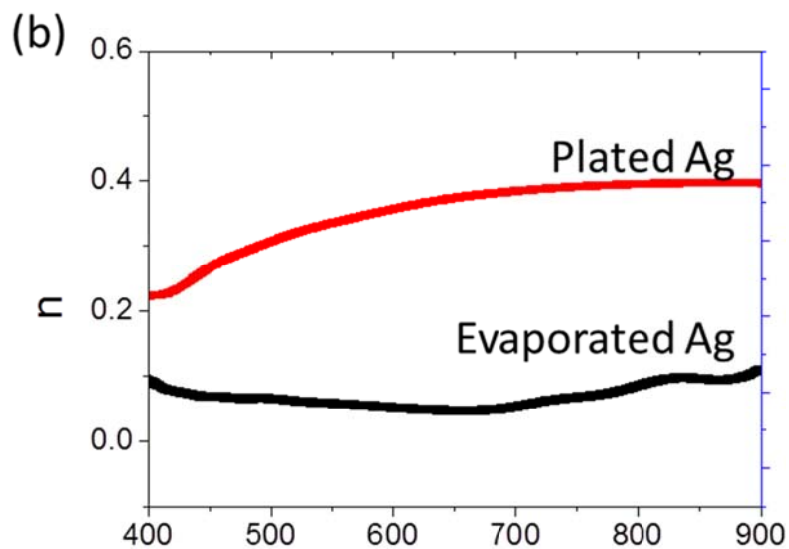
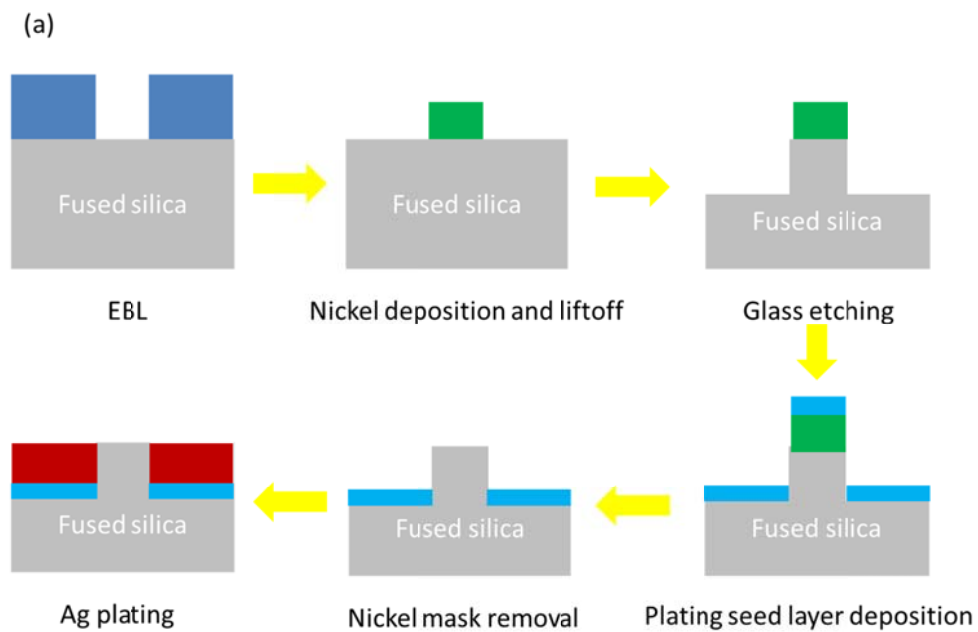
Figure 6.3 (a) Schematic of the design II, where DM is added and defined as the thickness of the top and bottom metal layer. (b) The optimized spectra for blue, green, and red colors given  $D=90\text{nm}$  and  $DM=20\text{nm}$  fixed .

## 6.5 Discussion – Design II

In the previous section, the Design II is shown to be capable of resolving performance trade-off problem. In order to implement this device in experiment, a fabrication process is proposed in Figure 6.4 (a). The whole process requires, first, nanopatterning lithography such as ebeam lithography (EBL). A nickel mask pattern lift-off is then performed. Afterwards, a self-aligned plating seed layer is patterned before silver (Ag) plating. The current bottle neck of this process is Ag plating, and this process is under development. The real part of refractive index of preliminary

plated Ag film is more lossy than evaporated and sputtered Ag, shown in Figure 6.4 (b).

Figure 6.4 (c) demonstrates that the simulated transmission resonance with plated silver does not have a clear resonance as the one with evaporated silver. Therefore, in order to obtain low loss silver film, the electrochemical silver plating method has to be improved.



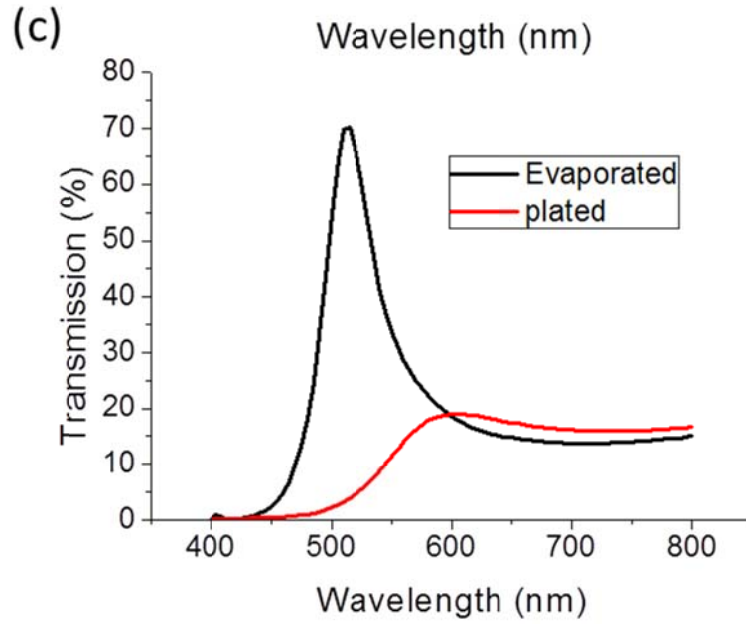


Figure 6.4 (a) shows the developed fabrication process, and (b) depicts the real part of refractive indices for plated (red curve) and evaporated silver (black curve), and (c) demonstrates the simulated transmission spectra with plasmonic metals as plated (red curve) and evaporated silver (black curve), where evaporated one has sharp resonance compared to plated one.

## 6.6 Design III – coupled cavity type transmission color filters

In the previous sections, the Design I and II show clearly that the angle robust transmission type color filters can be achieved based on MIMFP cavities. Furthermore, with top and bottom mirrors sandwiching the MIMFP cavity, the trade-off between color tunability and color purity will be solved. However, fabrication process in this

case requires much effort such as silver etching or silver electrochemical plating, shown in the previous sections. In order to reduce the complexity on the fabrication, another approach to transmission color filters is proposed with the geometrical parameters defined in the caption of Figure 6.5(a). The simulated transmission spectra of the proposed structure show in Figure 6.5(b). By sweeping  $W$  from 50 to 90nm, we are able to achieve the transmission maxima changing from 530 to 730nm, given  $DT=70$ ,  $DB=50$ ,  $WS=15$ ,  $D=100$ , and  $P=140$ nm fixed.

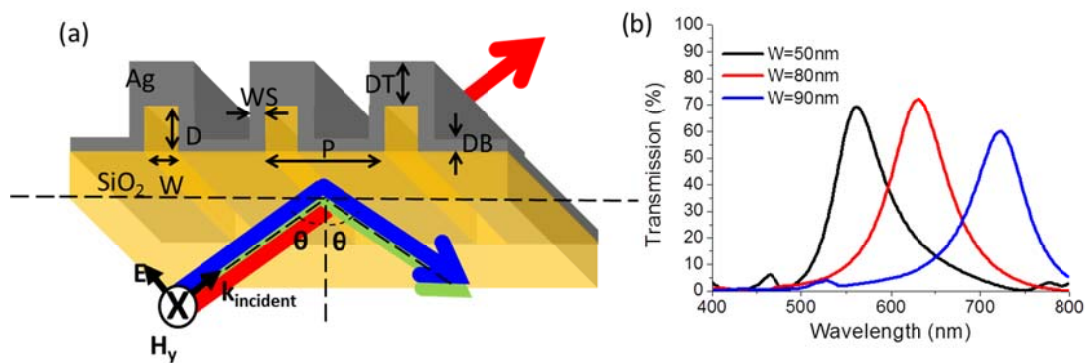
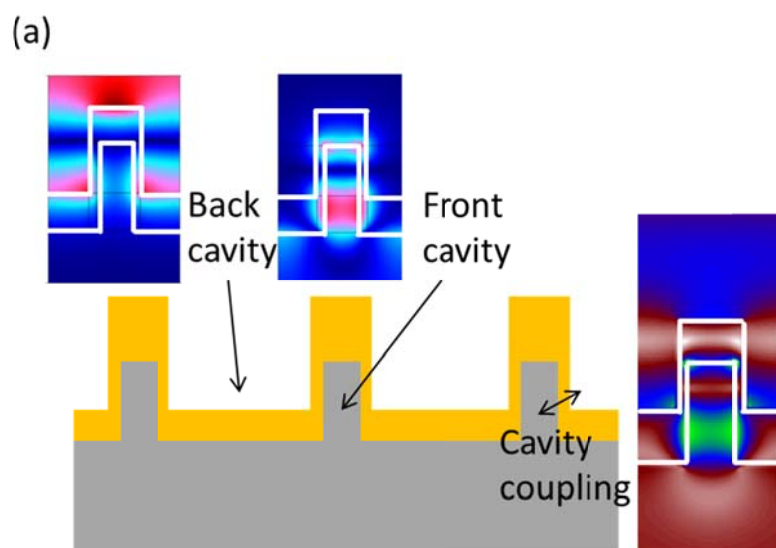


Figure 6.5 (a) schematic of the coupled cavity transmission type color filter, where  $WS$ ,  $DT$ ,  $DB$  are added and defined as sidewall metal thickness, top metal thickness, and bottom metal thickness, respectively. (b) The simulated spectra for varying  $W$  from 50 to 90nm, given  $DT=60$ ,  $DB=30$ ,  $WS=15$ ,  $D=100$ , and  $P=140$ nm fixed.

Figure 6.6(a) shows the mechanism of this coupled cavity design. The coupled cavity design can be divided into two cavities – front and back cavity, shown in Figure 6.6(a).

When WS is thick, the two cavities are isolated. On the other hand, the two cavities start to couple when the two cavity modes are spatially and spectrally overlap. The spatial overlap can be explained in the field plots of the front and back cavities in the same figure. The field plots of the back and front cavities are based on the field distribution at the resonance wavelength with the assumption of thick WS=50nm, but either of the two modes can still extend into boundary of each other. When the metal WS=15nm, the field distribution at transmission resonance shown in the right hand side is simply the add-up of the two field plots at left hand side. This clear evidence indicates the spatially overlapped fields of the two cavities. As for the spectral overlap, the absorption spectra of the front and back cavities show mode spectra in Figure 6.6(b). It is clear that the front mode has sharp resonance at 490nm, whereas the back mode has broad resonance with central wavelength 600nm. With cavity coupling effect, the resonance with cavity coupling is located right at middle of the two values—550nm.



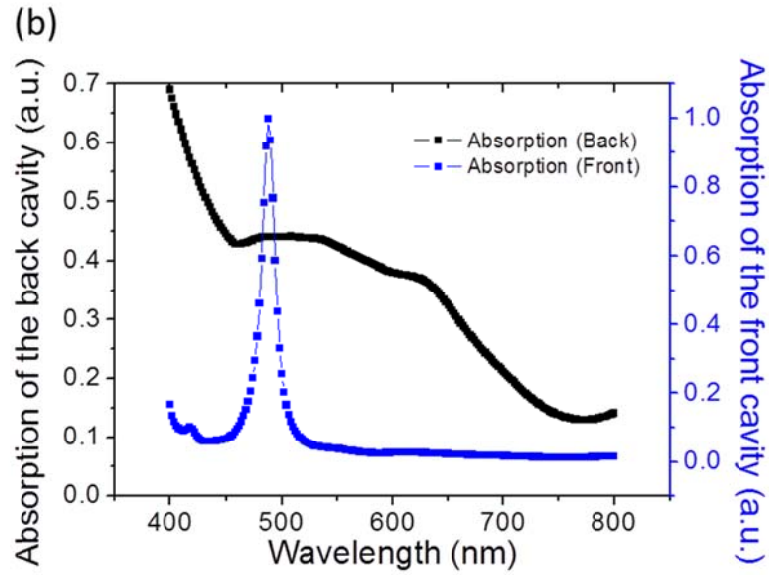


Figure 6.6 (a) Hy field distribution in front, back, and coupled cavities, and (b) the absorption spectra of front and back cavities. These two cavity modes are spatially (in (a)) and spectrally (in (b)) overlapped. Therefore, the two cavities form a coupled mode and provide transmission maximum.

Figure 6.7 (a) and (b) show the angular response spectrum filtering in simulation and in experiment, respectively. Both spectra indicate that the resonance wavelength shift is smaller than 7nm when viewing angle sweeps from 0 to 70 degree. This robust angular response on the resonance wavelength is again due to the MIMFP mode. More fabrication detail is available in the reference of Andrew Hollowell's thesis.

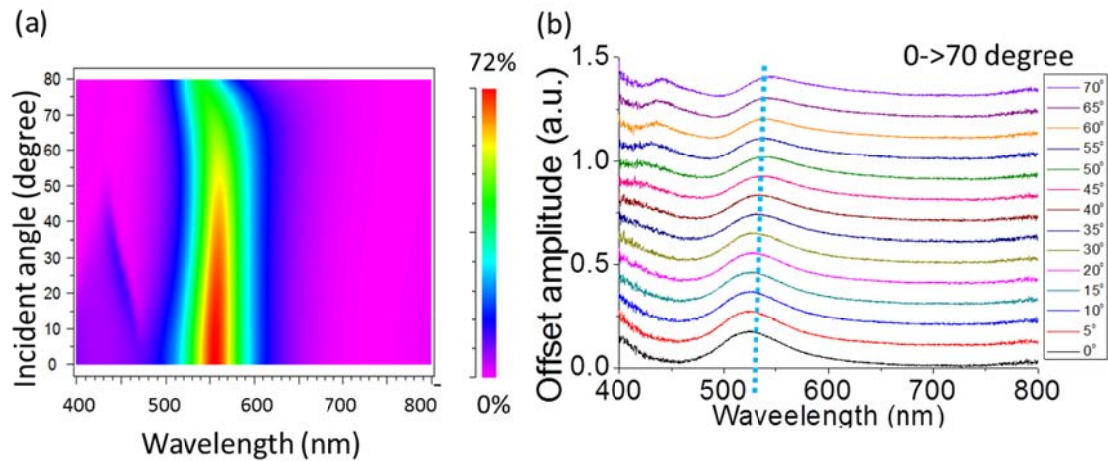


Figure 6.7 (a) simulated and (b) experimental angular resolved spectra with angle swept from 0 to 80 degree.

## 6.7 Discussion – Design III

In the previous section, the resonance based on Design III shows very good angle tolerance, color purity, and color tunability. To study this device in more detail, we further study another scenario – thinner metal on the bottom of the silica grating (DB).

When the bottom metal thickness DB reduces from 50 to 30nm, the spectrum in Figure 6.8(a) clearly indicates a fano shape resonance with peak wavelength at 576nm. It is also noticed that angle tolerance becomes less robust in this case. In Figure 6.8 (b), the resonance located at 576nm shows angle tolerance of 45 degree, which is less robust than angle tolerance when DB is at 50nm. It shows that the transmission spectrum drops to zero across the entire visible range when angle is larger than 45 degree. The

main reason of the less robust angle tolerance is due to the fano resonance contributed by the two transmission pathways shown in Figure 6.8(c). One of the pathways is the cavity coupling, which is defined as a dark mode in fano resonance model and is described in Figure 6.6. Another pathway is the light that penetrates directly through the bottom metal, which is considered as a bright mode. The second pathway cannot be ignored when  $DB=30\text{nm}$  since the transmission through this pathway accounts for 10-30% of the total transmission. It has been studied in the photonic crystals structure that transmission and reflection type fano resonances are sensitive to the incident angle of light<sup>119, 120</sup> due to the angle dependent far field interference. Therefore, the pathway has to be suppressed in order to have better angle robustness of the transmission resonance. The interaction of these two pathways can be seen in FDTD simulation, and moreover, the shape of the resonance agrees with the universal analytic equation for fano resonance in reference<sup>121</sup>. According to angle swept absorption spectrum in Figure 6.8(d), we can find additional information to support this argument. The absorption maximum at the same wavelength dramatically increases from 30% to 90% around the angle of 45 degree. It indicates that the light tends to be trapped in the front and back cavities due to the interference between the energy coupled from cavity coupling and the energy directly passes through bottom metal.

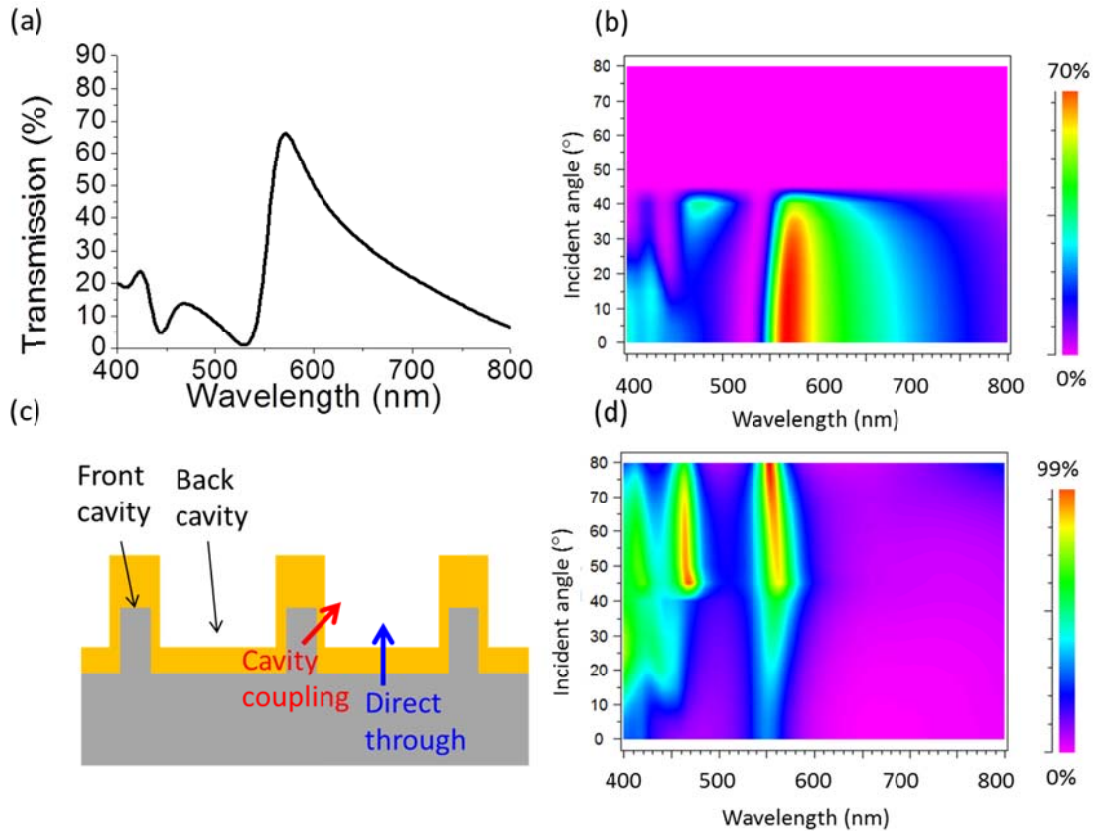


Figure 6.8 (a) the transmission resonance with fano shape peak located at 576nm with DB=30nm at normal incidence. (b) transmission spectra with various angle swept from 0 to 80 degree with bottom metal thickness DB reduces from 50 to 30nm. (c) the model of fano resonance in the design III. (d) absorption spectra with various angle swept from 0 to 80 degree

## 6.8 Summary

In this chapter, three plasmonic designs for angle insensitive transmission type color filters are proposed. The Design I shows a simple nanostructure that shares the same working principle with the plasmonic nanocavities in the chapter 5. In order to resolve

the performance trade-off issue, Design II decouples the trade-off factors – background suppression and color tunability— with Ag mirrors as reflectors at either side of nanocavities. To further decrease complexity level of manufacturing process for plasmonic color filtering devices, design III – coupled cavity type transmission filtering device is proposed. In the future, more performance and color tunability demonstration will be described in more detail based on the three designs in this chapter.

# Chapter 7 Summary and vision

## 7.1 Research summary

The light manipulation effects mentioned in chapter 1 enable many applications and possibilities. In this dissertation, the goal is to apply the light manipulation effects to improve the efficiency of microcavity lasers for photonic integrated circuits and achieve better performed color filters at visible wavelengths for LCD TVs. The works are summarized in the following:

1. Photonic crystal microdisk lasers

In Chapter 2, we demonstrate that the multi-stack photonic crystal microdisk lasers provide solutions both for spontaneous emission coupling efficiency and for cost issue of DWDM system.

The photonic crystal microdisk laser cavities are discussed in several aspects. First, this vertical 1D photonic crystals design is capable of boosting spontaneous emission coupling factor into lasing modes ( $\beta$ ) for microdisk cavities. It is achieved based on 1D photonic crystals in microdisk structure, which improves the suppression of the spontaneous emission into unwanted modes. This  $\beta$  enhancement can increase the

efficiency of microdisk based light sources and further reduce lasing threshold. Another important demonstration is that the mode splitting in this structure is easily achievable. By adjusting the spacing between top and bottom disks, as well as the thickness difference between these two disks, we are able to achieve multi-channel lasing and further reduce the cost of photonic integrated circuits.

## 2. High efficiency transmission type color filters

In the chapter 3, we proposed and demonstrated plasmonic nanoresonators to disperse light with high efficiency spectrally. By arranging resonators with different lateral dimensions such as metal grating period and duty cycle of the period, the resonance peaks can be manipulated, and furthermore, arbitrary colored patterns on a micrometer scale are achievable. These plasmonic structural colors provide an opportunity for display and imaging devices with a higher spatial resolution, as well as much smaller device dimensions than those currently available. The design principle can be easily expanded to other wavelength ranges for multispectral imaging.

In the chapter 4, the main focus is to further develop a version of the plasmonic resonator that further facilitates commercialization of the plasmonic color filtering devices in LCD display technology. Moving toward commercialization, we need to

focus on two aspects: one is further improvement on the optical performances of the devices, such as high transmission efficiency, good color purity, and large viewing angle tolerance. Another aspect is to develop a more efficient, high-throughput nanofabrication method to realize mass production with low costs. In the chapter 4, plasmonic based MRGW color filters are demonstrated to be manufacturable in large scale (2 inches), and this work paves the way for the commercial application of plasmonic color filters.

### 3. Angle insensitive resonance spectrum on plasmonic nanostructure for spectrum filtering application

Our goal is to design a novel transmission type color filter based on plasmonic resonance for LCD application. The plasmonic cavity designs in the chapter 3 and 4 show very good transmission efficiency, better color purity, low cost, and multi-functionality. However, angle dependent color response is an issue that has to be addressed by using other designs. In the chapter 5, we propose a plasmonic nanocavity structure for investigating the angle tolerance issue, and it shows promising solution for this issue. Moreover, in this chapter, the detailed physics of angle dependent color filtering effect is described. This proposed design also performs well as a reflection type color filter, and this device opens up the possibility on applications

on other technologies such as e-paper display (EPD), high resolution index sensors, and nanoemitters

#### 4. Angle insensitive transmission type spectrum filtering

In the previous chapter, the study related to angular response color filtering provides a clear insight on the designing angle robust color filtering devices. In the chapter 6, three plasmonic nanocavity based designs for angle insensitive transmission type color filters are proposed. The Design I shows a simple nanostructure that shares the same working principle with the plasmonic nanocavities in the chapter 5. In order to resolve the performance trade-off issue, Design II decouples the trade-off factors – background suppression and color tunability— with Ag mirrors as reflectors at either side of nanocavities. To further make manufacturing processes simple, the design III – coupled cavity type transmission filtering device — is proposed. In the future, more performance and color tunability demonstration will be described in more detail based on the three designs in this chapter.

## 7.2 Future work and vision

Light manipulation demonstrated in all the topics in this dissertation provides many

potential research topics and applications. Some of the possible directions are listed below:

1. E-paper display (EPD) technology based on angle insensitive reflection type color filters

In the chapter 5 and appendix 3, we have shown even a single nanocavity produces vivid colors. With very high resolution and good color purity, this design is possible to be a key component of the EPD. Substituting the color filtering layer and back reflector, this plasmonic color filter will keep the whole EPD device very simple and slim.

2. Light condenser and optical hotspot

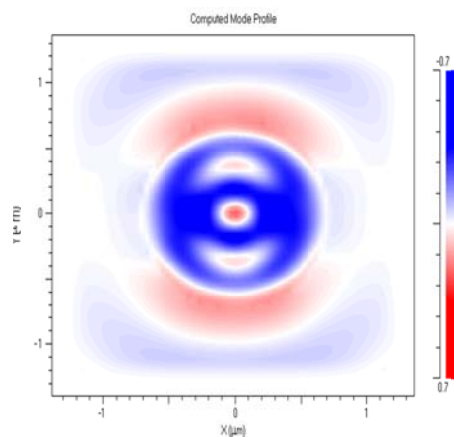
In the chapter 5 and 6, we have shown the optical field concentrates within the nanocavity very well (Figure 5.5 and Figure 6.1). The tight field confinement within the sub-100nm cavities results in very strong light intensity within it. It can be used for plasmonic transducers for energy conversion from optical wave to heat wave, to mechanical deformation, and even to electronic signal. The dielectric material has to be carefully chosen in order to meet the best performance both on plasmonic effect and on the energy that optical wave is converted to. Currently one possibility on this future direction is enhanced photo-acoustic signal generation.

### 3. Plasmonic materials

In the Figure 6.2 (a) in chapter 6, it shows a trade-off between the color tunability and color purity. This trade-off can be relaxed by using plasmonic material with larger real part of permittivity and small imaginary part of permittivity. The current conclusion in the plasmonic society shows that the best performing plasmonic material is still pure metal such as silver, aluminum, and gold. However, in order to achieve better performing plasmonic devices, improving plasmonic material is an important task. One of the options is metal alloy.

# Appendix 1. The importance of competing nonlasing modes – vertical Fabry Perot modes – in microdisk cavities

With FDTD Fullwave calculation, at least two nonlasing modes exist in a microdisk with diameter  $1.22D/\lambda$ . They are HE<sub>10</sub> and HE<sub>11</sub> shown in FIG. A1, with Q of 34 and 12. Even the Q is low such that associated Purcell factor F is small, they still affect  $\beta$  due to comparable average Purcell factor  $F_{ave}$ . The reason is that Purcell factors for the lasing WGM modes depends on the emitter location. Only at the very edge do the emitters strongly couple into lasing WGM mode, while those emitters not at the very edge of the disk will tend to funnel emission into FP modes.



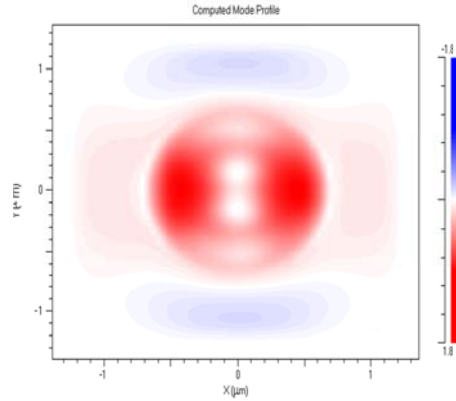


Figure A1. The mode profiles of HE(1,0) and HE(1,1) in the microdisk cavities oscillating up and down.

The calculation of  $\beta$  in previous literature<sup>52 53</sup> consider only dipoles at the very edge of the microdisk, not including those emitters away from the disk edge. The simulated  $\beta$  was reported to be at most 30%, yet the calculation still overestimates. Emitting dipoles away from the edge of the microdisk should be considered and play a critical role on the spontaneous emission coupling factor. The reason for it is that vertical Fabry Perot modes concentrate around the disk center. For proving this idea, we calculate not only  $F_{ave}$  and  $F_{cav}$  but also the dipole-field matrix element of those modes compared with the dipole moment for Whispering gallery modes (WGM). Given a single microdisk with thickness of 300nm and diameter of 1.2 $\mu$ m, the dipole-field matrix element  $|d \cdot E|^2$  in an active layer for a WGM and for a Fabry Perot mode is comparable. In COMSOL simulation, we consider dipoles' contribution from different positions in the microdisk by placing five dipoles in different position radially.

The dipole-field matrix element of WGM mode is 0.08, whereas those for HE(1,0) and HE(1,1) is 0.06 and 0.12, respectively. Since these values are all comparable, we strengthen the argument of strong mode competition from vertical Fabry Perot modes again.

# Appendix 2. Definition of the sweeping angles

The goal of this work is to solve the angle dependent color response (iridescence) with the viewing angle swept perpendicular to the grating direction, which is a key challenge in structural colors using grating couplings. For any grating coupled resonances, it is known that the color spectra are invariant for angles varied in the direction of the grating; only angle varied in the plane that is orthogonal to the grating orientation would produce resonance shift. These are illustrated in Figures A2 and A3 for the period of 180 and 260nm, respectively. Using the localized F-P resonances and appropriate grating period [Figure A1(a)] as discussed in the paper, we have successfully addressed angle dependent color change depicted in Figure A2 (a).

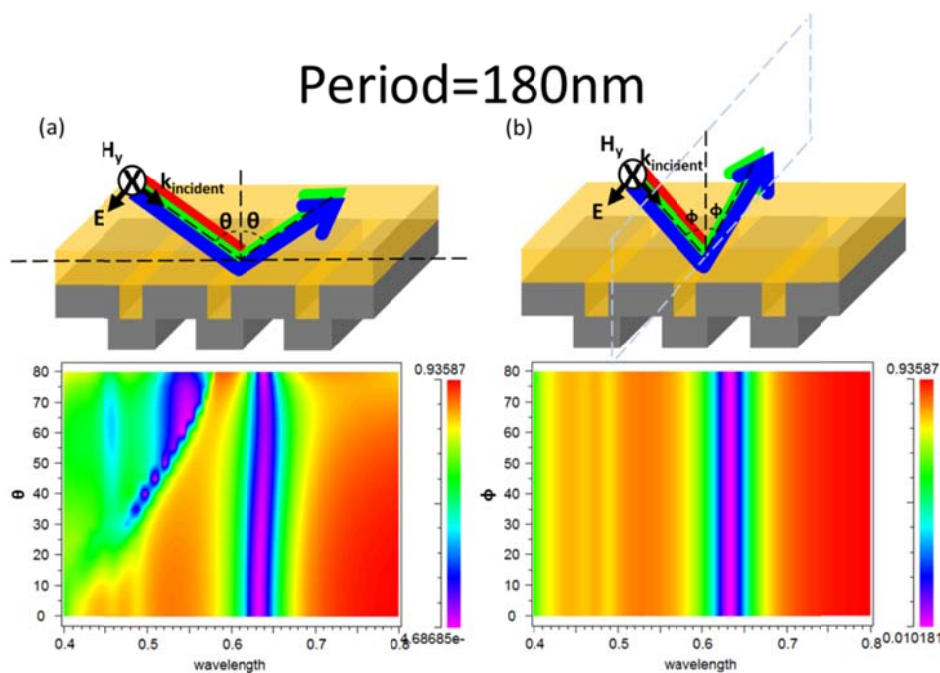


Figure A2. **The reflection spectrum at period=180nm with different angle sweeping orientation.** Measurement schematic and reflection spectra at angle sweeping (a) perpendicular to the grating orientation and (b) parallel to the grating direction.

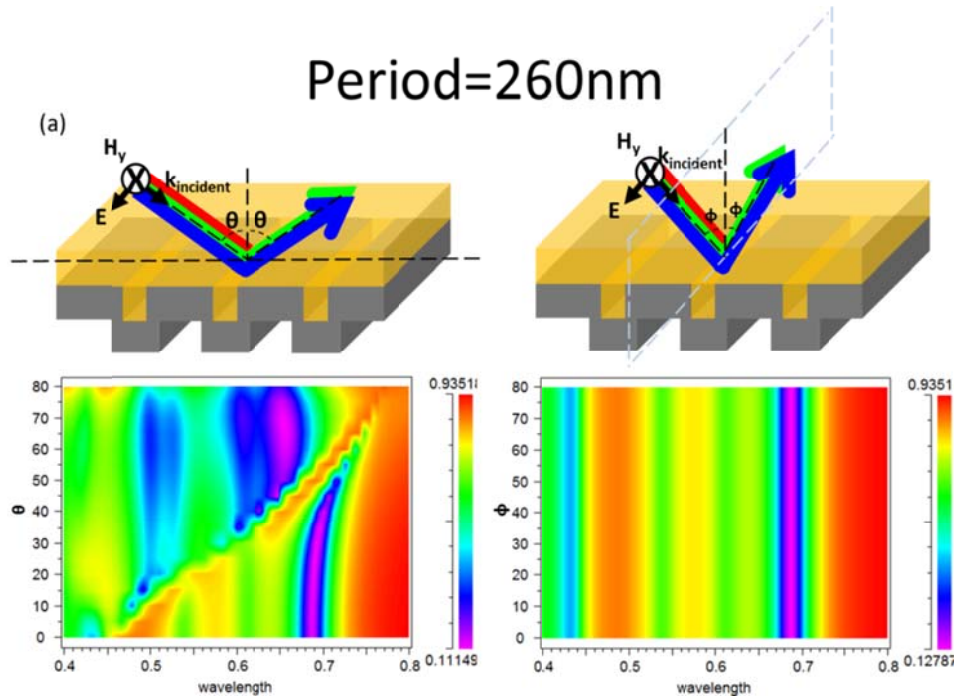


Figure A3. **The reflection spectrum at period=260nm with different angle sweeping orientation.** Measurement schematic and reflection spectra at angle sweeping (a) perpendicular to the grating orientation and (b) parallel to the grating direction.

# Appendix 3. Proof of single-cavity color effect

To prove that even single and double slits with size well beyond the diffraction limit can have color filtering effect, we include additional simulation results below. For the single slit calculation, the simulation parameters are included in Figure A4(a). Figure A4(b) shows the absorption of the light spectrum by a single slit.

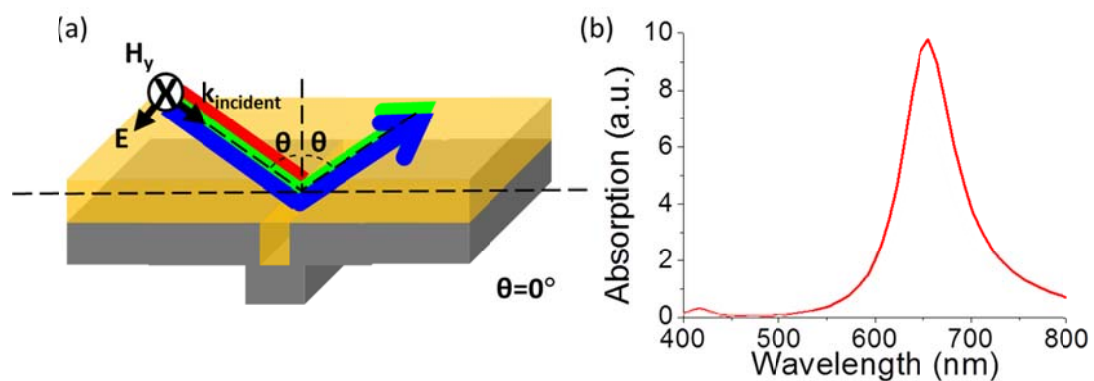


Figure A4. **Single slit case.** (a) Schematic, and (b) absorption spectrum.

As another example to illustrate the color pixels can be defined beyond diffraction limit, we further show the reflection spectrum in Figure A5(b) based on schematic in Figure A5(a). Noted that the two slits are 30 and 50nm wide, respectively, 20 times smaller than the spectrum wavelength to be filtered. Figure A5(b) shows two reflection dips and are verified to be contributed by the absorption from the different slits. To prove light funnels into different slits at different wavelength, we plot the  $H_y$  field distribution in

Figure A5(c). At resonance dip around 600nm, the resonance field concentrates in the slit with  $W=50\text{nm}$ , and the Poynting vectors shown as purple arrows flow into the aforementioned slit. On the other hand, field concentrates at the slit with  $W=30\text{nm}$  at resonance around 670nm. Poynting vectors also indicates the energy goes into  $W=30\text{nm}$  slit.

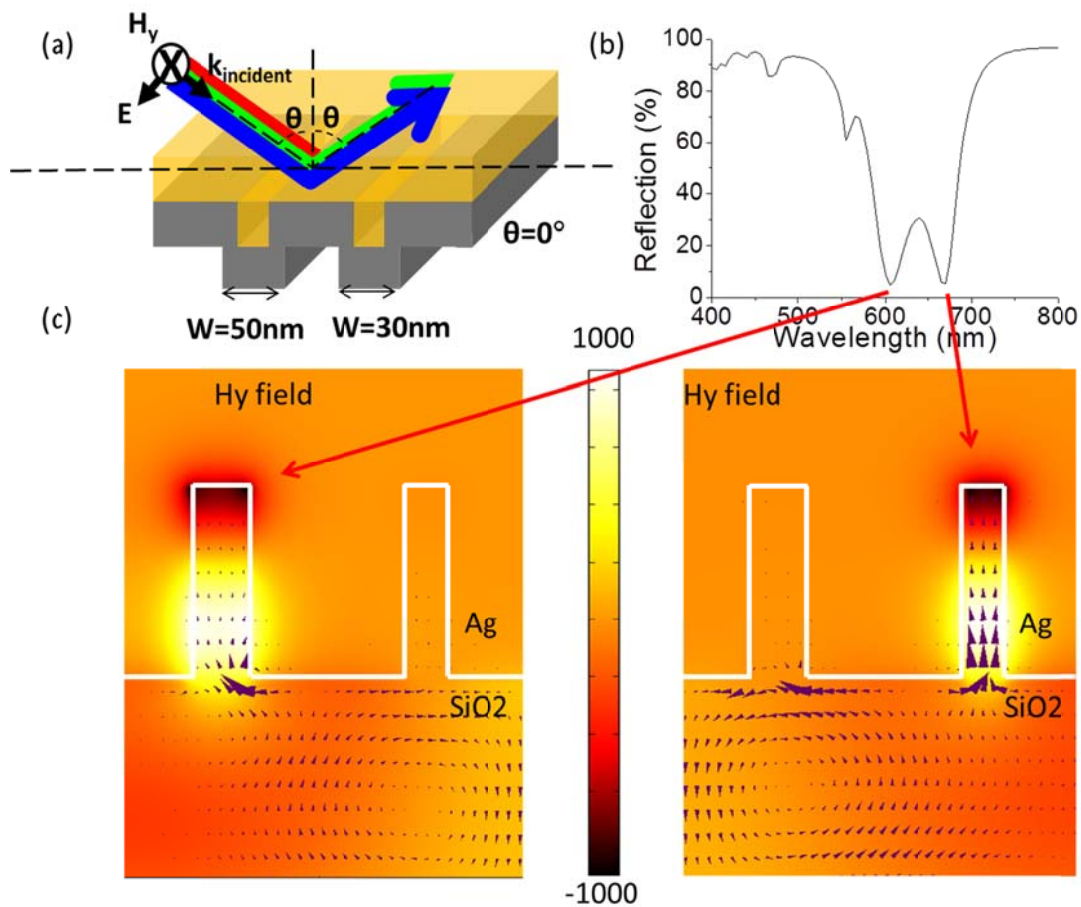


Figure A5. **Two slits case.** (a) Schematic, (b) simulated reflection spectrum, (c) the  $H_y$  field distribution in contour plots (with scale bar) and Poynting vector in purple arrows.

Furthermore, let us discuss the funneling efficiency of the single cavity at different angles. According to Figure A6(a), energy coupling efficiency into a single slit drops

10% when angle changes from 0 to 75 degree. This slight drop indicates the funneling zones are different at horizontal and vertical directions, which are defined as FH and FP respectively shown in Figure A6(b). Nevertheless, this slight drop does not affect the coupling efficiency in array case. The energy that is not captured by the first nanoslit will be eventually captured by the slits after the first one.

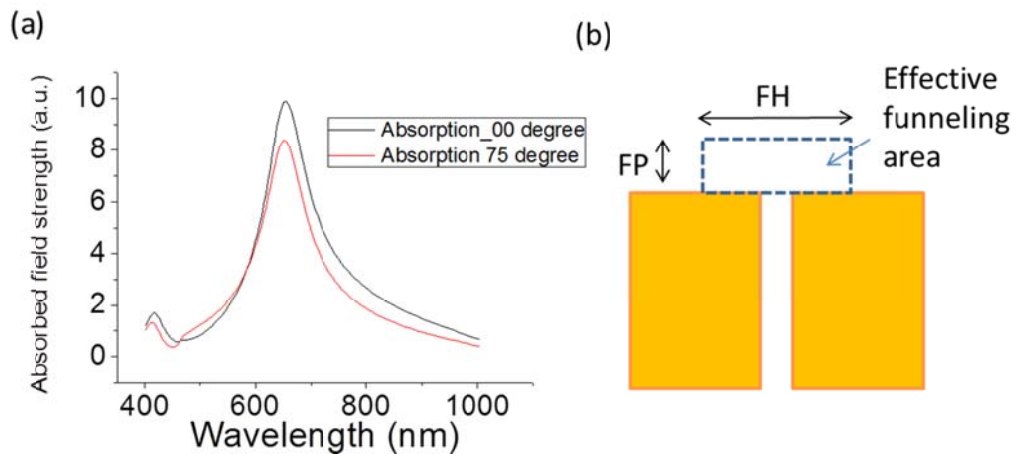


Figure A6 (a) absorbed optical field strength at angles of 0 and 75 degree, and (b) the schematic of the effective funneling area in different direction. Funneling in horizontal and vertical directions is defined as FH and FP.

# Bibliography

1. Siegman, A. E. Laser beams and resonators: The 1960s. *Ieee Journal of Selected Topics in Quantum Electronics* **6** (2000).
2. Vahala, K. J. Optical microcavities. *Nature* **424**, 839-846 (2003).
3. Ma, R. M., Oulton, R. F., Sorger, V. J., Bartal, G. & Zhang, X. A. Room-temperature sub-diffraction-limited plasmon laser by total internal reflection. *Nature Materials* **10**, 110-113 (2011).
4. Zhang, J. P. *et al.* Photonic-wire laser. *Phys. Rev. Lett.* **75**, 2678-2681 (1995).
5. Xu, T., Wu, Y., Luo, X. & Guo, L. J. Plasmonic nanoresonators for high-resolution colour filtering and spectral imaging. *Nature Communications* **1**, 59 (2010).
6. Benson, T. M. *et al.* Micro-optical resonators for microlasers and integrated optoelectronics - Recent advances and future challenges. *Frontiers in Planar Lightwave Circuit Technology Design, Simulation, and Fabrication* **216** (2006).
7. Zhang, Y. *et al.* Photonic crystal disk lasers. *Opt. Lett.* **36**, 2704-2706 (2011).
8. Noda, S., Fujita, M. & Asano, T. Spontaneous-emission control by photonic crystals and nanocavities. *Nature Photonics* **1**, 449-458 (2007).
9. Akahane, Y., Asano, T., Song, B. S. & Noda, S. High-Q photonic nanocavity in a two-dimensional photonic crystal. *Nature* **425**, 944-947 (2003).
10. Foresi, J. S. *et al.* Photonic-bandgap microcavities in optical waveguides. *Nature* **390**, 143-145 (1997).
11. Bleuse, J. *et al.* Inhibition, Enhancement, and Control of Spontaneous Emission in Photonic Nanowires. *Phys. Rev. Lett.* **106**, 103601 (2011).

12. Claudon, J. *et al.* A highly efficient single-photon source based on a quantum dot in a photonic nanowire. *Nature Photonics* **4**, 174-177 (2010).
13. Song, Q., Cao, H., Ho, S. T. & Solomon, G. S. Near-IR subwavelength microdisk lasers. *Appl. Phys. Lett.* **94**, 061109 (2009).
14. Chen, Y., Wu, Y. & Guo, L. J. Photonic crystal microdisk lasers. *Appl. Phys. Lett.* **98**, 131109 (2011).
15. Hill, M. T. *et al.* Lasing in metallic- Coated nanocavities. *Nature Photonics* **1**, 589-594 (2007).
16. Khajavikhan, M. *et al.* Thresholdless nanoscale coaxial lasers. *Nature* **482** (2012).
17. Alu, A., D'Aguanno, G., Mattiucci, N. & Bloemer, M. J. Plasmonic Brewster Angle: Broadband Extraordinary Transmission through Optical Gratings. *Phys. Rev. Lett.* **106**, 123902 (2011).
18. Cattoni, A. *et al.*  $\lambda/1000$  Plasmonic Nanocavities for Biosensing Fabricated by Soft UV Nanoimprint Lithography. *Nano Letters* **11**, 3557-3563 (2011).
19. Liaw, J. & Liu, C. Plasmonic effect of nanoshelled nanocavity on encapsulated emitter's spontaneous emission. *J. Quant. Spectrosc. Radiat. Transfer* **112** (2011).
20. Hill, M. T. *et al.* Lasing in metal-insulator-metal sub-wavelength plasmonic waveguides. *Optics Express* **17**, 11107-11112 (2009).
21. Marty, R., Baffou, G., Arbouet, A., Girard, C. & Quidant, R. Charge distribution induced inside complex plasmonic nanoparticles. *Optics Express* **18**, 3035-3044 (2010).
22. Deng, H., Weihs, G., Santori, C., Bloch, J. & Yamamoto, Y. Condensation of semiconductor microcavity exciton polaritons. *Science* **298** (2002).
23. Okamoto, K. *et al.* Surface-plasmon-enhanced light emitters based on InGaN quantum wells. *Nature Materials* **3** (2004).

24. Balet, L. *et al.* Enhanced spontaneous emission rate from single InAs quantum dots in a photonic crystal nanocavity at telecom wavelengths. *Appl. Phys. Lett.* **91**, 123115 (2007).
25. Nomura, M., Iwamoto, S., Kumagai, N. & Arakawa, Y. Temporal coherence of a photonic crystal nanocavity laser with high spontaneous emission coupling factor. *Physical Review B* **75**, 195313 (2007).
26. Hughes, S. Modified spontaneous emission and qubit entanglement from dipole-coupled quantum dots in a photonic crystal nanocavity. *Phys. Rev. Lett.* **94**, 227402 (2005).
27. Baba, T. *et al.* Observation of fast spontaneous emission decay in GaInAsP photonic crystal point defect nanocavity at room temperature. *Appl. Phys. Lett.* **85** (2004).
28. Nazir, H. *et al.* Multilayered silicone oil droplets of narrow size distribution: Preparation and improved deposition on hair. *Colloids and surfaces.B, Biointerfaces* **100** (2012).
29. Lee, Y. *et al.* in *Interaction of Strong Terahertz Pulses with Exciton-Polaritons in Quantum-Well Microcavity* , 2011).
30. Bradley, M. S. & Bulovic, V. Intracavity optical pumping of J-aggregate microcavity exciton polaritons. *Physical Review B* **82**, 033305 (2010).
31. Lanty, G. *et al.* HYBRID PEROVSKITE - GaN EXCITON-POLARITONS IN A STRONGLY COUPLED MICROCAVITY. *11th International Conference on Optics of Excitons in Confined Systems (Oecs11)* **210** (2010).
32. Haroche, S. & Kleppner, D. Cavity Quantum Electrodynamics. *Phys Today* **42** (1989).
33. Purcell, E. M. Spontaneous Emission Probabilities at Radio Frequencies. *Physical Review* **69** (1946).

34. Gjonaj, B. *et al.* Active spatial control of plasmonic fields. *Nature Photonics* **5** (2011).
35. Ma, C. & Liu, Z. Designing super-resolution metalenses by the combination of metamaterials and nanoscale plasmonic waveguide couplers. *Journal of Nanophotonics* **5**, 051604 (2011).
36. Wei, F. & Liu, Z. Plasmonic Structured Illumination Microscopy. *Nano Letters* **10** (2010).
37. Challener, W. A. *et al.* Heat-assisted magnetic recording by a near-field transducer with efficient optical energy transfer. *Nature Photonics* **3** (2009).
38. Landy, N. I., Sajuyigbe, S., Mock, J. J., Smith, D. R. & Padilla, W. J. Perfect metamaterial absorber. *Phys. Rev. Lett.* **100**, 207402 (2008).
39. Hao, J. *et al.* High performance optical absorber based on a plasmonic metamaterial. *Appl. Phys. Lett.* **96**, 251104 (2010).
40. Teperik, T. V. *et al.* Omnidirectional absorption in nanostructured metal surfaces. *Nature Photonics* **2**, 299-301 (2008).
41. Morfa, A. J., Rowlen, K. L., Reilly, T. H., III, Romero, M. J. & van de lagemaat, J. Plasmon-enhanced solar energy conversion in organic bulk heterojunction photovoltaics. *Appl. Phys. Lett.* **92**, 013504 (2008).
42. Tvingstedt, K., Persson, N., Inganas, O., Rahachou, A. & Zozoulenko, I. V. Surface plasmon increase absorption in polymer photovoltaic cells. *Appl. Phys. Lett.* **91**, 113514 (2007).
43. Anger, P., Bharadwaj, P. & Novotny, L. Enhancement and quenching of single-molecule fluorescence. *Phys. Rev. Lett.* **96**, 113002 (2006).
44. Staffaroni, M., Conway, J., Vedantam, S., Tang, J. & Yablonovitch, E. Circuit analysis in metal-optics. *Photonics and Nanostructures-Fundamentals and Applications* **10** (2012).

45. Fang, W. *et al.* Large enhancement of spontaneous emission rates of InAs quantum dots in GaAs microdisks. *Opt. Lett.* **27**, 948-950 (2002).
46. Noda, S. Seeking the ultimate nanolaser. *Science* **314**, 260-261 (2006).
47. Ishii, S., Nakagawa, A. & Baba, T. Modal characteristics and bistability in twin microdisk photonic molecule lasers. *IEEE Journal of Selected Topics in Quantum Electronics* **12**, 71-77 (2006).
48. Liu, L. *et al.* An ultra-small, low-power, all-optical flip-flop memory on a silicon chip. *Nature Photonics* **4**, 182-187 (2010).
49. Won, R. & Paniccia, M. Integrating silicon photonics. *Nature Photonics* **4**, 498-499 (2010).
50. Blumenthal, D. J. *et al.* Integrated Photonics for Low-Power Packet Networking. *IEEE J. Sel. Top. Quant.* **17**, 458 (2011).
51. Xia, F. N., Sekaric, L. & Vlasov, Y. Ultracompact optical buffers on a silicon chip. *Nature Photonics* **1**, 65-71 (2007).
52. Vuckovic, J., Painter, O., Xu, Y., Yariv, A. & Scherer, A. Finite-difference time-domain calculation of the spontaneous emission coupling factor in optical microcavities. *IEEE J. Quant. Electron.* **35**, 1168-1175 (1999).
53. Xu, Y., Lee, R. K. & Yariv, A. Finite-difference time-domain analysis of spontaneous emission in a microdisk cavity. *Physical Review A* **61**, 033808 (2000).
54. Jaffrennou, P. *et al.* Whispering gallery mode lasing in high quality GaAs/AlAs pillar microcavities. *Appl. Phys. Lett.* **96**, 071103 (2010).
55. Baba, T. & Sano, D. Low-threshold lasing and purcell effect in microdisk lasers at room temperature. *IEEE Journal of Selected Topics in Quantum Electronics* **9**, 1340-1346 (2003).
56. Yu, K., Lakhani, A. & Wu, M. C. Subwavelength metal-optic semiconductor nanopatch lasers. *Optics Express* **18** (2010).

57. Bendickson, J. M., Dowling, J. P. & Scalora, M. Analytic expressions for the electromagnetic mode density in finite, one-dimensional, photonic band-gap structures. *Physical Review E* **53**, 4107-4121 (1996).
58. Yokoyama, H. & Ujihara, K. in (CRC Press, Boca Raton, FL, 1995).
59. Wang, Z. N., Zhai, T. R., Lin, L. & Liu, D. H. Effect of surface truncation on mode density in photonic crystals. *Journal of the Optical Society of America B-Optical Physics* **24**, 2416-2420 (2007).
60. H. Shen *et al.* Eight-channel reconfigurable microring filters with tunable frequency, extinction ratio and bandwidth. <http://arxiv.org/ftp/arxiv/papers/1007/1007.1169.pdf> (2009).
61. Ebbesen, T. W., Lezec, H. J., Ghaemi, H. F., Thio, T. & Wolff, P. A. Extraordinary optical transmission through sub-wavelength hole arrays. *Nature* **391** (1998).
62. Barnes, W. L., Dereux, A. & Ebbesen, T. W. Surface plasmon subwavelength optics. *Nature* **424** (2003).
63. Zayats, A. V., Smolyaninov, I. I. & Maradudin, A. A. Nano-optics of surface plasmon polaritons. *Physics Reports-Review Section of Physics Letters* **408** (2005).
64. Ozbay, E. Plasmonics: Merging photonics and electronics at nanoscale dimensions. *Science* **311** (2006).
65. Genet, C. & Ebbesen, T. W. Light in tiny holes. *Nature* **445** (2007).
66. Atwater, H. A. & Polman, A. Plasmonics for improved photovoltaic devices. *Nature Materials* **9** (2010).
67. Schuller, J. A. *et al.* Plasmonics for extreme light concentration and manipulation. *Nature Materials* **9** (2010).
68. Garini, Y., Young, I. T. & McNamara, G. Spectral imaging: Principles and applications. *Cytometry Part a* **69A** (2006).

69. Lee, H., Yoon, Y., Lee, S., Kim, S. & Lee, K. Color filter based on a subwavelength patterned metal grating. *Optics Express* **15** (2007).
70. Laux, E., Genet, C., Skauli, T. & Ebbesen, T. W. Plasmonic photon sorters for spectral and polarimetric imaging. *Nature Photonics* **2** (2008).
71. Diest, K., Dionne, J. A., Spain, M. & Atwater, H. A. Tunable Color Filters Based on Metal-Insulator-Metal Resonators. *Nano Letters* **9** (2009).
72. Zia, R., Selker, M. D., Catrysse, P. B. & Brongersma, M. L. Geometries and materials for subwavelength surface plasmon modes. *Journal of the Optical Society of America A-Optics Image Science and Vision* **21** (2004).
73. Dionne, J. A., Sweatlock, L. A., Atwater, H. A. & Polman, A. Plasmon slot waveguides: Towards chip-scale propagation with subwavelength-scale localization. *Physical Review B* **73**, 035407 (2006).
74. Bozhevolnyi, S. I., Volkov, V. S., Devaux, E., Laluet, J. Y. & Ebbesen, T. W. Channel plasmon subwavelength waveguide components including interferometers and ring resonators. *Nature* **440** (2006).
75. Neutens, P., Van Dorpe, P., De Vlamincx, I., Lagae, L. & Borghs, G. Electrical detection of confined gap plasmons in metal-insulator-metal waveguides. *Nature Photonics* **3** (2009).
76. Reilly, T. H., III, van de Lagemaat, J., Tenent, R. C., Morfa, A. J. & Rowlen, K. L. Surface-plasmon enhanced transparent electrodes in organic photovoltaics. *Appl. Phys. Lett.* **92**, 243304 (2008).
77. Lindquist, N. C., Luhman, W. A., Oh, S. & Holmes, R. J. Plasmonic nanocavity arrays for enhanced efficiency in organic photovoltaic cells. *Appl. Phys. Lett.* **93**, 123308 (2008).
78. Burgos, S. P., de Waele, R., Polman, A. & Atwater, H. A. A single-layer wide-angle negative-index metamaterial at visible frequencies. *Nature Materials* **9** (2010).

79. Chettiar, U. K., Kildishev, A. V., Klar, T. A. & Shalaev, V. M. Negative index metamaterial combining magnetic resonators with metal films. *Optics Express* **14** (2006).
80. Lezec, H. J., Dionne, J. A. & Atwater, H. A. Negative refraction at visible frequencies. *Science* **316** (2007).
81. Cai, W. *et al.* Metamagnetics with rainbow colors. *Optics Express* **15** (2007).
82. Diest, K., Dionne, J. A., Spain, M. & Atwater, H. A. Tunable Color Filters Based on Metal-Insulator-Metal Resonators. *Nano Letters* **9**, 2579-2583 (2009).
83. Wang, J. J. *et al.* High-performance nanowire-grid polarizers. *Opt. Lett.* **30** (2005).
84. Kang, M. & Guo, L. J. Nanoimprinted semitransparent metal electrodes and their application in organic light-emitting diodes. *Adv Mater* **19** (2007).
85. Kang, M., Kim, M., Kim, J. & Guo, L. J. Organic Solar Cells Using Nanoimprinted Transparent Metal Electrodes. *Adv Mater* **20** (2008).
86. Xu, T. *et al.* Directional excitation of surface plasmons with subwavelength slits. *Appl. Phys. Lett.* **92**, 101501 (2008).
87. Xu, T. *et al.* Structural Colors: From Plasmonic to Carbon Nanostructures. *Small* **7**, 3128-3136 (2011).
88. Hung, K., Pei, C., Hu, C. & Yang, T. Manipulation image processing algorithmic technology to realize 1.8" RGBW transfective TFT-LCDs with adjustable colour gamut. *Displays* **29** (2008).
89. Wang, S. S. & Magnusson, R. Theory and Applications of Guided-Mode Resonance Filters. *Appl. Opt.* **32** (1993).
90. Wang, S. S., Magnusson, R., Bagby, J. S. & Moharam, M. G. Guided-Mode Resonances in Planar Dielectric-Layer Diffraction Gratings. *Journal of the Optical Society of America A-Optics Image Science and Vision* **7** (1990).

91. Kaplan, A. F., Xu, T. & Guo, L. J. High efficiency resonance-based spectrum filters with tunable transmission bandwidth fabricated using nanoimprint lithography. *Appl. Phys. Lett.* **99**, 143111 (2011).
92. Cho, E. *et al.* Two-dimensional photonic crystal color filter development. *Optics Express* **17**, 8621-8629 (2009).
93. Vukusic, P., Sambles, J. R. & Lawrence, C. R. Structural colour - Colour mixing in wing scales of a butterfly. *Nature* **404**, 457-457 (2000).
94. Zi, J. *et al.* Coloration strategies in peacock feathers. *Proc. Natl. Acad. Sci. U. S. A.* **100**, 12576-12578 (2003).
95. Wu, Z., Lee, D., Rubner, M. F. & Cohen, R. E. Structural color in porous, superhydrophilic, and self-cleaning SiO<sub>2</sub>/TiO<sub>2</sub> Bragg stacks. *Small* **3**, 1445-1451 (2007).
96. Kumar, K. *et al.* Printing colour at the optical diffraction limit. *Nature Nanotechnology* **7**, 557-561 (2012).
97. Kinoshita, S., Yoshioka, S. & Miyazaki, J. Physics of structural colors. *Reports on Progress in Physics* **71**, 076401-076401 (2008).
98. Kim, H. *et al.* Structural colour printing using a magnetically tunable and lithographically fixable photonic crystal. *Nature Photonics* **3**, 534-540 (2009).
99. Kaplan, A. F., Xu, T. & Guo, L. J. High efficiency resonance-based spectrum filters with tunable transmission bandwidth fabricated using nanoimprint lithography. *Appl. Phys. Lett.* **99**, 143111 (2011).
100. Yokogawa, S., Burgos, S. P. & Atwater, H. A. Plasmonic Color Filters for CMOS Image Sensor Applications. *Nano Letters* **12** (2012).
101. Zhou, W., Gao, H. & Odom, T. W. Toward Broadband Plasmonics: Tuning Dispersion in Rhombic Plasmonic Crystals. *Acs Nano* **4**, 1241-1247 (2010).
102. Genet, C. & Ebbesen, T. W. Light in tiny holes. *Nature* **445**, 39-46 (2007).

103. Lee, K. *et al.* Enhancing Surface Plasmon Detection Using Template-Stripped Gold Nanoslit Arrays on Plastic Films. *Acs Nano* **6**, 2931-2939 (2012).
104. Yao, J. *et al.* Soft Embossing of Nanoscale Optical and Plasmonic Structures in Glass. *Acs Nano* **5**, 5763-5774 (2011).
105. Schmidt, M. A., Lei, D. Y., Wondraczek, L., Nazabal, V. & Maier, S. A. Hybrid nanoparticle-microcavity-based plasmonic nanosensors with improved detection resolution and extended remote-sensing ability. *Nature communications* **3**, 1108 (2012).
106. Brown, L. V., Sobhani, H., Lassiter, J. B., Nordlander, P. & Halas, N. J. Heterodimers: Plasmonic Properties of Mismatched Nanoparticle Pairs. *Acs Nano* **4**, 819-832 (2010).
107. Aksu, S. *et al.* High-Throughput Nanofabrication of Infrared Plasmonic Nanoantenna Arrays for Vibrational Nanospectroscopy. *Nano Letters* **10**, 2511-2518 (2010).
108. Ross, B. M., Wu, L. Y. & Lee, L. P. Omnidirectional 3D Nanoplasmonic Optical Antenna Array via Soft-Matter Transformation. *Nano Letters* **11**, 2590-2595 (2011).
109. Pasquale, A. J., Reinhard, B. M. & Dal Negro, L. Engineering Photonic-Plasmonic Coupling in Metal Nanoparticle Necklaces. *Acs Nano* **5**, 6578-6585 (2011).
110. Ikeda, K. *et al.* Structural Tuning of Optical Antenna Properties for Plasmonic Enhancement of Photocurrent Generation on a Molecular Mono layer System. *Journal of Physical Chemistry C* **116**, 20806-20811 (2012).
111. Le Perchec, J., Desieres, Y., Rochat, N. & de Lamaestre, R. E. Subwavelength optical absorber with an integrated photon sorter. *Appl. Phys. Lett.* **100**, 113305 (2012).

112. Le Perche, J., Quemerais, P., Barbara, A. & Lopez-Rios, T. Why metallic surfaces with grooves a few nanometers deep and wide may strongly absorb visible light. *Phys. Rev. Lett.* **100**, 066408 (2008).
113. Pardo, F., Bouchon, P., Haidar, R. & Pelouard, J. Light funneling mechanism explained by magnetoelectric interference. *Phys. Rev. Lett.* **107** (2011).
114. Polyakov, A. *et al.* Plasmonic light trapping in nanostructured metal surfaces. *Appl. Phys. Lett.* **98**, 203104 (2011).
115. Dionne, J. A., Sweatlock, L. A., Atwater, H. A. & Polman, A. Plasmon slot waveguides: Towards chip-scale propagation with subwavelength-scale localization. *Physical Review B* **73**, 035407 (2006).
116. Economou, E. N. Surface Plasmons in Thin Films. *Physical Review* **182**, 539-& (1969).
117. Fan, X., Wang, G. P., Lee, J. C. W. & Chan, C. T. All-angle broadband negative refraction of metal waveguide arrays in the visible range: Theoretical analysis and numerical demonstration. *Phys. Rev. Lett.* **97**, 073901 (2006).
118. Shi, H. & Guo, L. J. *Phys. Rev. Lett.* (accepted 2012).
119. Babic, L. & de Dood, M. J. A. Interpretation of Fano lineshape reversal in the reflectivity spectra of photonic crystal slabs. *Optics Express* **18**, 26569-26582 (2010).
120. Christ, A., Tikhodeev, S. G., Gippius, N. A., Kuhl, J. & Giessen, H. Waveguide-plasmon polaritons: Strong coupling of photonic and electronic resonances in a metallic photonic crystal slab. *Phys. Rev. Lett.* **91**, 183901 (2003).
121. Gallinet, B. & Martin, O. J. F. Influence of Electromagnetic Interactions on the Line Shape of Plasmonic Fano Resonances. *Acs Nano* **5**, 8999-9008 (2011).